DISSERTATION

STRUCTURAL HEALTH MONITORING IN ADHESIVELY BONDED COMPOSITE JOINTS

Submitted by

Steven Caldwell

Department of Systems Engineering

In partial fulfilment of the requirements

For the Degree of Doctor of Philosophy

Colorado State University

Fort Collins, Colorado

Spring 2024

Doctoral Committee:

Advisor: Donald W. Radford

Steven Simske
James Cale
Henry Adams

ABSTRACT

STRUCTURAL HEALTH MONITORING IN ADHESIVELY BONDED COMPOSITE JOINTS

Composite bonded aircraft structure is a prevalent portion of today's aircraft structural composition. Adequate bond integrity is a critical aspect of the fabrication and operational service life of aircraft structure. Many of these structural bonds are critical for flight safety. Thus, a major concern is related to the assurance of quality in the structural bond. Over the last decade, non-destructive bond evaluation techniques have improved but still cannot detect a structurally weak bond that exhibits full adherend/adhesive contact. Currently, expensive, and time-consuming structural proof testing is required to verify bond integrity. The objective of this work is to investigate the feasibility of bondline integrity monitoring via piezoelectric sensors embedded in the composite joint. Initially, a complex composite joint, the Pi preform, was analytically evaluated for health monitoring viability, with the results showing promising capability. Subsequently, due to experimental complexities, a simple, state-of-the-art composite single lap shear joint is selected for experimentation and analysis to measure and quantify the effect of incorporating a sensor within the bondline to evaluate and expand on the ability of the embedded sensor to monitor and assess the joint integrity. Simple flatwise tension joints are also studied to investigate an orthogonal loading direction through the sensor. The experimental results indicate that the embedded piezoelectric sensors can measure a change in the joint before the integrity degrades and fails on subsequent loadings, resulting in a novel approach for prognostic performance evaluation without detrimentally affecting the performance of the structural joint.

ACKNOWLEDGEMENTS

I would like to acknowledge and thank my advisor, Dr. Donald Radford, for guiding me through this journey. Also, I would like to thank my committee for providing constructive feedback to help me complete this effort. Finally, I thank the Colorado State University Department of Systems Engineering, specifically, Ingrid Bridge for her never ending help.

DEDICATION

This dissertation is dedicated to my wife Debbie who supported me and was by my side for this entire process.

TABLE OF CONTENTS

LIST OF TABLES

LIST OF FIGURES

Chapter 1 Introduction

Joints connected with mechanical fasteners worked well with metallic aircraft structures of the past. With the advent of lightweight composite aircraft structure, the use of bolted joints has become inefficient both due to the fastener hole drilling process and to the reduced shear out resistance of composites versus metal counterparts. The use of adhesively bonded joints in composite designs provides the characteristics of efficient production, light weight structure, and ease of maintainability[1-3]. An effective adhesive joint relies on correctly designed laminated composite adherends, an appropriate adhesive, and a strong interface between the adherend and the adhesive. While designing the composite adherend and choosing an appropriate adhesive are relatively well understood and readily controlled, a major downside is that the joint integrity is extremely sensitive to process control during the bonding operation. Poor process control during bonding can result in reduced bond interfacial strength and lead to a structurally weak bond that traditional non-destructive inspection techniques cannot detect since the adherends remain in full physical contact[4-6]. As the use of composite structure has increased, health monitoring has recently become a focus of study and improvement[7-11]. These studies offer approaches to evaluating the health of bonded composite assemblies, immediately after manufacture and throughout the service life of the aircraft.

Most of the research into structural health monitoring of composites is focused on damage to the composite material itself. Sensors are typically placed on the surface of the composite and sense damage to that external surface. There are many types of non-destructive inspection techniques that are used to detect damage to composite materials and bonded joints. The main inspection techniques are visual, optical methods, eddy current, ultrasonics, vibration, acoustics,

and radiography. Visual inspection does not apply since the area of concern is the integrity of the bond, which is enclosed by the adherends on either side. Optical methods employ the use of fiber optic sensors which are bonded to the surface of the composite joint. These sensors can detect minute changes to the strain field but the damage or imperfection in the bondline must create a strain change large enough to be sensed at the outer surface of the composite adherend. This may be problematic when the adherends are thick, meaning that the bond imperfection would not generate a disturbance through the skin laminate. Fiber optic sensors are expensive and generate a large amount of data that would be problematic to evaluate. Shearography is another optical method that uses interferometry to measure displacement changes at the external surface of the composite laminate. The displacement change represents a strain concentration due to the defect in the joint. This is more appropriate for a disbond that is present in the adherend lamina and may not be sensitive enough to capture an internal bond integrity issue. Eddy current inspections use electromagnetic energy to characterize surface or near surface defects such as cracks, and corrosion. This technique is mostly used to inspect metallic parts and not bonded composite joints. Ultrasonic inspection makes use of concentrated high energy acoustic waves that are generated and applied to the joint. They use a pulse echo method when only one transducer is used as a transmitter and a receiver of the pulse. With two transducers, a through transmission inspection can be performed to measure the signal as it passes through and comes out of the joint. These techniques are good at identifying delaminations in the adherends and flaws present in the adhesive bond. They do require a gap or a change in material property to be able to measure defects in the joint. Another technique for inspection is vibration, which is typically applied as a coin-tap to the material surface. The change is the sound field as the coin is tapped in the inspection area indicates a local defect in the composite joint. This technique is mostly used to identify disbonds and

delaminations near the surface of the adherend or between the composite facesheet and core in a sandwich bonded structure. It is doubtful that the coin-tap inspection would work for a evaluating the integrity of a structural bond between two non-sandwich adherends. Another inspection technique using vibration response employs surface mounted accelerometers to measure minute changes in the frequency response of the structure. Unfortunately, accelerometers measure relatively low frequency response of the structure and may not be sensitive enough to measure minute internal bond integrity defects. Radiographic inspection is typically used in applications with isotropic material. Composite joints are typically anisotropic and are low absorbers of radiologic energy. These techniques work well for inspecting local defects at the surface of the composite joint but have a limited capable to quantify a defect that manifests itself as a weakened bond, although there is full contact of the adherends with the adhesive in the joint. These types of weak bonds are sometimes referred to as “kissing” bonds and can exhibit a zero-volume disbond. These defected bonds could be due to many factors including improper bond surface preparation, surface contamination, adhesive curing issues, and residual stresses that are present during bonding operations. Bond defects of this nature can appear locally during fabrication and potentially grow during service use due to repeated loadings and moisture ingression, resulting in a compromised joint. Thus, there is a need for a suitable inspection technique that monitors the initial bond structural health and periodically evaluates of the bonded joint health after experiencing repeated loading in service.

Another option is to embed a sensor in the adhesive bondline offering a potential method to directly monitor the structural health state of the bonded joint. However, concerns exist about (i) the potential reduction in joint performance due to the inclusion of the sensor itself, and (ii) the location of the sensor within the joint. A further, deeper look is taken on the use of piezoelectric

sensors, as much work has been focused on using them for structural health monitoring[12-15]. These sensors are small, lightweight, relatively low in cost, and can be used in a passive or active mode. In the active mode, they work as both actuators and sensors, thus providing an efficient means to excite and measure the electromechanical impedance response with a single device. The use of these sensors has evolved from surface-mounted sensing to embedded bondline sensing for bonded joint health monitoring. The initial application of these sensors was used for damage detection from impacts resulting in cracks and degraded structural integrity[16]. These were proven to be sensitive enough to detect barely visible damage, making them powerful health monitoring sensors.

In recent research, for composite structure joined with adhesives, small, piezoelectric sensors have been inserted in the bondline to evaluate joint integrity. These sensors monitor the local electromechanical impedance signature of the joint in a simple procedure that excites and records the response of the in situ sensor[17-18]. These sensors are transducers, based on the piezoelectric principle, which couples the electrical and mechanical properties. The piezoelectric effect occurs as a voltage is applied, creating an electric field that causes the sensor to lengthen or shorten according to the field polarity in proportion with the strength of the field. This piezoelectric coupling exists in both the in-plane strain (radial) direction and the out-of-plane strain (thickness) direction of the sensor and can therefore can simultaneously produce a response for loads occurring in these axes. The sensors are sensitive to minute changes in impedance which occur at high frequencies, well above the primary joint structural resonance. The minute changes serve as health indicators for the joint integrity. This capability can prove to be beneficial for an aircraft joint that is exposed to loads in multiple directions. For this application, they serve as embedded modal sensors, and the electromechanical impedance method is used to characterize the structural

integrity of the bonded joint. In place, the sensor acts as both a transmitter and a receiver, functioning in a pulse-echo mode. A tone-burst voltage signal applied to the sensor generates a wave through the structure. The sensor receives the wave and passes it to the impedance analyzer, which performs a fast Fourier transform (FFT) and plots the wave resonance in the frequency domain. The strength of the returned wave provides a mechanism to evaluate joint integrity through the impedance measurement. The impedance is a complex quantity, and the real part reflects clearly defined resonances that are indicative of the coupled dynamics between the embedded sensor and the frequency-dependent pointwise structural stiffness of the sensor in the composite joint. Thus, the real part of the electromechanical impedance measures the pointwise mechanical impedance of the structure, and the impedance spectrum is equivalent to the pointwise frequency response of the structure. As damage develops in the structure, in the vicinity of the sensor, the pointwise impedance changes. Furthermore, the stress state in the joint can vary with position. Therefore, piezoelectric sensors must be placed at critical joint locations in the structure, where they have high sensitivity to impending damage, but also where they have the least negative effect on the mechanical performance of the joint. The integrity of the sensor itself is independently confirmed using the imaginary part of the impedance. This part is highly sensitive to a local disbond of the sensor in the adhesive, but much less sensitive than the real part to structural resonances[19]. The resonances that are observed in the real part of the impedance comprise in-plane and out-of-plane sensor responses[20]. The in-plane responses directly relate to the shear and tension/compression joint capability, whereas the thickness or out-of-plane responses relate to the flexural or joint pull-off capability. The in-plane resonances are generally much lower in frequency than the out-of-plane resonances due to the larger dimension of the sensor in the disk radial direction when compared to its thickness direction.

For composite joints, much of the in situ joint health monitoring methods have been concentrated on single lap shear joints with tension loading producing shear stress in the bonded joint. For evaluating the health state of the bond, most of the efforts use a root mean square deviation index that compares the measured real part of the impedance for the primary resonance to the baseline value after repeated loadings are experienced on the joint. An arbitrary change of -2% or more in the primary impedance resonance may indicate a degradation in the integrity of the bonded joint. These efforts concentrate on the real impedance response of the primary radial mode response and normally consider only one load axis. The initial goal of this work is to analytically evaluate the effect of embedding a piezoelectric sensor in the bondline of a complex composite joint on the structural performance of the joint. The primary goal is to evaluate the joint health and the interaction of the sensor and its location within the joint bondline and determine how the joint performance/sensing capability is altered by moving the sensor within the bondline. After successfully completing the initial goal of this work, which was analytically determining the location of maximum strain in the Pi joint and showing minimal performance degradation from the addition of the sensor, it was decided to undertake a second phase performing experiments on a simplistic joint, specifically a single lap shear coupon. This was due to 1) the back-to-back joint providing two Pi bonds, 2) the additional bond in the Pi clevis/substructure, and 3) the laminate back-to-back bond. Each bond adds locations where the coupon could initiate failure making it problematic to fail the coupon where the sensor is embedded. A final phase of experiments is conducted on additional single lap shear joints and flatwise tension joints to fully evaluate the health monitoring capability of the bondline embedded sensors. This allows for evaluation of the monitoring capability when the applied joint loads occur in multiple axes and corrects deficiencies that were encountered in the second phase of experiments. It also allows for the expansion of

interpretation of the sensor's impedance response in a novel approach that may add to the prognostic capability of joint health monitoring.

Chapter 2 Phase 1 Efforts

While bonded, single lap shear joints are a common joint for laboratory investigations, more complex joining situations and requirements are typical of large-scale composite structure designs as seen in modern aircraft. There are many types of out-of-plane loading, such as those that result from curved section bending, fuel pressure, termination kick loads, and skin buckling. These out-of-plane loads result in a tensile stress across the adhesive bondline, which is much more difficult to react than the shear loads imposed on a lap joint. Composite structures commonly fail under these types of out-of-plane loads which result in both reduced adhesive performance and interlaminar tensile stress failure in the base laminate. To address these out-of-plane stresses and improve transfer of loads from the internal structure to the outer skin, developmental efforts have resulted in a unique composite joint design described as the Pi joint.

Pi Background

The composite Pi joint offers a unique and robust joining solution[21]. In aerospace structure, this joint is used to connect the substructure to the skins of the aircraft. The Pi joint gets its name from the shape of the preform which resembles the inverted symbol π. Due to the highly interlocked 3D weave architecture and the relative ease of application, the Pi joint is robust and tolerant to damage and flaws. The preform is woven flat and then folded into shape. The Pi composite bonded joint offers a solution that provides superior pull-off and shear load capability, mainly due to the 3-dimensional woven reinforcing fiber system. However, while offering superior "T" joint out-of-plane pull-off strength, relative to other conventional bonded joining methods, the joint is still susceptible to manufacturing defects at the bondline. Thus, this section describes an analytical investigation into the potential for the use of embedded piezoelectric sensors in a Pi joint to monitor out-of-plane bond health.

The Pi joint was extensively studied by Flansburg and Englestad to investigate enabling a robust design in the presence of impact damage and manufacturing flaws[22]. In this investigation, a parametric 2D planar finite element model of the Pi joint was used to vary geometric parameters such as widths and thicknesses of the actual joint, skin, substructure, and adhesive. The model was subject to a vertical pull-off load and constrained using roller supports on the skin, or base laminate, on each side of the Pi joint. While the Pi joint was loaded with a pull-off load, due to the constraints applied, a moment was also induced, as shown in Figure 1. Flaws in the skin and substructure were also considered in the analysis. As a result of the study, the simplest design changes leading to a reliable, robust Pi design were in geometry only. Furthermore, the most sensitive geometric parameters where the width of the Pi base and the thickness of the vertical Pi legs.

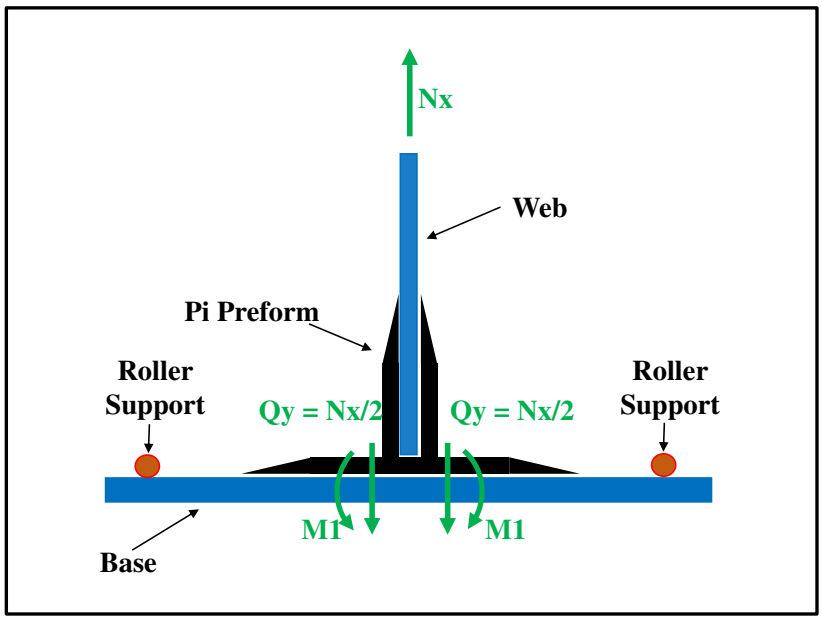

Figure 1. Pi joint loading.

While the Pi joint does see a complex state of stress in application, for the present study, investigating heath monitoring in this joint, it is desired to concentrate on a pure pull-off load with

no bending moment in the joint. This case is chosen as it represents the most simplistic loading for application and evaluation of structural health monitoring techniques using embedded piezoelectric sensors. To isolate the pull-off loading, a back-to-back Pi joint configuration has been developed, as shown on the freebody diagram, in Figure 2. With this configuration there is no moment transferred, and one half of Nx, the applied pull-off load, is transmitted equally through each leg of the Pi through the Pi base, the adhesive, and into the base laminate. This back-to-back configuration is used throughout the presented simulation. In this effort, the interest is to investigate the potential for health monitoring of Pi bonds using bondline embedded sensors.

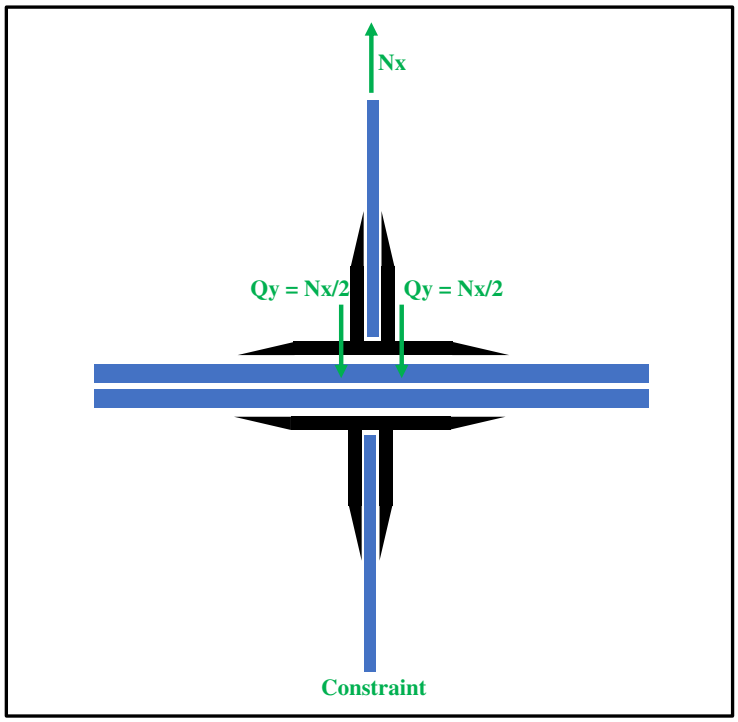

Figure 2. Pi joint back-to-back configuration freebody diagram.

The piezoelectric sensor, applied in this work for electromechanical impedance evaluation of the structural health of the bond, is a ceramic disk[16]. The sensor has a large radius compared to its thickness. The impedance resonances for the in-plane direction (shear) are lower in frequency than the out-of-plane resonances (pull-off) due to the thin, disk-shape geometry of the sensor.

Specifically, for the sensor under consideration, the radius is ~25 times larger than the thickness. Because of this, the impedance resonance for the in-plane load monitoring is generally measured in kHz and the out-of-plane resonance in MHz. In pristine structures, only the structural boundaries are reflected, whereas in damaged structures, reflections are also generated due to internal flaws. For health monitoring, impedance measurements would be repeated at specified time intervals throughout the service life and structural damage would manifest itself in a change or lowering in the impedance resonant response frequency. For example, flaws or disbonds would lower the resonant frequency or create a new resonance. For composites, the in-plane radial direction measurements are robust for large area monitoring, but in the thickness direction, or pull-off, the detection can only be made locally, directly in line with the sensor. Therefore, the sensor must be in a well-defined position in the area of pull-off load transfer through the joint.

The approach taken is to model the joint, under pure pull-off loading, with a piezoelectric sensor at the bondline between the Pi and the base laminate, for the purposes of (i) ensuring that the structural integrity of the joint is not negatively affected, and (ii) determining an optimal location for the small piezoelectric sensor. Thus, the focus of this study is to verify, analytically, the critical location of pull-off load transfer through the Pi joint and to evaluate any detrimental effects of embedding the sensor in the adhesive at this critical location.

Analysis

The Pi joint modeled is, in practice, fabricated by co-bonding the preform to a pre-cured laminate “web” and a pre-cured laminate “base” forming a “T” joint. The green Pi impregnated with the 5320-1 resin system[23] and two layers of FM300-2K[24] film adhesive is co-bonded under

vacuum bag pressure to consolidate and cure the joint. The Pi considered in this study has the dimensions shown in Figure 3.

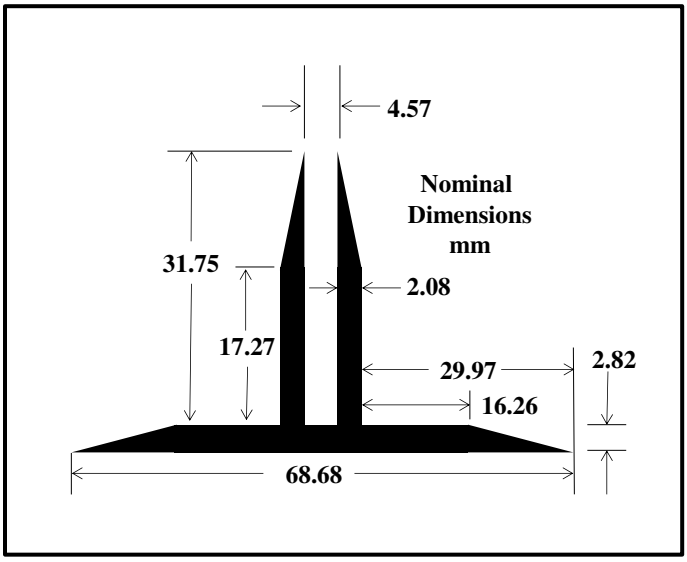

Figure 3. Pi preform dimensions (mm).

In order to understand the details of the Pi joint loading and investigate the viability of embedding piezoelectric sensors in the bondline between the Pi base and the structural skin base laminate, a finite element model (FEM) is built in MSC/Patran and analyzed with a pure pull-off static loading in MSC/Nastran. A detailed 2D plane strain FEM is used to model and understand the load transfer through the joint and to aid in sensor positioning, within the Pi to base laminate adhesive. The configuration for the model is shown in Figure 4.

The properties are derived for the xy plane, and the out-of-plane motion is constrained to zero. The model is initially constructed in the pristine configuration with no sensor embedded in the bondline. This configuration is used to understand the load transfer through the joint. Subsequently the FEM is used to evaluate effectiveness of sensor placement at various positions in the bondline. To completely investigate the loading, a static analysis simulation with non-linear adhesive properties is performed to fully evaluate the strain distribution in the adhesive.

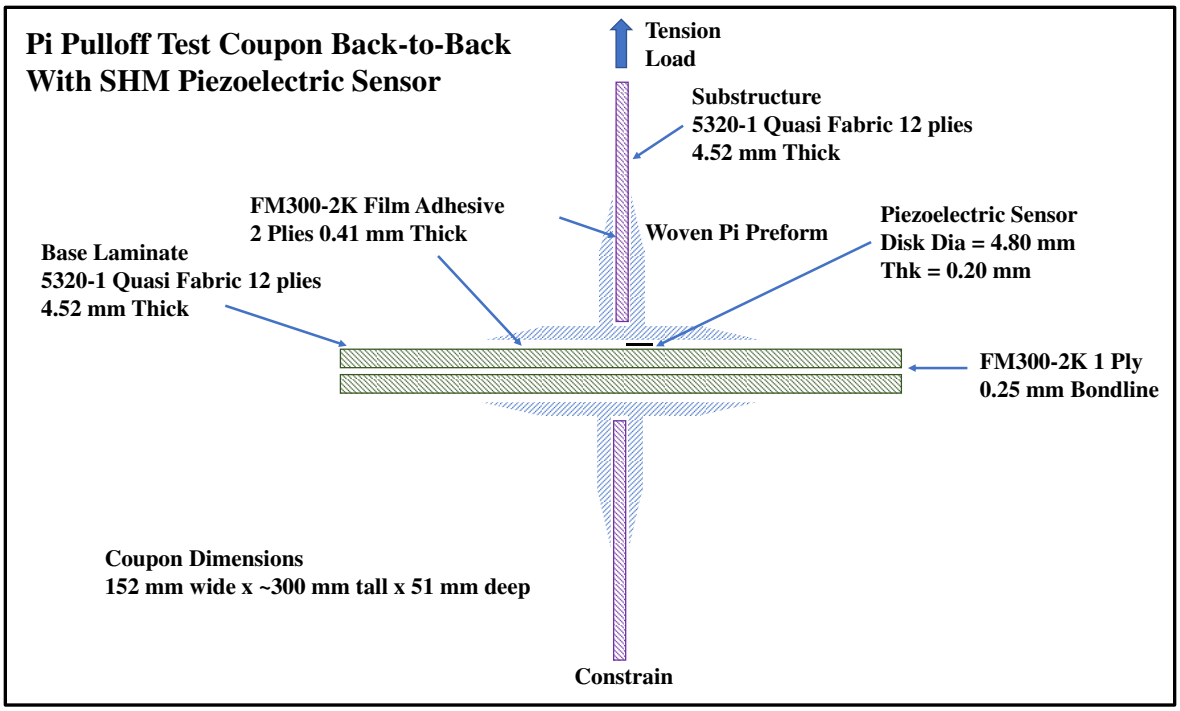

Figure 4. Pi back-to-back test configuration.

The 2D plane strain model more accurately represents the load distribution through the joint and can be used to facilitate a detailed evaluation of the effect of embedding the sensor in the bondline. Symmetry is employed between the Pi coupons and only the upper Pi is modeled. Initially, the location of the sensor is chosen directly underneath one Pi leg in the bondline to the base laminate. The reason for this location can be seen in the freebody load diagram of Figure 2, which shows that under the symmetric pull-off load 50% of the load is transmitted through each leg of the Pi, then the base, through the adhesive, and into the base laminate.

The substructure and base laminate consist of 12 plies of T650-35/5320-1 carbon/epoxy 8HS woven fabric prepreg (4.52 mm thick) in a symmetric quasi-isotropic $((45/0)_3)_S$ lay-up. In practice, the laminates are pre-cured and are co-bonded to the Pi legs and Pi base with 2 layers of FM300-2K film adhesive. The cured bondline thickness is approximately 0.41 mm. The Pi coupon is secondarily bonded to a similar Pi coupon forming a back-to-back coupon that is suitable

for pure pull-off loading with no induced bending moment. The dimensions of the coupon are 152 mm wide by 300 mm tall and 51 mm deep.

The FEM is shown in Figure 5. It is a 2D plane strain model taking advantage of symmetry in the y-axis (1/2 model) consisting of 4841 nodes and 4610 elements. The elements are 25.4 mm thick in the out-of-plane direction. Nastran allows for an isotropic material plane strain formulation. This is used for the FM300-2K adhesive elements. The orthotropic properties of the Pi, substructure, and skin are computed for the 2D plane. The elements are grouped by properties.

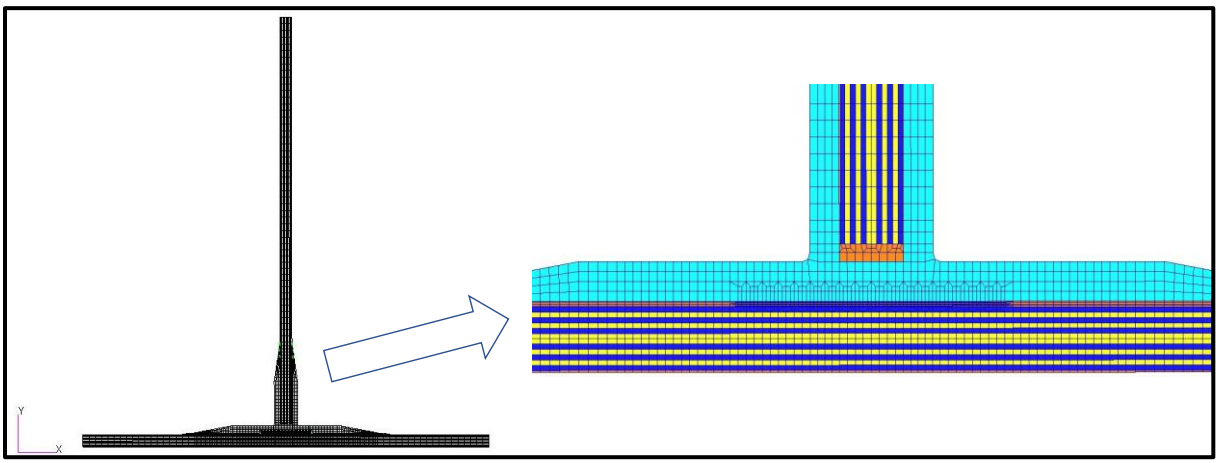

Figure 5. 2D plane strain Pi test coupon FEM.

Figure 6 shows a close-up view of the Pi joint to the base laminate. Note the fine mesh applied to the adhesive in the area underneath the centerline of the Pi past the clevis and leg. Adhesive elements are modeled connecting the Pi leg to the vertical substructure laminate. These elements represent the FM300-2K film adhesive between these adherends. The gap between the bottom of the substructure laminate and the Pi base is filled with the adhesive. To alleviate stress concentrations at the abrupt termination of the Pi base on the laminate, fillet adhesive elements are added to generate a smooth load transition.

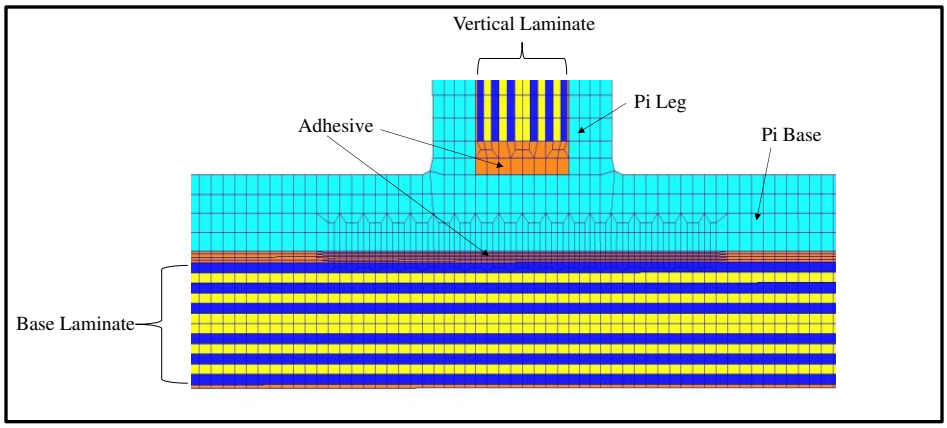

Figure 6. Pi joint FEM.

The 2D FEM is initially run in a pristine bondline configuration with no embedded sensor. The model is restrained in all nodal out-of-plane degrees of freedom (plane stress/strain). X-direction motion is restrained at all Pi joint centerline nodes. For symmetry, y-direction motion is restrained at the bottom layer of adhesive between the Pi back-to-back coupons. This allows for a pure pull-off load with zero moment. The pull-off load is applied at the top of the substructure laminate, pulling in the vertical direction. The analytical load was chosen to be 350 N/mm. To apply this load, the model is subjected to an enforced displacement in the y-direction of 0.25 mm. This provides for a smooth uniform load introduction into the joint. To fully evaluate the shear capability of the adhesive in the joint, the model is run using a non-linear static analysis solution. The adhesive is given non-linear material properties for this run. This simulation allows the adhesive to deform in a manner that reflects the actual stress strain curve when the adhesive exhibits plastic properties. The effect of non-linear geometry is also included in the simulation. This analysis with the added evaluation of non-linear material (adhesive) and displacement provides a complete characterization of the deformed state of the joint. Using this solution, the results of the applied load are fully understood in terms of displacement, adhesive strain, and permanent deformation. This run also allows for complete evaluation of the effect of embedding the sensor in the bondline of the joint.

The pristine FEM is then modified to include a piezoelectric sensor in the bondline. The mechanical properties of the disk are obtained from a commercially available ceramic lead zirconate titanate (PZT-5A) sensor[25]. To fully evaluate the effect of the sensor on the performance of the Pi joint under pull-off load, several piezoelectric sensor locations are modeled and analyzed. These sensor locations are shown in Figure 7 with the sensor model placed between the 2 layers of FM300-2K film adhesive. The sensor configurations analyzed are as follows:

1) One sensor – located in the center of the Pi joint directly under the clevis
2) Two sensors – one in each of the critical load transfer location under both Pi legs
3) One sensor – located in the left-hand side critical location under the left Pi leg
4) One sensor – located in the right-hand side critical location under the right Pi leg

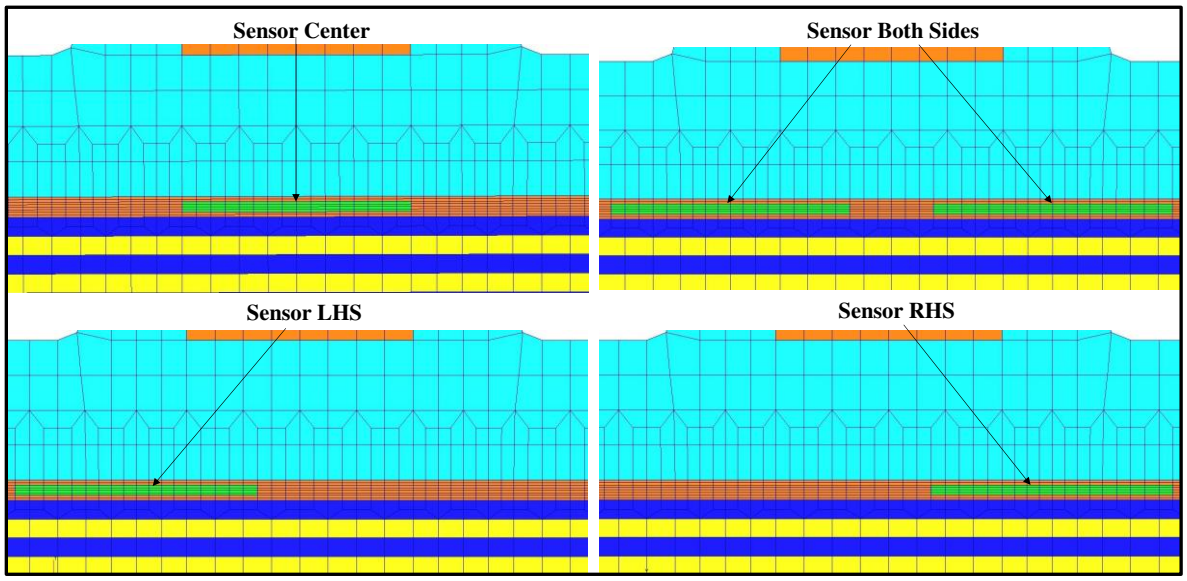

Figure 7. Sensor model locations in bondline.

The ceramic Piezoelectric sensor model is represented by the elements shown in Figure 7. The sensor has a diameter of 4.80 mm and a thickness of 0.20 mm. This sensor was chosen for its small footprint in the bondline. The FM300-2K film adhesive nominal bondline thickness is 0.41 mm. The sensor takes up half the bondline thickness. The 2D plane strain model represents

a slice cut through the center of the sensor disk. The adhesive is finely meshed in this area of the bondline where the critical load is transferred, and the sensor is embedded. This rectangular slice of the sensor disk is modeled by 72 elements (0.29 mm wide by 0.05 mm tall). This provides 4 elements through the thickness of the sensor, which is adequate FEM resolution as demonstrated and verified in previous analytical/test studies[14]. The sensor elements are modeled with 2D orthotropic plates and hard connected to the adhesive. The sensor is much stiffer than the adhesive. The simulations are performed with the inclusion of the embedded sensor under the same load condition as used for the pristine case. The analysis results serve as the primary evaluation of the critical location of joint pull-off load transfer and performance of this joint with embedded sensors.

Results & Discussion

The analysis results from the 350 N/mm load are presented and discussed in this section for each of the configurations. There are two purposes for performing the detailed analysis of the Pi joint under pure pull-off load; 1) Verification of the critical location of load transfer through the joint, and 2) Evaluation of any degradation to the structural performance of the joint in the presence of the sensor embedded in the optimal bondline position between the Pi base and the skin laminate.

To verify the critical location in the Pi joint under pure pull-off load, the pristine deflected shaped is examined first. The displacement results are shown in Figure 8, windowed in on the main constituents of the Pi joint. Both undeflected and deflected shapes are shown.

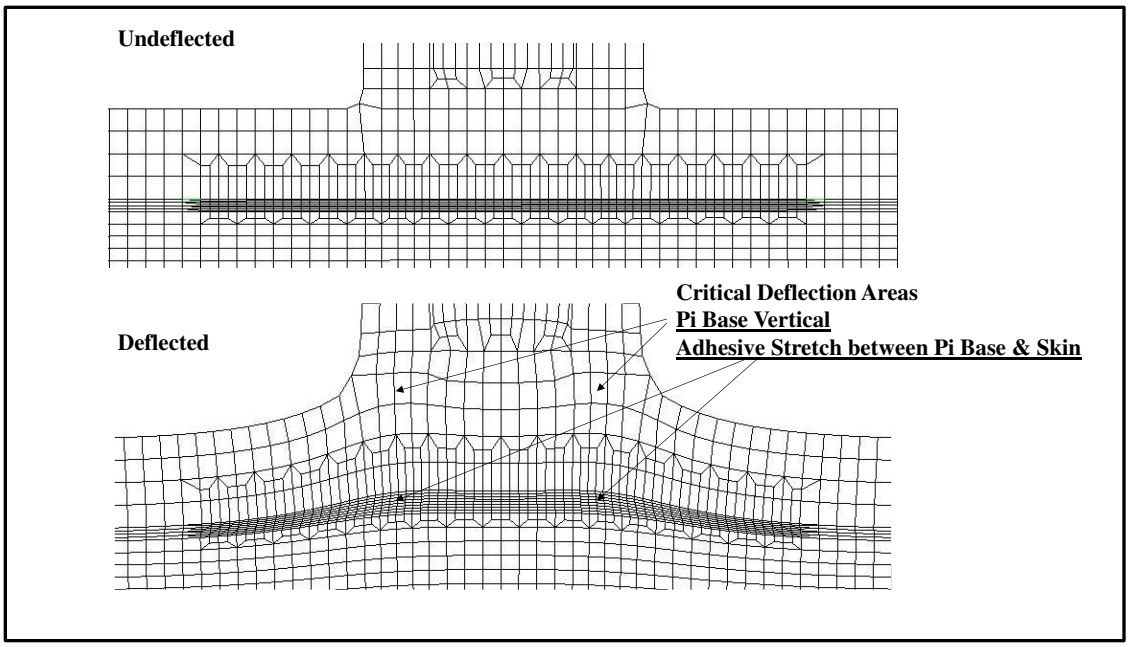

Figure 8. Pristine joint displacement results.

From examining the pull-off load deflections, the areas of critical displacement are the vertical stretch occurring in the Pi base under each Pi leg and in the adhesive under each Pi leg in between the Pi base and the skin laminate. Both critical deflection areas occur symmetrically under each leg of the Pi. This vertical stretch corresponds with the dominant $\frac{N_x}{2}$ load transfer shown on the freebody diagram in Figure 2. Since a sensor cannot be embedded directly inside the Pi base, the adhesive between the Pi base and the skin laminate under each Pi leg serves as a good sensor location selection. At this time, the selection is only based on displacement.

Stress/strain results are recovered for each constituent of the joint. These include axial strains, interlaminar tensile and shear stresses for the lamina and x and y strains for the Pi legs and base. For the adhesive, the shear strain and major principal strain are recovered. The maximum of each resultant quantity, for the pristine joint run, is shown in Table 1.

Table 1. Pristine Pi preform bonded joint analysis summary.

Analysis Results	Pristine
Vertical Laminate Axial Strain (μ-m/m)	
Tension	**42.16**
Compression	**-**
Vertical Laminate ILS (MPa)	**7.24**
Vertical Laminate ILT (MPa)	**-4.86**
Skin Laminate Axial Strain (μ-m/m)	
Tension	**1.68**
Compression	**-10.44**
Skin Laminate ILS (MPa)	**5.67**
Skin Laminate ILT (MPa)	**28.97**
Pi Leg Ex (μ-m/m)	
Tension	**50.04**
Compression	**-6.99**
Pi Leg Ey (μ-m/m)	
Tension	**62.23**
Compression	**-**
Pi Base Ex (μ-m/m)	
Tension	**29.97**
Compression	**-16.61**
Pi Base Ey (μ-m/m)	
Tension	**161.54**
Compression	**-0.56**
Adhesive Shear Strain (μ-m/m)	**201.00**
Adhesive Max Principal Strain (μ-m/m)	**284.00**

The results of the pristine joint indicate the highest stress under the pull-off load is the interlaminar tensile stress (ILT) at the base laminate. Composites are weak in the out-of-plane direction and the maximum ILT occurs under each leg of the Pi at the adhesive/skin interface (first 45° ply of the skin adjacent to the bondline). The other stresses in the joint constituents are low. The axial strains of the laminates are low. The Pi strains are highest in the y-direction of the base. This strain corresponds with the pull-off load with creates the ILT in the skin laminate after it transfers through the adhesive. The best indicator of the load transfer through the joint is the major principal strain in the adhesive. The shear strain in the adhesive is another indicator of load transfer through the joint. Both maximums for these quantities are shown in Table 1. The maximum adhesive

shear strain occurs at the lower interface of the vertical laminate and the Pi leg (symmetric, both sides). The maximum principal strain occurs, in the adhesive, between the Pi base and the base laminate, directly under the Pi leg. This critical location corresponds with the $\frac{N_x}{2}$ load transfer location shown in the freebody diagram, Figure 2. The adhesive principal strain distribution is shown in Figure 9 for the pristine joint.

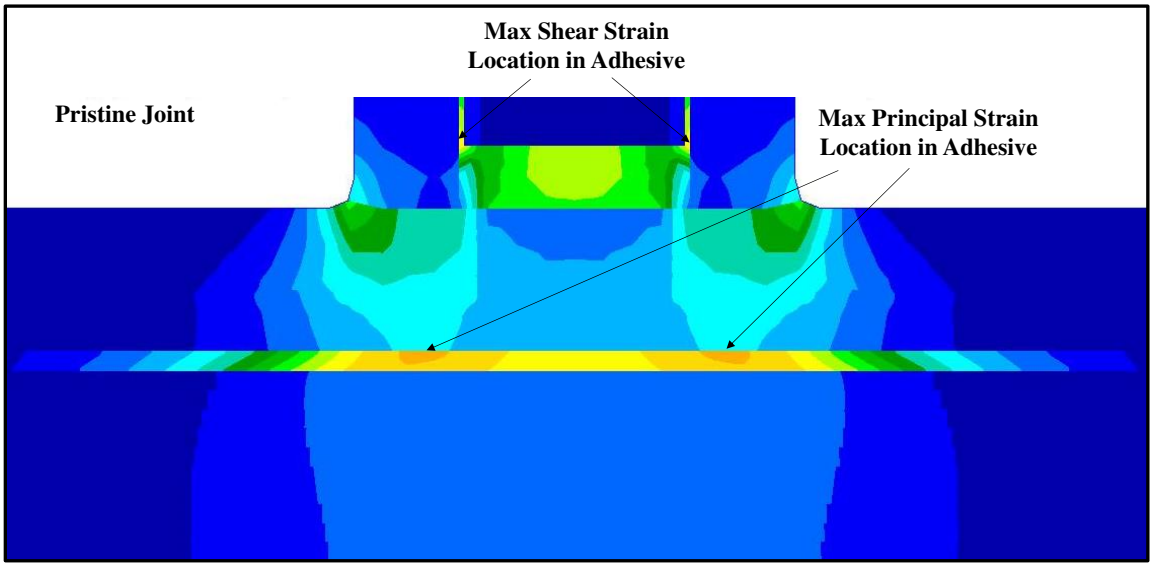

Figure 9. Pristine joint major principal strain distribution.

The critical location for pull-off load through the Pi joint is verified as the adhesive directly under each Pi leg. This location is critical for the highest strain through the joint and is also the adhesive location directly above the highest ILT stress in the base laminate. The location of highest adhesive shear strain is where the vertical laminate interfaces to the lower Pi leg, but this location does not capture the critical load transfer or the ILT of the base laminate. The sensor is embedded in the bondline between the Pi base and the base laminate at the selected locations previously shown. The sensor must be placed in the adhesive as it cannot be embedded in the Pi preform or in the pre-cured vertical or base laminate. The displacement is plotted for the embedded sensor configurations and evaluated against the pristine joint displacement. Figure 10 shows the

displacements of the embedded sensor runs. The presence of the sensor does not alter the displacement field in the Pi base, it only locally alters the adhesive deflection where it is embedded. Since the sensor is stiffer than the FM300-2K adhesive it lessens the displacement locally in the joint. This does not change the overall displacement of the Pi joint under the pure pull-off load.

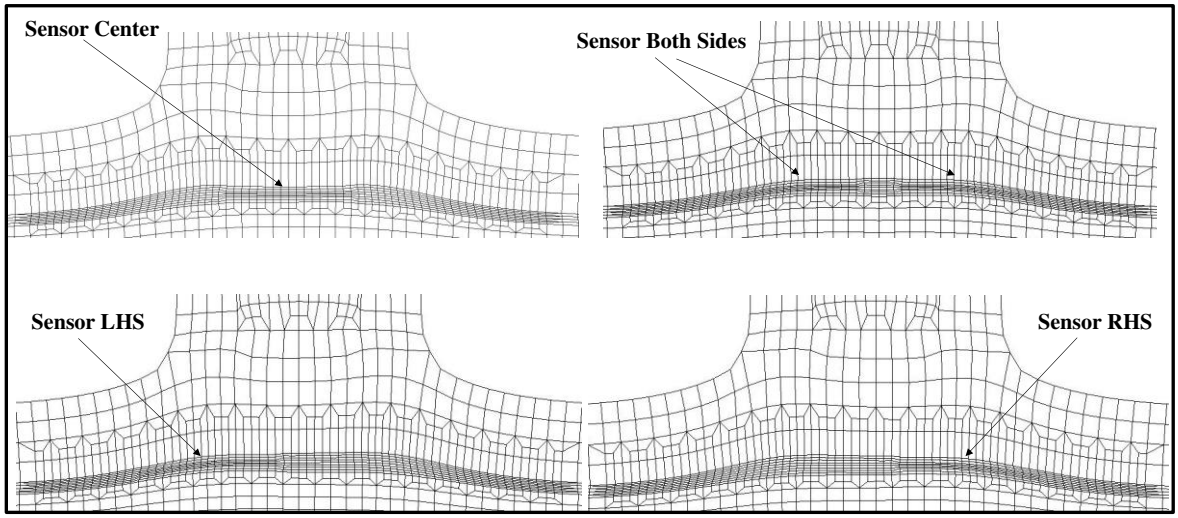

Figure 10. Pi joint pull-off load displacements with embedded sensors.

The stress and strain results for each configuration are compared to the pristine joint results. These comparisons of the resultant quantities are shown in Table 2 and are presented as percentage differences from the pristine joint run.

Table 2. Embedded sensor results in comparison to pristine.

Analysis Results	Pristine	% Difference From Pristine			
		Sensor Center	Sensor Both Sides	Sensor LHS Side	Sensor RHS Side
Vertical Laminate Axial Strain (μ-m/m)					
Tension	42.16	0.00	0.62	0.00	0.00
Compression	-	-	-	-	-
Vertical Laminate ILS (MPa)	7.24	-1.93	0.00	2.90	2.90
Vertical Laminate ILT (MPa)	-4.86	5.56	4.12	7.20	7.20
Skin Laminate Axial Strain (μ-m/m)					
Tension	1.68	4.17	2.98	4.17	4.17
Compression	-10.44	4.12	-2.39	-0.48	-0.48
Skin Laminate ILS (MPa)	5.67	-4.76	12.70	14.64	14.64
Skin Laminate ILT (MPa)	28.97	11.63	3.31	5.94	5.94
Pi Leg Ex (μ-m/m)					
Tension	50.04	-1.02	-3.56	-1.52	-1.52
Compression	-6.99	0.00	0.29	0.29	0.29
Pi Leg Ey (μ-m/m)					
Tension	62.23	-0.82	-0.40	0.00	0.00
Compression	-	-	-	-	-
Pi Base Ex (μ-m/m)					
Tension	29.97	-0.83	-4.24	-0.83	-0.83
Compression	-16.61	9.51	-31.49	-0.90	-0.90
Pi Base Ey (μ-m/m)					
Tension	161.54	-2.04	-1.10	0.32	0.32
Compression	-0.56	-5.36	-14.29	0.00	0.00
Adhesive Shear Strain (μ-m/m)	201.00	0.00	1.00	3.48	3.48
Adhesive Max Principal Strain (μ-m/m)	284.00	23.59	7.39	10.92	10.92

Reviewing Table 2 shows that the presence of the sensor in the critical location of pull-off load transfer (directly under the Pi leg) does not affect the strain in the Pi itself. The results for this location are the same (left-hand side or right-hand side sensor) since the loading is symmetric. For this location, the ILT stresses in the vertical laminate and the base laminate increase on the order of 7%. These increases are compared to the capability of the 5320-1 material system[23]. The pristine vertical laminate ILT is a relatively small value for this layup and a 7% increase is acceptable. The base laminate ILT increase is also acceptable. The ILS results in the base laminate show the largest increase but the pristine (initial value) is low, and the increase is acceptable. The adhesive shear and principal strains increase (~11% max principal strain) but the FM300-2K is a robust adhesive and this increase is acceptable based on the mechanical properties from the supplier[24]. Locating the sensor in the center location under the Pi clevis does increase the ILT stress in the base laminate

by ~12% and increases the adhesive maximum principal strain by ~24%. These are the largest increases over the pristine results for all sensor locations. The center sensor location does not affect the maximum shear strain at the vertical laminate to Pi leg. This is because of the symmetric sensor location to the shear transfer location. However, this is not the critical location for pull-off load through the Pi joint. Therefore, the center sensor location is not recommended due to these increases in stress and strain and the fact that the sensor would not measure the impedance at the critical location of load transfer through the joint. The other embedded sensor locations in the critical load path are acceptable from a stress/strain result evaluation.

The final comparison is the evaluation of the effect of the embedded sensor on the adhesive strain distribution. The adhesive's major principal strain distribution for all sensor locations is plotted in Figure 11 and compared to the pristine joint. The plot contours all use the same range and spectrum that corresponded to the maximum principal strain of 0.000351 *m/m* for the center sensor location.

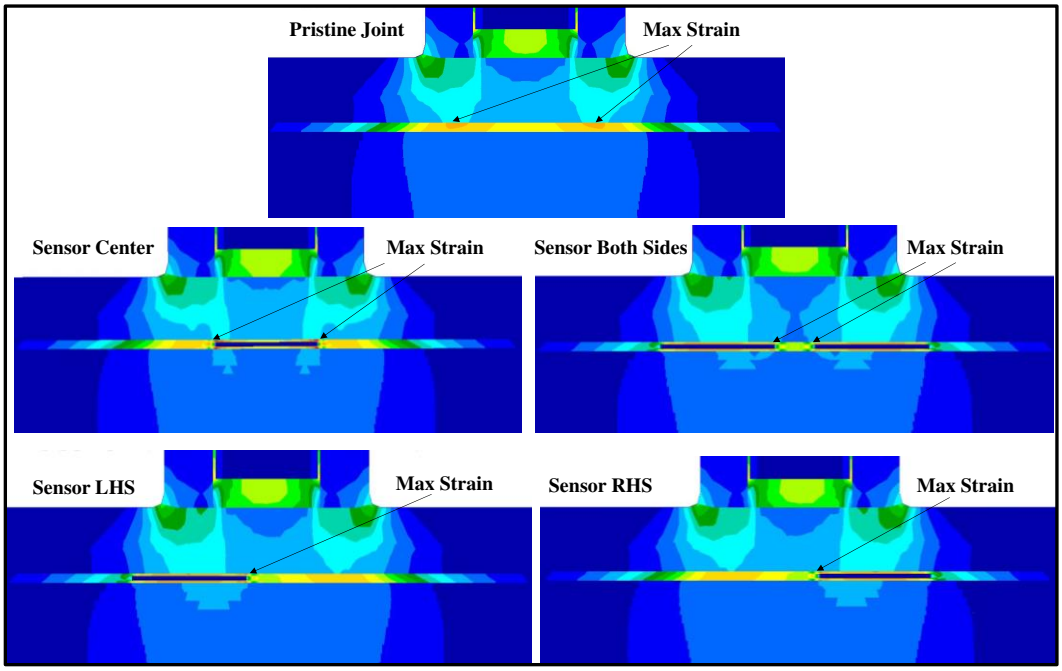

Figure 11. Major principal strain distribution comparison.

In comparing the four cases shown in Figure 11 to the pristine joint strain distribution, it is noted that none of the sensor locations in the critical load transfer area alter the adhesive major principal strain distribution or the shear strain maximum location at the vertical laminate lower interface. The maximum value increases due to the stress concentration around the top and bottom corners of the sensor. That is why the maximum value is located at the edge of the sensor nearest to the center of the joint. However, the value of principal strain for the embedded sensor corresponding to the pristine joint strain is the same for all embedded sensors in the critical load transfer location in the adhesive under the Pi legs between the Pi base and the base laminate.

Embedding the sensor in the center location does not provide the capability to measure the electromechanical impedance in the critical pull-off load transfer location. This location is not recommended for an embedded sensor. The other three sensor locations embed the sensor in the critical load transfer location and do not degrade the overall pull-off load performance of the joint. For practical purposes, due to the small size of the sensor, it is recommended to locate the sensor on the left or right-hand side critical load transfer location and not symmetrically on both sides. Embedding two small sensors in close proximity could be problematic to implement during joint fabrication. Having the sensor on either the left-hand side or right-hand side is expected to provide health monitoring for damage on either side. In the case of damage on the same side as the sensor location, the electromechanical impedance change is directly measured at this critical location. For the case of damage on the other side of where the sensor is located, it is expected that the load transfer will increase on the side of the embedded sensor, changing the electromechanical impedance.

In summary, the Phase 1 research efforts focused on the analytical application of embedded piezoelectric sensors in the bondline of a Pi joint between the base laminate and the Pi preform for

advanced health monitoring. A FEM simulation has been applied to verify the critical location of load transfer through the joint, in pure pull-off, and a preferred location of the sensor ensuring that the insertion of the sensor will not lead to early failure of the adhesive joint. The maximum value of the principal strain was observed to occur in the adhesive, directly under each leg of the Pi. The distribution is symmetric, and the maximum value is the same under each Pi leg. Thus, it was verified that the critical load transfer for a pure pull-off load is directly underneath the Pi legs in the adhesive between the Pi base and the base laminate. Embedding a piezoelectric sensor in this critical location between the layers of film adhesive either in the right-hand side or the left-hand side does not detrimentally affect the pull-off performance of the joint or alter the joint load distribution for this loading as witnessed in the pristine and embedded sensor max principal adhesive strain plots. Therefore, this location in the adhesive is predicted to be the optimal location to embed the sensor to monitor the structural health of the joint with applied pull-off load.

Phase 1 provided good insight into the use of piezoelectric sensors to monitor the structural health of a bonded composite Pi preform joint. After careful consideration, this joint was deemed too complex to proceed with experimental studies. This complexity is due to the multiple bonds in the back-to-back Pi joint, of which any could fail prematurely given any issue with the bonding process. The bonding process is complicated through the use of film adhesive which requires a vacuum bagging operation. The Pi joint also has multi-axis load capability and for this pure pull-off load, strict test load control is required to not introduce unwanted moments to the joint. Therefore, Phase 2 efforts will concentrate on a bonded composite single lap shear joint in a simple tension load, still allowing for development, evaluation, and improvement of joint health monitoring methodology, but using the analytical approach which successfully determined the preferred sensor location in the bond from the 2D plane strain FEM result evaluation.

Chapter 3 Phase 2 Efforts

The goal of this phase is to evaluate the joint health and the interaction of the sensor and its location within the joint bondline and determine if the joint performance and sensing capability is altered by moving the sensor within the bondline. Phase 2 covers the analysis and experimentation on the embedded sensor's ability to measure the joint health of a composite single lap shear joint loaded in tension.

Experimentation

Experiments are developed to demonstrate the ability of the embedded sensors to quantify the electromechanical joint impedance response during successive, incrementally increasing tensile loadings until joint failure. Two sensor locations within the lap shear joint are analytically evaluated to better understand the relationship between the sensor effectiveness and any negative effects on joint performance. These two locations are chosen since they exhibit the minimum and maximum shear stress in the bond during tensile loading. In order to establish a baseline impedance response, each sensor is tested in a free state, measuring the response of the primary radial and thickness resonances. The sensors are catalogued and then used in the fabrication of standard composite lap shear coupons created via a secondary bond cure, where each sensor is inserted between two layers of film adhesive that forms the bond between the composite adherends. The coupons are then tested with incrementally increasing loads until failure, while measuring the sensor impedance between loads. Pristine coupons are also tested to establish a baseline structural performance for comparison to the embedded sensor experimental results.

Sensor Free State Electromechanical Impedance

Several piezoelectric ceramic disk sensors from APC International are evaluated in the free boundary condition state to determine the radial and thickness electromechanical impedance

resonances. The sensor disks are solid, consisting of material 851, which is highly purified lead zirconate titanate (PZT) ceramic[25]. The disks are 5.8 mm in diameter and 0.20 mm thick and are selected for their small geometric footprint in the adhesive bond. The sensors are provided with 150 mm leads, soldered to the top and bottom sensor surface for connection to the network analyzer to perform voltage frequency sweeps measuring the electromechanical impedance. One of the sensors with the leads attached is shown in Figure 12. APC performed the wire soldering, and each delivered sensor is measured for thickness, diameter, and wire thickness. Of note, the thickness of the sensors is measured consistently at 0.39 mm, almost double the specified thickness in the catalog without soldered surface leads. The measured radial dimensions are at the specified 5.80 mm dimension and the red and black wire diameters are 0.50 mm.

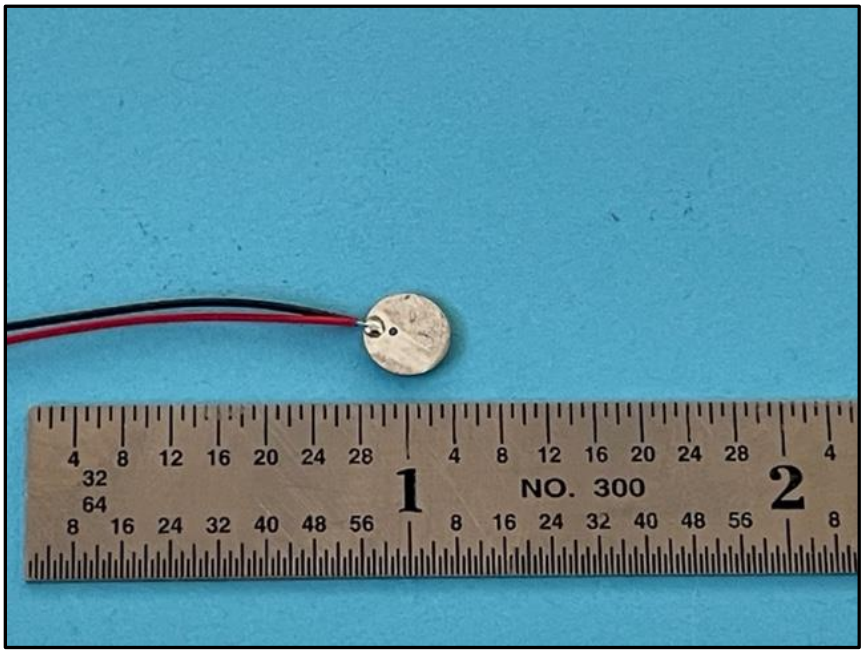

Figure 12. Piezoelectric sensor with leads attached.

Prior to performing the sensor free boundary state experiments, an analytical model of the sensor is created using the Ansys[26] code to simulate the impedance response. The model is shown in Figure 13 and is run in the free boundary condition state to match the experiment. The element

mesh density through the thickness is initially selected at 4 elements. Note that element density along the radial and thickness axes can be increased if model calibration is required. The SOLID226 20 node element is used to represent the sensor since it includes a voltage degree of freedom for impedance analysis.

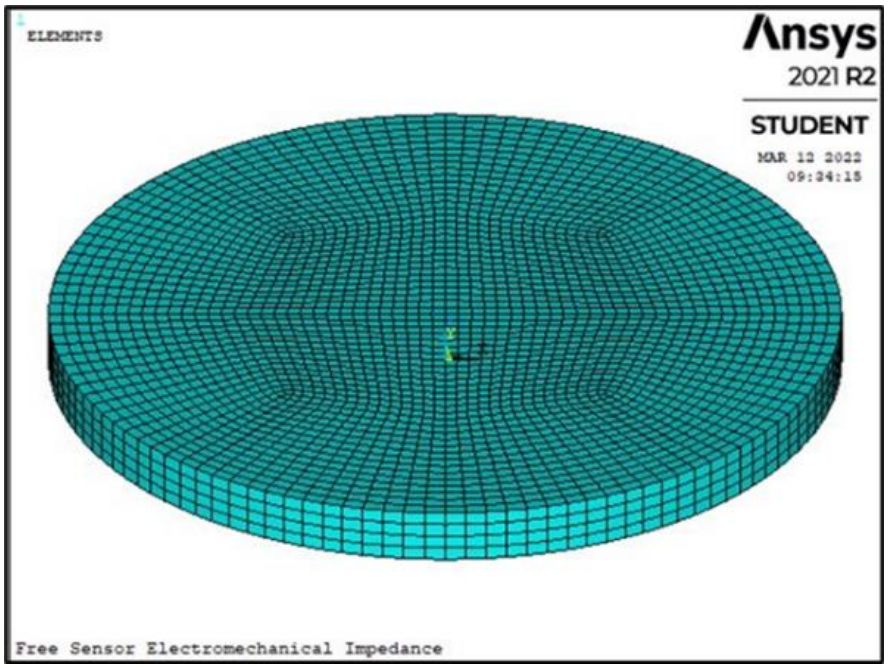

Figure 13. Sensor disk analytical model.

The mechanical and electrical properties representing the sensor are shown below:

$$[C_p] = \begin{bmatrix} 97 & 49 & 44 & 0 & 0 & 0 \\ 49 & 97 & 49 & 0 & 0 & 0 \\ 44 & 49 & 84 & 0 & 0 & 0 \\ 0 & 0 & 0 & 24 & 0 & 0 \\ 0 & 0 & 0 & 0 & 22 & 0 \\ 0 & 0 & 0 & 0 & 0 & 22 \end{bmatrix} GPa, \quad (1)$$

$$[\varepsilon_p] = \begin{bmatrix} 947 & 0 & 0 \\ 0 & 947 & 0 \\ 0 & 0 & 605 \end{bmatrix} x\ 10^{-8}\ F/m, \quad (2)$$

$$[e_p] = \begin{bmatrix} 0 & 0 & 0 & 0 & 12.84 & 0 \\ 0 & 0 & 0 & 12.84 & 0 & 0 \\ -8.02 & -8.02 & 18.31 & 0 & 0 & 0 \end{bmatrix} C/m^2, \quad (3)$$

where [C_p] is the stiffness matrix, [ε_p] is the dielectric matrix, and [e_p] is the piezoelectric matrix[27]. The density of the sensor material is 7600 kg/m^3. In order to represent the experiment, a coupled field harmonic analysis is run by applying a unit voltage differential between the upper and lower disk surface and recovering the generated charge that is summed to create the induced current. The current response and the applied unit voltage level are used to compute the electromechanical impedance. The frequency analysis was run at 1 Hz intervals in the range of 200 kHz to 6000 kHz to cover the radial and thickness response resonant frequencies. The free sensor analytical impedance response (real and imaginary) is shown on Figure 14 with the primary radial and thickness resonances noted.

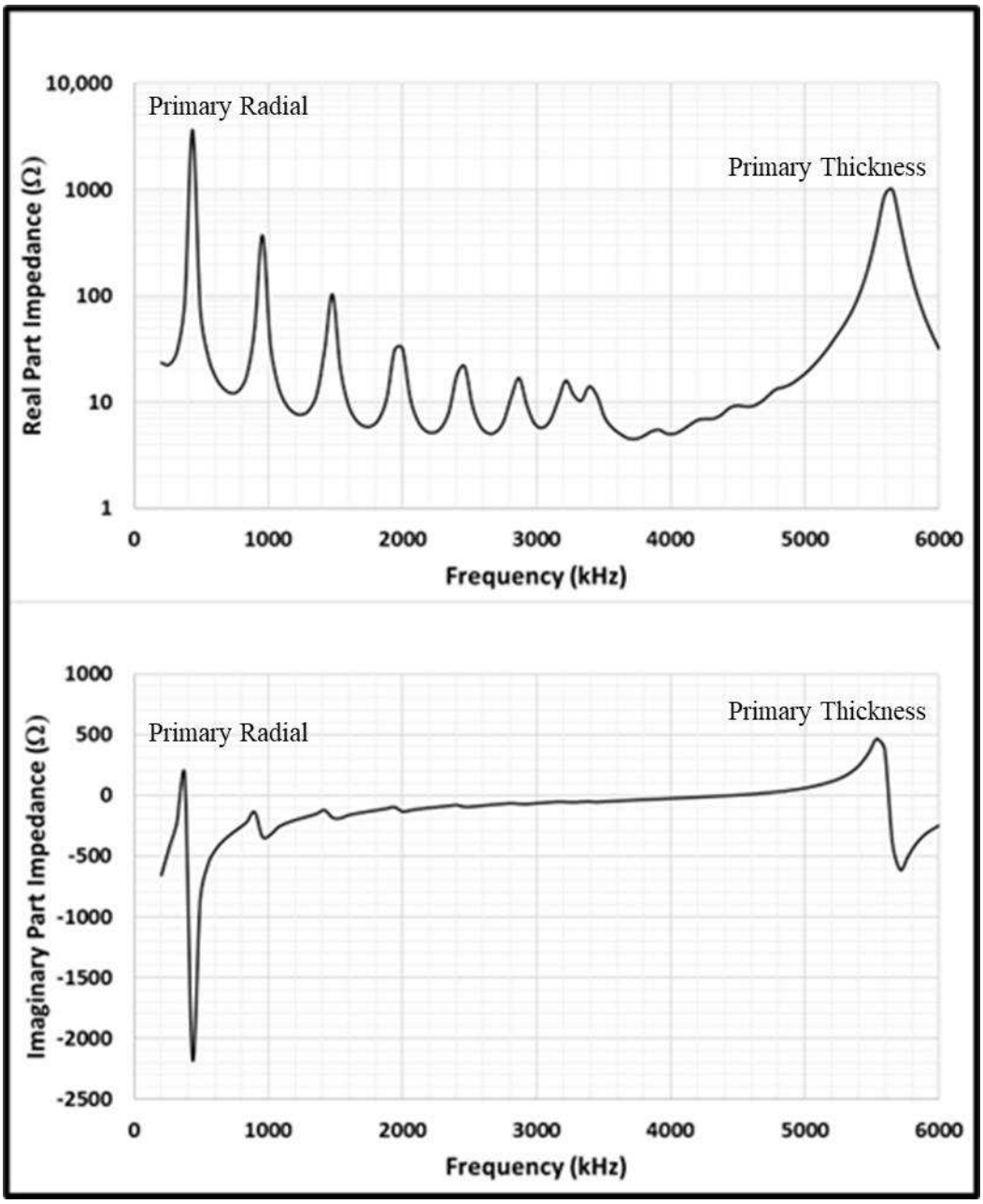

Figure 14. Free sensor analytical impedance response.

A total of 9 sensors are tested in the free boundary state by suspending each one by its lead wires through a rubber grommet. While this is not a totally free state in the radial direction, it offers a consistent baseline impedance response of each sensor prior to being embedded in the adhesive bondline of the test coupons. The sensor leads are connected to a Bode 100 Network Analyzer and a voltage is applied across the disk surface with one side acting as ground and the other being

excited[28-29]. The voltage is applied in a linear frequency sweep from 200 kHz to 20000 kHz. The frequency sweep takes about three minutes to complete and comprises 16501 frequency points. For the first sensor test, the sweep is run multiple times obtaining the same results. After that, each additional sensor is tested only a single time. For each run, the data is exported for plotting. The real part of the electromechanical impedance, for each of the 9 sensors, is plotted on Figure 15. The strongest peak is the 1st radial resonance occurring at an average of 384.5 kHz. The thickness resonance occurred at a higher frequency (5589 kHz), since the disk is thin compared to its radius.

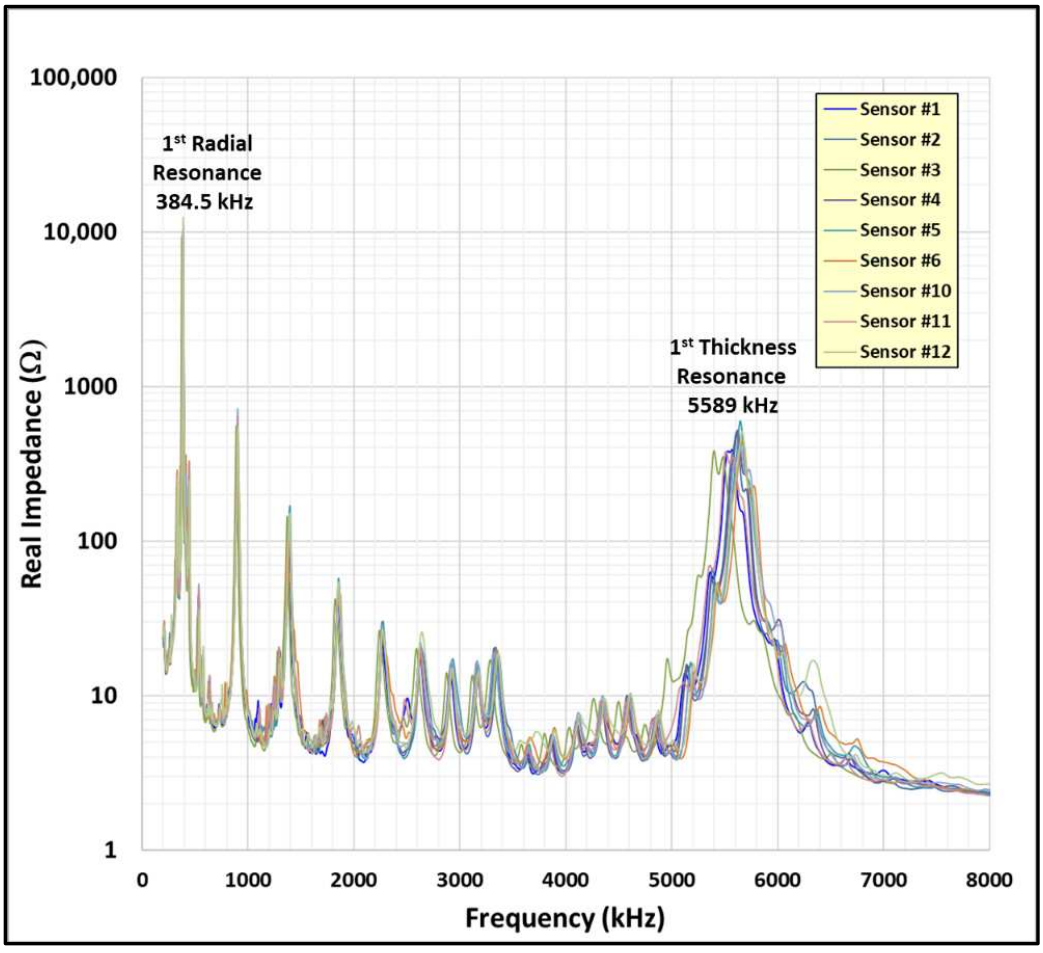

Figure 15. Free sensor real impedance response.

The 9 sensors tested are remarkably close in frequency response (resonance frequency and amplitude). This consistency in response is important, because it indicates that the sensors have

essentially the same impedance signature in the free state. Therefore, the results of the lap shear coupon impedance are not expected to contain any significant variances from the embedded sensor itself. Table 3 shows the primary mode resonance frequencies and amplitudes, with the averages noted at the bottom of the table.

Table 3. Free sensor measured impedance resonances.

Sensor	Radial (kHz)	Amplitude (kOhms)	Thickness (kHz)	Amplitude (Ohms)
1	381.2	7.8	5559	381.4
2	382.4	9.4	5604	490.8
3	375.2	9.2	5422	307.3
4	387.2	9.7	5604	452.9
5	388.4	10.7	5650	595.4
6	386.0	8.0	5650	398.3
10	388.4	9.2	5650	409.1
11	381.2	10.1	5513	378.1
12	387.2	12.4	5650	455.3
Average	384.5	9.5	5589	441.3

Single Lap Shear Coupon Design

In order to assess and quantify the adhesive bond stress distribution and the effects of the embedded sensor and its location within the bond, a FEM representation is created and analyzed prior to testing. The finite element model with the embedded center bond sensor is shown in Figure 16 and is a 2D plane strain detailed representation of the test coupon, which is the type of detailed analysis employed in Phase 1 efforts with the Pi preform joint.

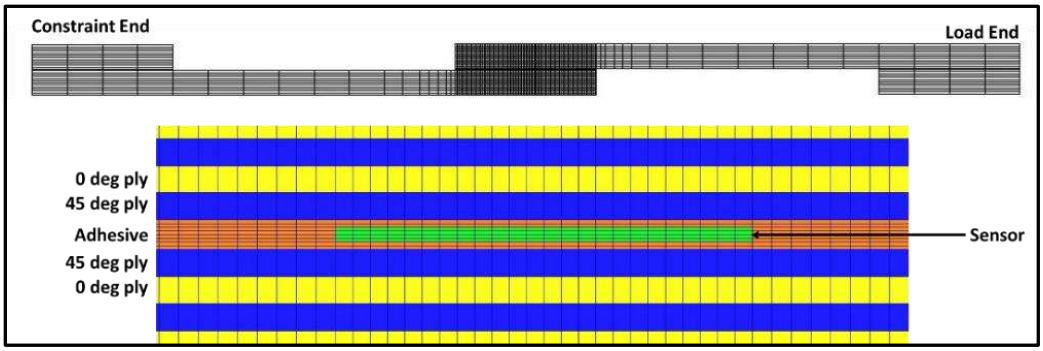

Figure 16. Test coupon static analysis FEM.

The sensor is directly connected to the adhesive elements at the nodal locations. The model is run statically with one end constrained and an enforced displacement applied to the free end. The sensor mechanical properties are the same as previously presented. The sensor took up approximately 4% of the shear bond area, so no significant joint degradation is expected due to a simple reduction in the bond area related to the embedded sensor. The simulation results showing the maximum shear stress distribution through the bondline are shown on Figure 17 for the pristine, center-embedded sensor, and load end-embedded sensor.

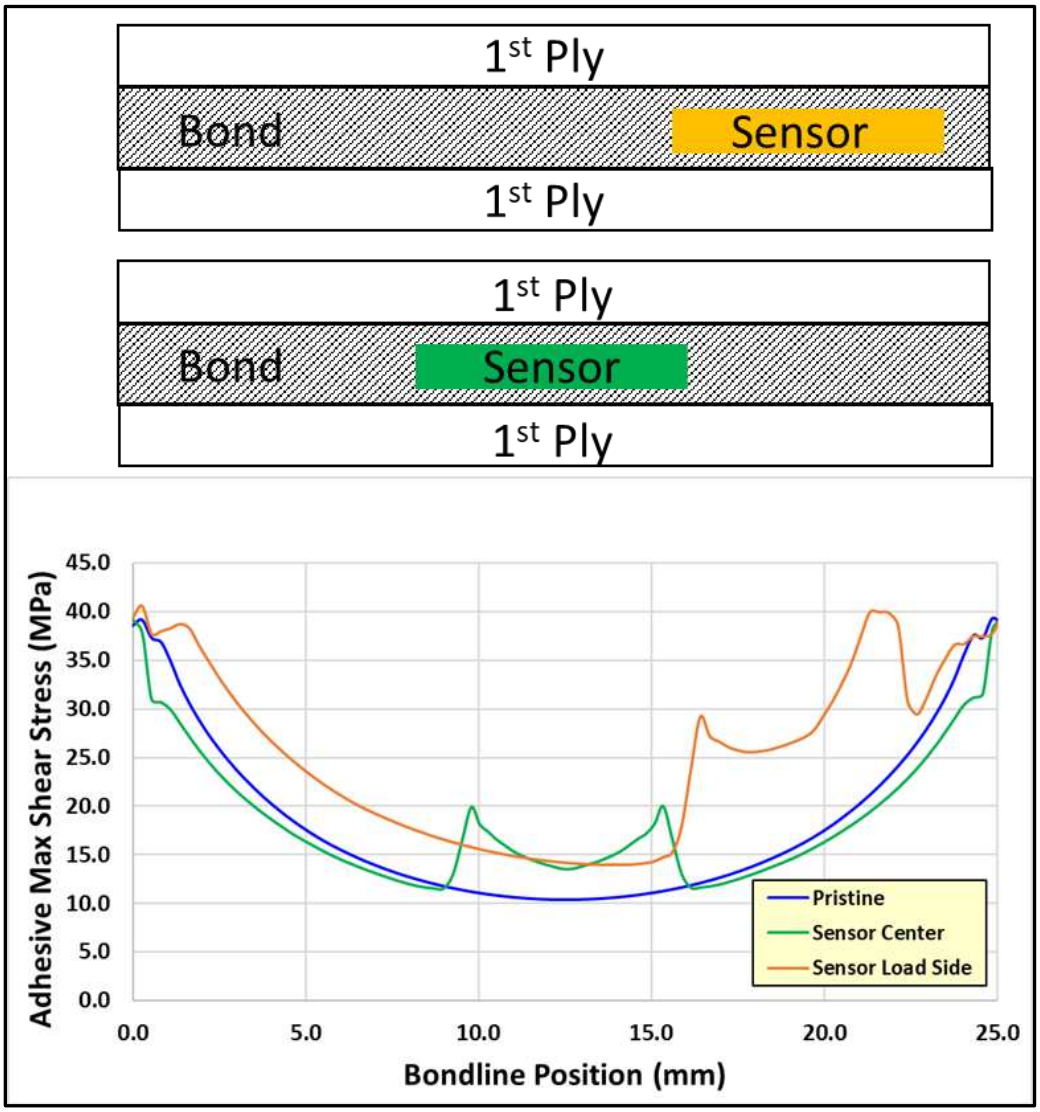

Figure 17. Analytical lap shear adhesive bond maximum shear stress distribution.

For the pristine case, it is seen that the maximum shear stress through the bond thickness occurs at the endpoints of the bond area. There is about a 4:1 ratio between the center and endpoint maximum stresses. The analytical results further indicate that the shear bond performance degrades when the sensor is embedded in the area of maximum shear stress as indicated on Figure 17 showing a higher maximum shear stress in the bond. There is a stress concentration at the edge of the bondline and adding the sensor to this location results in a higher imposed shear stress than the pristine case and may result in premature failure initiation. Embedding the sensor at the center of the bond (the minimum stress position) results in a similar sensor effect on the stress distribution, but due to the location, the stress intensification at the sensor edges does not approach the stress seen in the pristine case at the bond endpoints. Based on these results, the bondline sensor locations for testing are selected to be the center position and the load end position. This covers the range of minimum to maximum sensor effect on the bondline shear stress distribution.

Adhesively Bonded Composite Single Lap Shear Coupon Fabrication

Static shear testing is performed on single lap shear test coupons with, and without, embedded piezoelectric sensors in the bondline. The coupons are fabricated with composite adherends that consisted of 12 plies of T650-35/5320-1 carbon/epoxy 8HS woven fabric prepreg in a quasi-isotropic layup ((45/0)3)S. The laminates used the Solvay CYCOM 5320-1 toughened epoxy resin system and are vacuum-bag cured, out-of-autoclave, at 177°C. This resulted in an adherend thickness of 4.5 mm (0.376 mm thickness per cured ply). Figure 18 shows the layout of the adherends before the application of the adhesive.

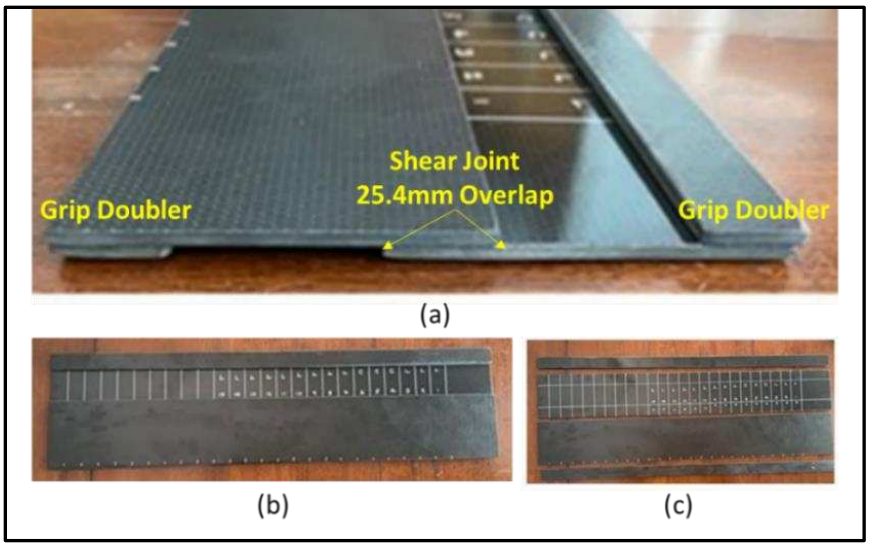

Figure 18. Adherend layout before adhesive cure: (a) side view, (b) plan view, (c) part view.

The adherends are vacuum-bagged and secondarily bonded together with two layers of FM300-2K film adhesive at 121°C for 90 minutes. Figure 19 shows the bonded coupons after the adhesive cure, but before cutting into individual test coupons. Individual coupon dimensions are shown on Figure 20.

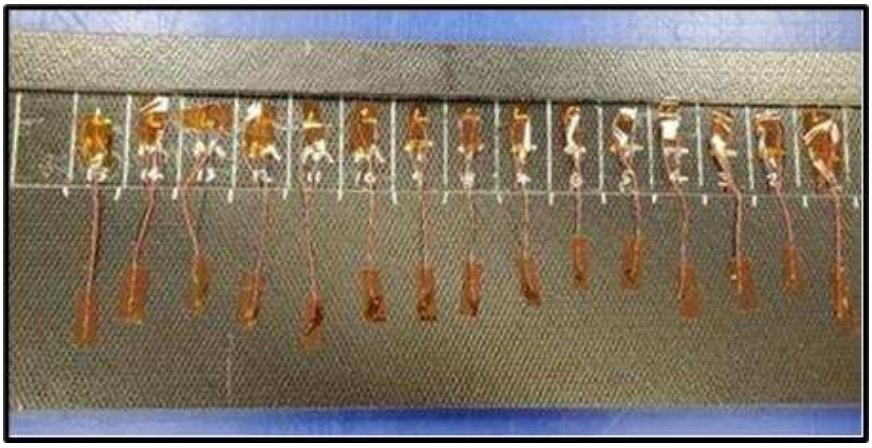

Figure 19. Bonded coupons after adhesive cure.

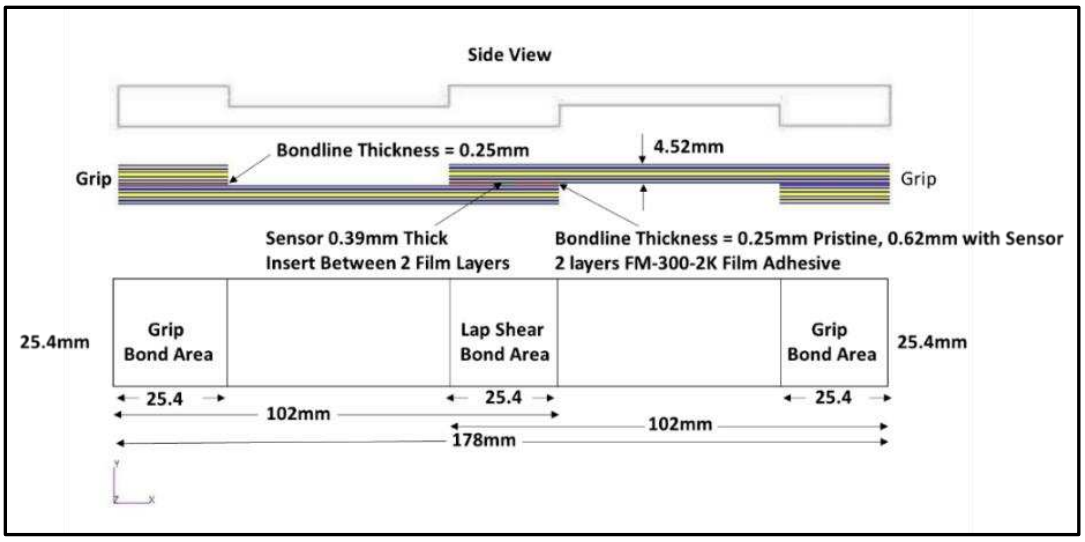

Figure 20. Lap shear test coupon dimensions.

A total of 5 pristine- and 9 bondline-embedded sensor lap shear test coupons are fabricated. The pristine coupons (no embedded sensor) were tested to establish a baseline failure load for comparison to the failure load with the bondline-embedded sensor. The sensors are placed between the two layers of film adhesive to encapsulate the sensor uniformly and consistently in the bond. The sensor locations within the bondline are varied, as shown in Figure 21. The locations are selected based on the simulation results and this is carried out to evaluate the sensitivity of the impedance measurement to the sensor location and to the bond shear stress distribution.

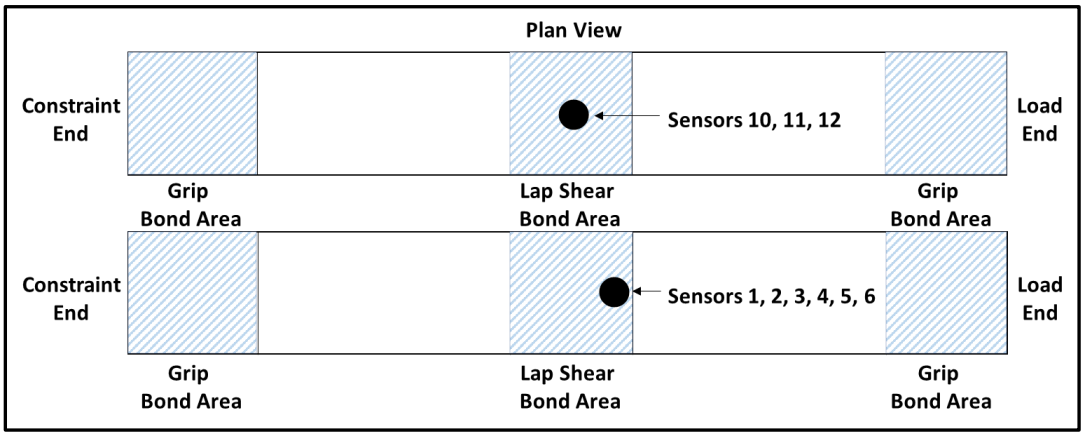

Figure 21. Test coupon embedded sensor locations.

The completed test coupons are shown, in Figure 22, prior to tensile testing. Note that the silver pen-marks (circles) indicate the position of the sensor embedded in the bond and are not the actual sensors. The shear joint bondline thicknesses are measured using a micrometer, resulting in a consistent thickness of 0.62 mm.

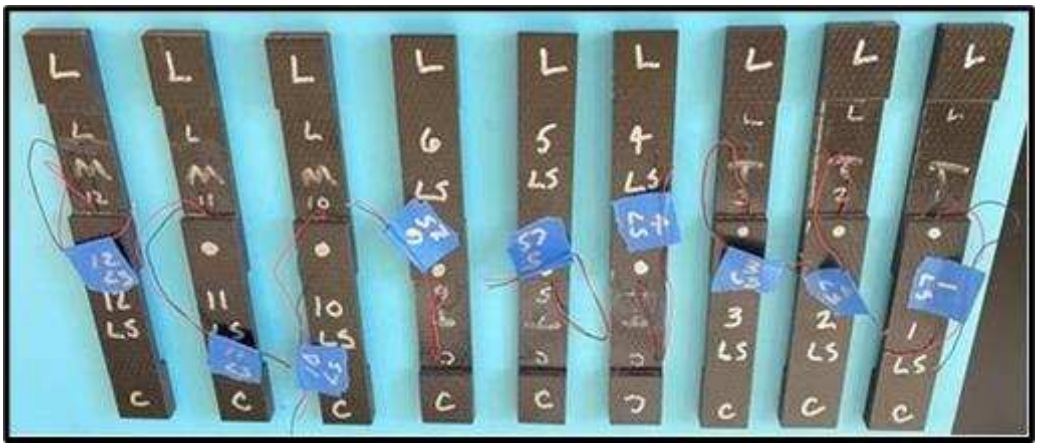

Figure 22. Embedded sensor lap shear test coupons.

Coupon Tensile Load and Impedance Testing

The ASTM D5868 FRP single lap shear test procedure is followed, loading the coupon in tension, producing shear stress in the bond[30]. The coupons are loaded at a rate of 1.25 mm/minute using the applied test system (ATS 900) universal testing machine. This is a deviation from the recommended load/deflection rate of 13 mm/minute since the embedded sensors must be unloaded between each applied load to measure the impedance. Given this lower load rate, each coupon test takes about 4 minutes to complete each incremental static loading, allowing the operator to better control accuracy of attaining the setpoint loads. After completing each load step and returning to zero load, the coupon is removed from the test machine and the embedded sensor electromechanical impedance is measured in a freestanding, unloaded state, similar to the baseline test. Coupon impedance is measured outside the test machine in a free state due to the effect of the test machine grips on the impedance measurement. The sensors are believed to be sensitive to the

characteristics of the test machine grips from both the mechanical loading and the electrical properties of the metal. The measured impedance of the coupon installed in the load machine did not correlate to the freestanding results; therefore, each coupon is removed from the test machine between incremental load applications, and its impedance was measured in the freestanding, unloaded state. For testing, each coupon is first loaded to 4448 N then unloaded for impedance measurement, followed by reinsertion in the test grips and reloading to a load value 445 N higher than the previous increment, until failure. The test procedure is shown in Table 4.

Table 4. Single lap shear coupon test procedure.

Test Procedure	
Step	**Action**
1	**Measure embedded sensor impedance.**
2	**Insert coupon into the universal test machine.**
3	**Photograph the test specimen.**
4	**Apply an initial load of 4448 N, unload, remove coupon and measure impedance.**
5	**Reinsert the coupon into the test machine and load to 4893 N (an increment of 445 N), unload, remove and measure impedance.**
6	**Repeat sequence adding 445 N until failure.**
7	**Record individual peak loads (and average).**
8	**Record test load/deflection and save to an Excel file.**
9	**Photograph broken specimens.**
10	**Identify failure mode type per ASTM 5573-99[31].**

Figure 23 shows the embedded sensor coupon, #11, in the test fixture. The clip gage extensometer is attached to the coupon to measure the shear bond axial displacement during loading. The displacement is recorded along with the applied load.

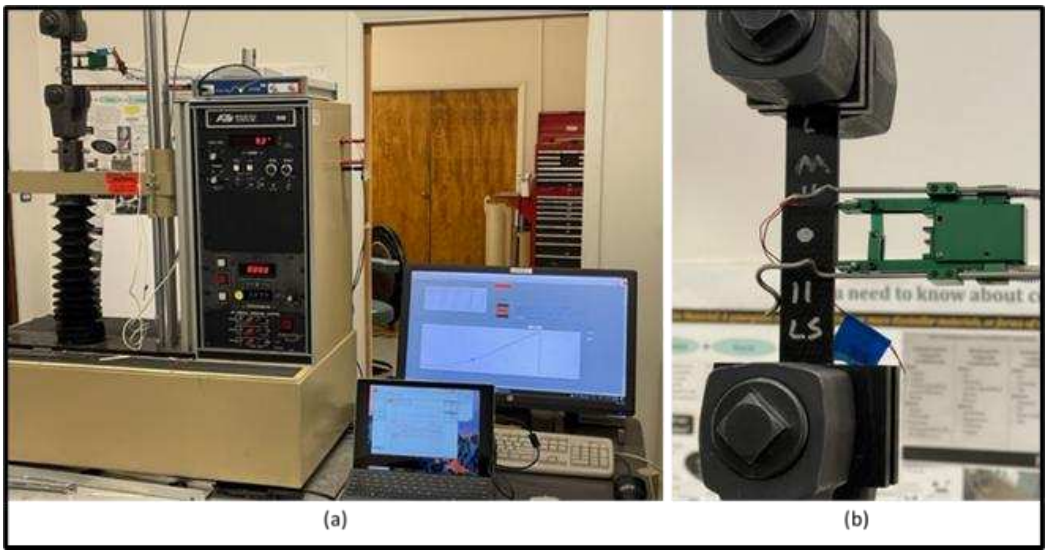

Figure 23. ATS 900 test system with coupon loaded. (a) test setup, (b) coupon closeup.

Results

The results for these experiments are presented in this section and the evaluation is presented in the Discussion section of this chapter.

Pre-Test Baseline Test Coupon Electromechanical Impedance Measurements

The electromechanical impedance of each embedded sensor coupon is measured prior to lap shear testing. This established a baseline pre-load impedance and is also used to compare to the free sensor's impedance. This comparison established the difference between the sensor free state impedance and the lap joint-embedded sensor's impedance. As a result of these baseline tests, it is noted that only four of the nine embedded sensors are fully functional. The five coupons with inoperable sensors had no clear radial or thickness impedance resonances in the expected

frequency range of interest. This may be due to problems occurring during the coupon bonding operation and demonstrates a need for redundant sensors if these are used in aircraft film adhesive bondline integrity monitoring. Due to this result, only the four coupons with functioning sensors are tensile tested. These are coupons 2, 3, 11, and 12. Figure 24 shows a plot of the real and imaginary components of the embedded sensor impedance. These embedded sensors are averaged and show a consistent impedance response with the first radial impedance resonance at 656 kHz and the first thickness resonance at 5200 kHz. Figure 25 shows an example of one of the inoperable sensors compared to the average of the operable sensors. As seen in the figure, there are no appreciable radial or thickness resonances in the frequency range, consistent with the operable sensors, suggesting either a failure during the cure of one of the wire leads, or of the brittle piezoelectric sensor itself.

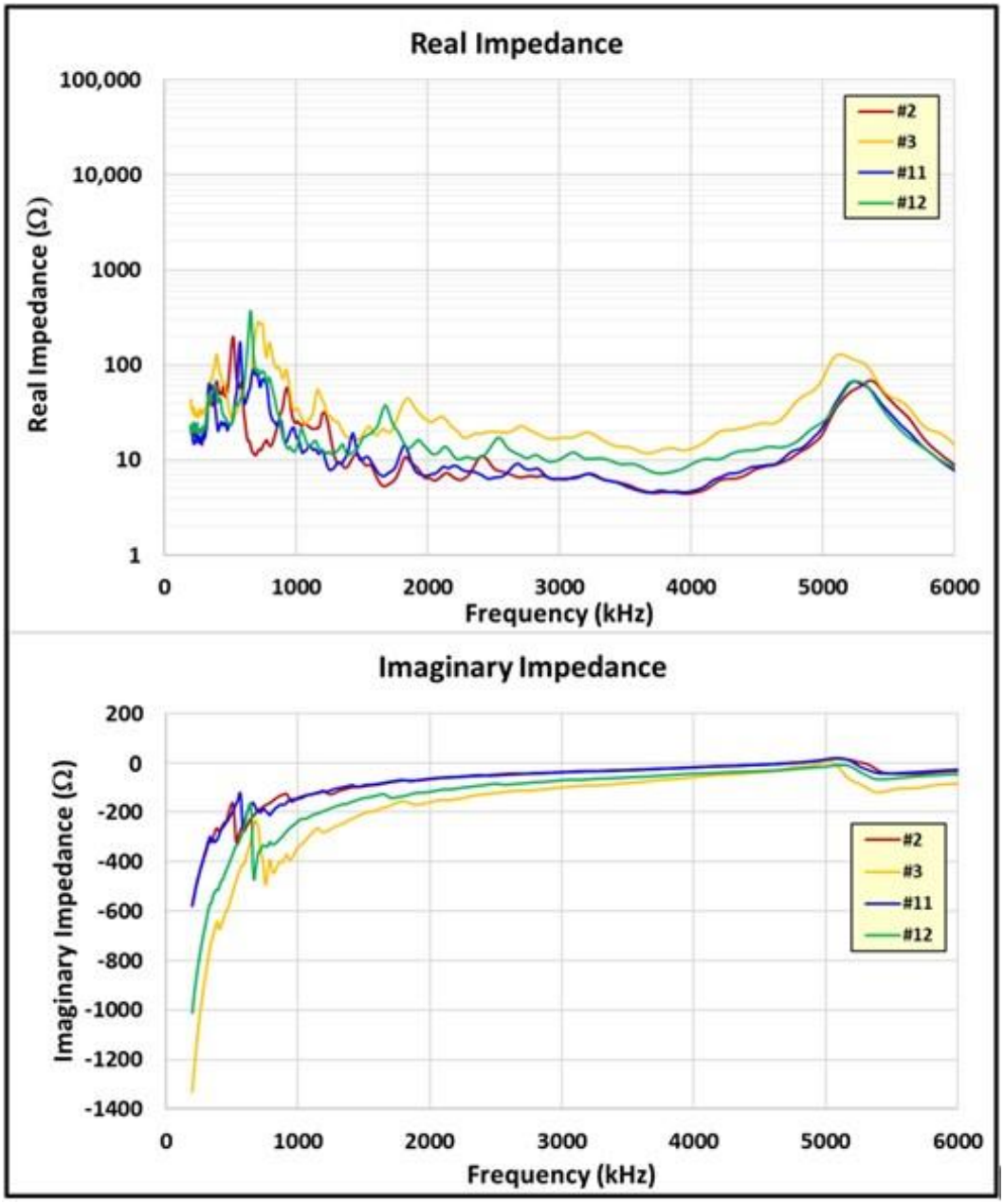

Figure 24. Pre-load test embedded sensor impedance resonances (sensors 2, 3, 11, 12).

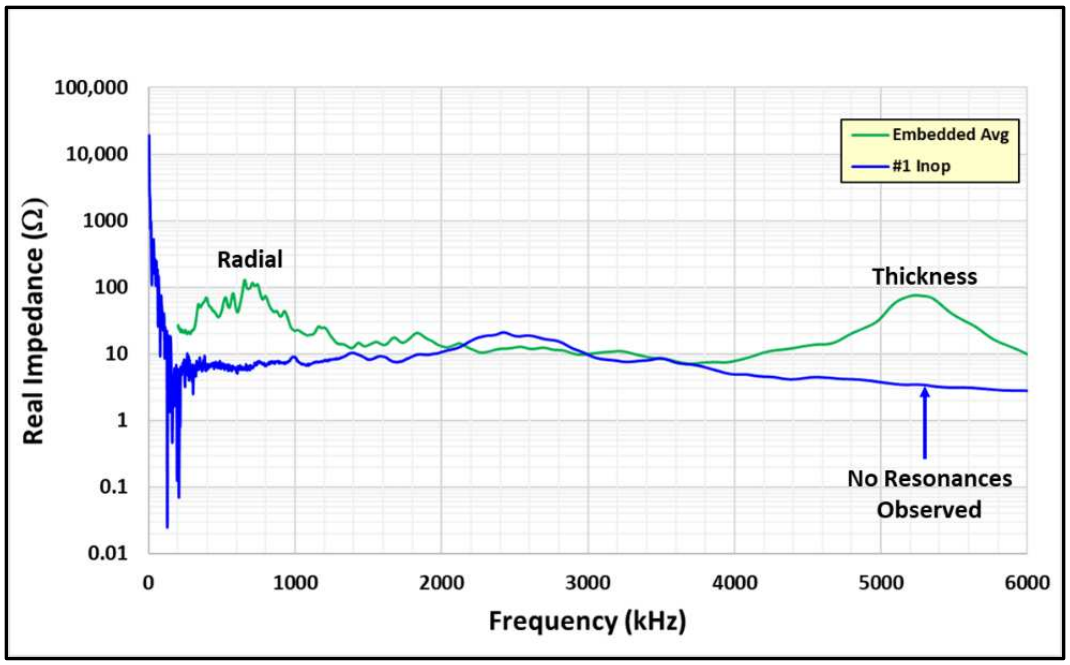

Figure 25. Inoperable embedded sensor #1 impedance response.

Pristine Coupon Tensile Load Test Results

The coupons without sensors (5) are tested following the procedure in the previous section with the exception of the second applied load, which used an increase of 2224 N instead of 445 N. For each additional load, the level is increased by 445 N until failure occurs. The coupon is not removed from the test machine between loads. The average failure load for the pristine coupons is 10280 N and a bondline stress of 15.9 MPa. For pristine coupon 2, Figure 26 shows the load versus bond displacement on the final load increment to failure with an 'x' on the curve depicting the maximum load achieved on that test. The other pristine coupons exhibited similar load versus displacement plots. The failures were mixed-mode with mostly cohesive failures (in the adhesive). One of the coupons failed in a composite adherend fiber tear.

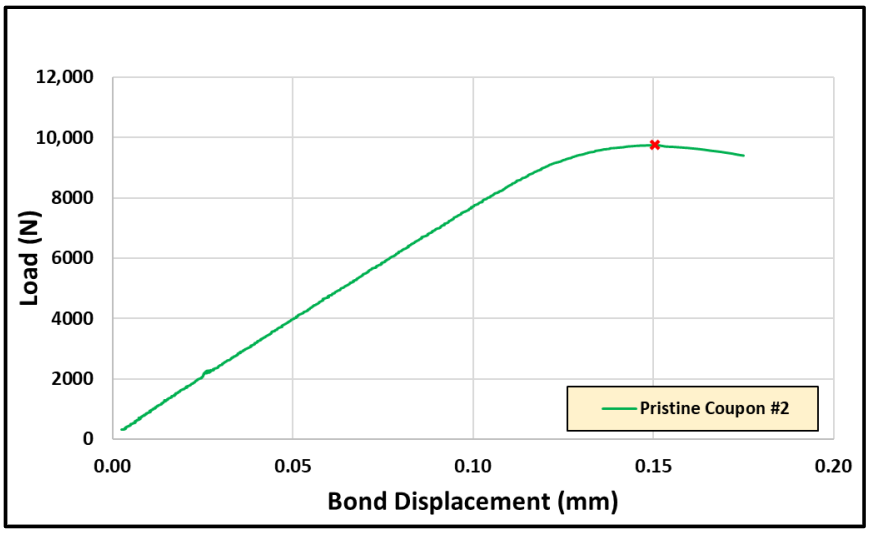

Figure 26. Pristine test coupon #2 load versus displacement (final load increment).

Embedded Sensor Coupon Tensile Load Test Results

An example of the applied sequential loadings for an embedded sensor coupon is shown on Figure 27. The sample (with sensor #11) failed at 6630 N on the 7th load increment exhibiting a mixed mode failure (primarily cohesive but some thin layer adhesive). The failed coupon 11 is shown on Figure 28. The cohesive failure mode indicates that failure originated in the bond adhesive, and the thin layer adhesive failure aspect indicates that the failure was close to becoming an adhesive failure at the bond interface. The adhesive exhibited a high degree of porosity, which was noticeable by the incomplete adherend surface coverage with adhesive. The brittle sensor was fractured into multiple pieces.

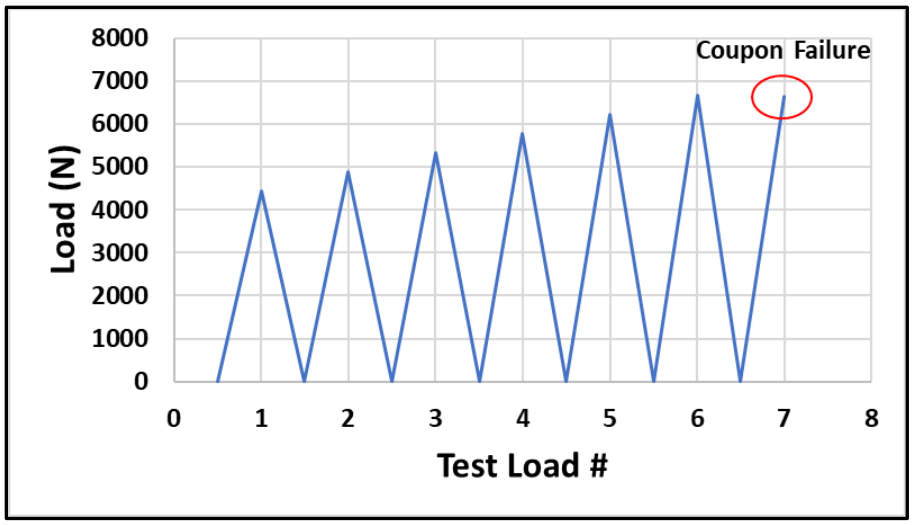

Figure 27. Example coupon (11) test loads.

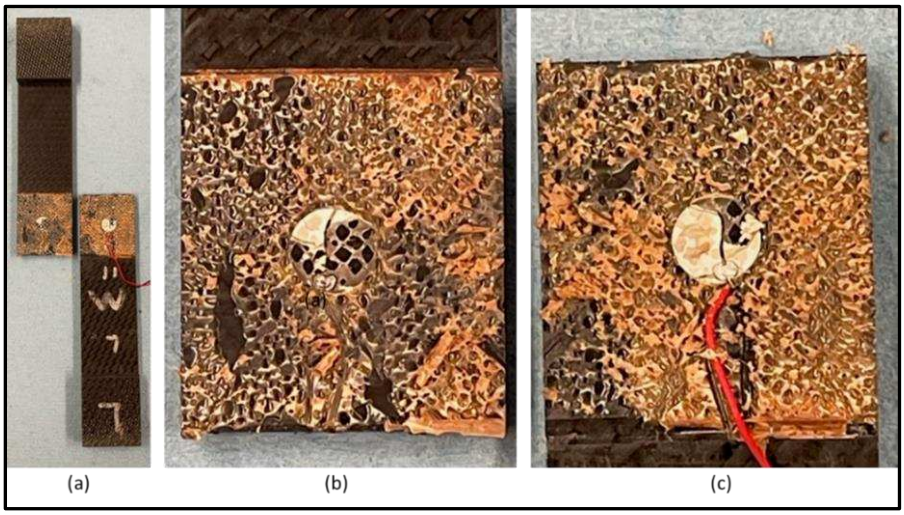

Figure 28. Coupon 11 cohesive failure photos with broken sensor disk. (a) both adherends, (b) top adherend, (c) bottom adherend.

The embedded sensor coupons failed at an average load of 6510 N after six load increments, corresponding to a bondline stress of 10.1 MPa. A plot of the final failure load test versus bond displacement for the tested embedded sensor coupons is shown on Figure 29. The ‘x’ on each curve indicates the peak load achieved on the coupon.

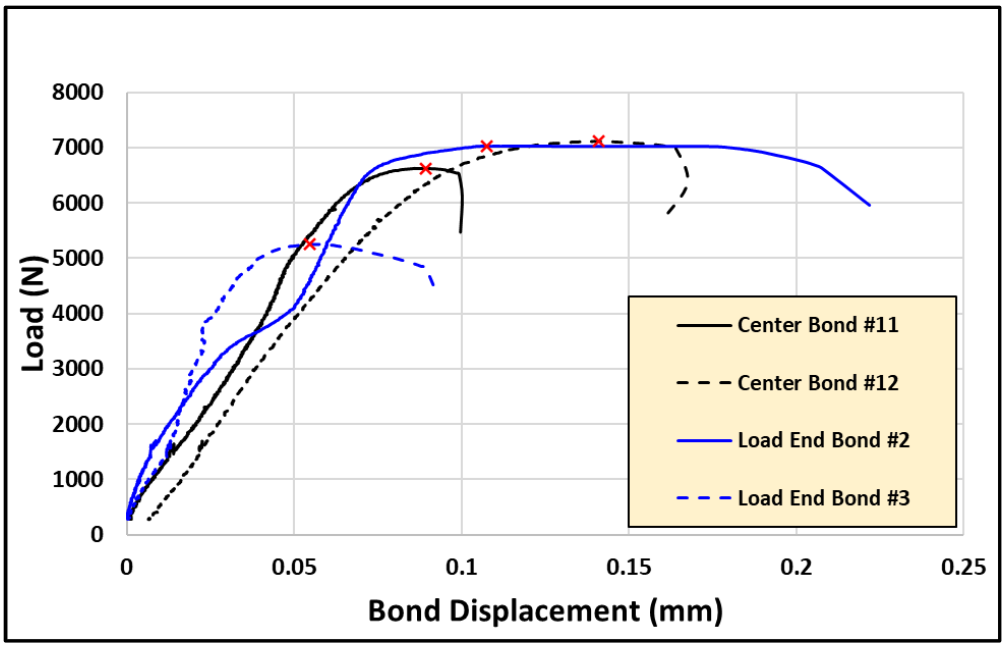

Figure 29. Failure load test cycle versus displacement.

Coupon #11 is used to review the results and electromechanical impedance in detail. All coupon failure modes are similar to coupon #11 (primarily cohesive bond failure). The sensor embedded in the center of the lap shear bond achieved the highest load (sensor #12). One of the sensors embedded at the load end of the bond achieved the lowest test load (sensor #3). Table 5 provides the peak load achieved.

Table 5. Peak load achieved for each sensor coupon test.

Sensor	Bond Location	Peak Load (N)	Stress (MPa)
2	Load end	7033	10.9
3	Load end	5257	8.1
11	Center	6630	10.3
12	Center	7120	11.0
Average		6510	10.1

Embedded Sensor Coupon Impedance Tensile Test Results

For each sensor coupon, the electromechanical impedance is measured in the unloaded condition between the load increments, repeating up to failure. As an example, Figure 30 shows

the real and imaginary values of the impedance for each load level on the sensor #11 coupon. Note that the various colored curves represent each sequential load increment.

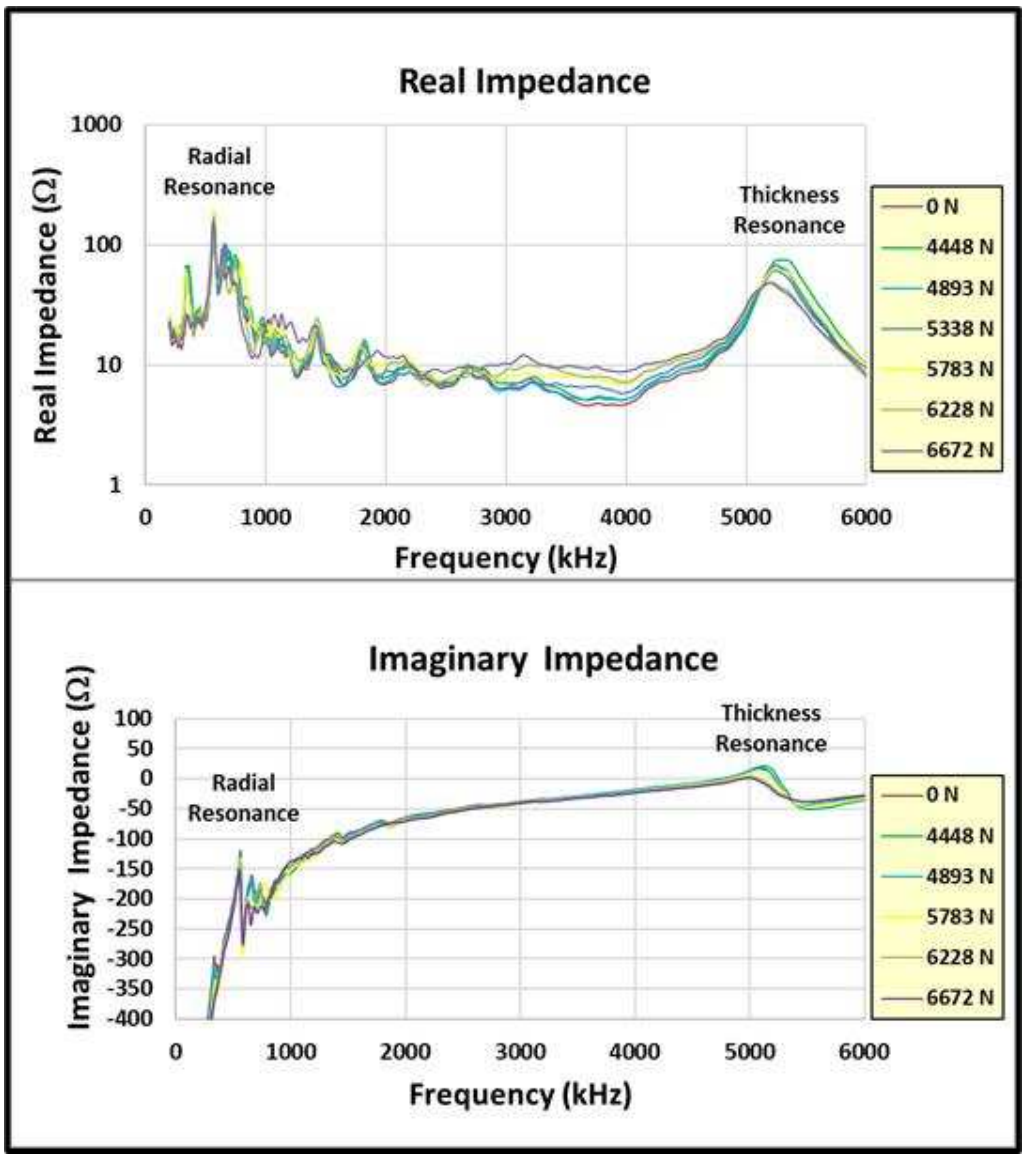

Figure 30. Sensor #11 impedance for each load increment.

Discussion

The discussion that follows is broken down into three subsections related to the sensor itself, the effects of mechanical testing on the embedded sensor specimens, and the effects of sequential loading as a way to review the results and assemble critical outcomes.

Baseline Sensor Impedance Testing

The free state impedance response was first compared to the simulation results, shown in Figure 31. Sensor #11 impedance results are chosen for the comparison. The analytical representation correlates well with the experimental results for the real part of the impedance. This indicates that the simulation captured the structural resonance of the sensor. The small difference in the primary radial resonance is most likely due to the effect of the wires suspending the sensor. This is amplified in the higher order harmonics. This is not a concern, since embedding the sensor constrains the response and removes any contribution of the higher order resonant responses. The primary thickness impedance showed good correlation to the test results. It is interesting to note that the imaginary impedance showed a much higher amplitude at the radial resonance than the simulation. This is due to the free state of the sensor in the experiment and indicates that the sensor was not bonded, which matches the free boundary state of the test. As a result of the acceptable correlation, the ANSYS analytical model can be used directly in possible 3D representations of the joint for embedded sensor impedance simulation studies.

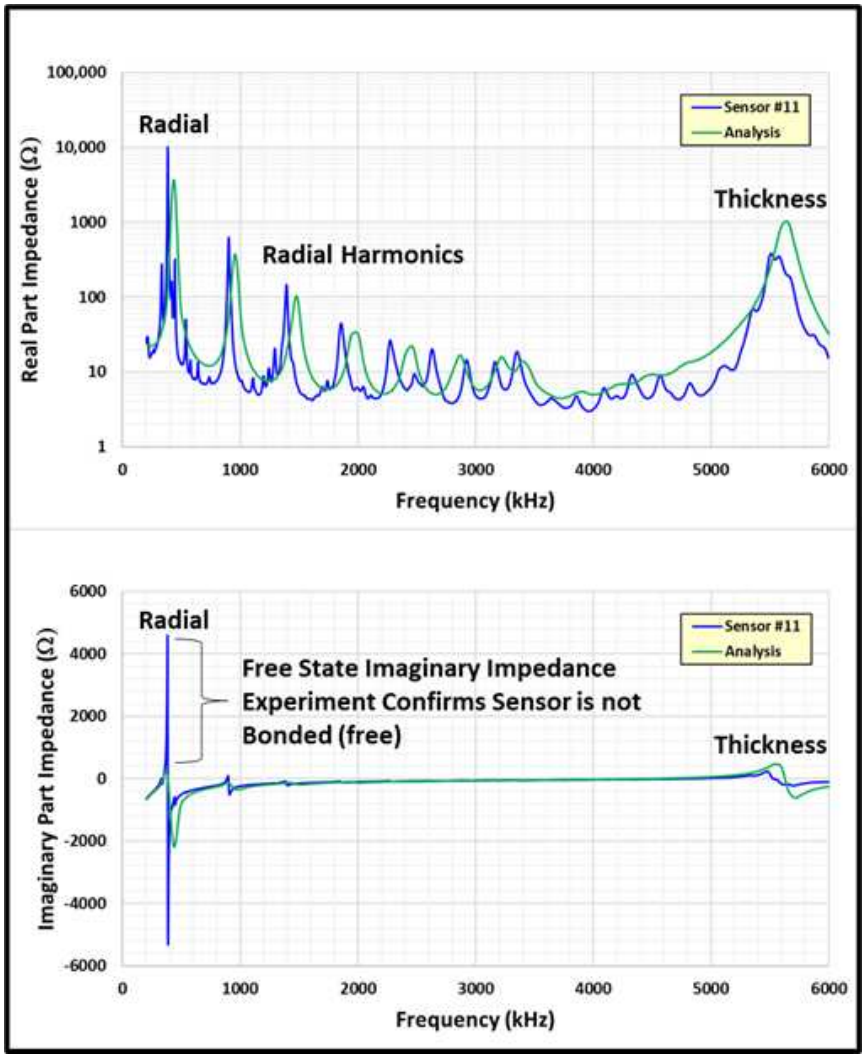

Figure 31. Free sensor impedance, sensor #11 versus analysis.

Figure 32 shows the comparison of the baseline impedance tests, both of the sensor in the free state and the embedded joint state before test loading. Sensors 2, 3, 11, and 12 are shown since they are coupon-embedded operable sensors. The free state response shows a dominant first radial mode, followed by its higher order harmonic resonances. The thickness mode exhibited a clear response at approximately 5500 kHz with lower amplitude and higher damping than the primary radial mode. The embedded sensor coupon showed a much lower amplitude and higher damping for both the radial and thickness modes. This is the physical effect of constraining the sensor within the adhesive bond of the test coupon. The sensor is not allowed to move and exhibits higher damping.

Note that the radial harmonic modes are no longer distinct enough to readily separate in the embedded sensor response, as shown in Figure 32 (b). The resonance responses of the four sensors are averaged and plotted for free versus embedded sensor impedance comparison in Figure 33. The primary radial response increased from an average of 384 kHz to 656 kHz with much lower amplitude and higher damping. The increase in resonant frequency and damping is due to constraining the sensor within the bondline of the coupon, resulting in higher pointwise structural stiffness. The thickness mode response also showed a decreased amplitude with higher damping (broader peak). The thickness resonance decreased in frequency from an average of 5600 kHz to 5200 kHz.

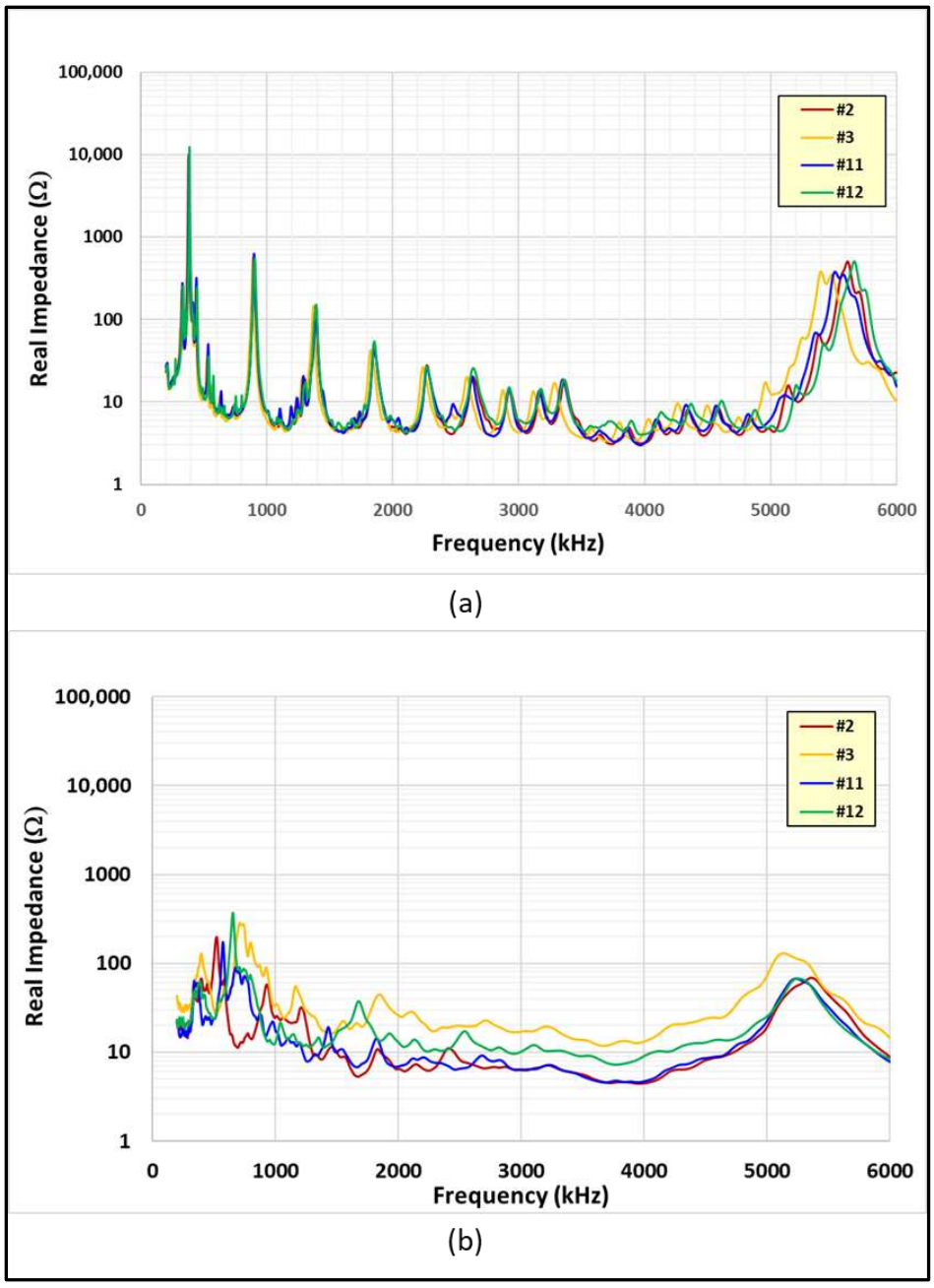

Figure 32. (a) Free sensor, (b) embedded sensor, baseline impedance results.

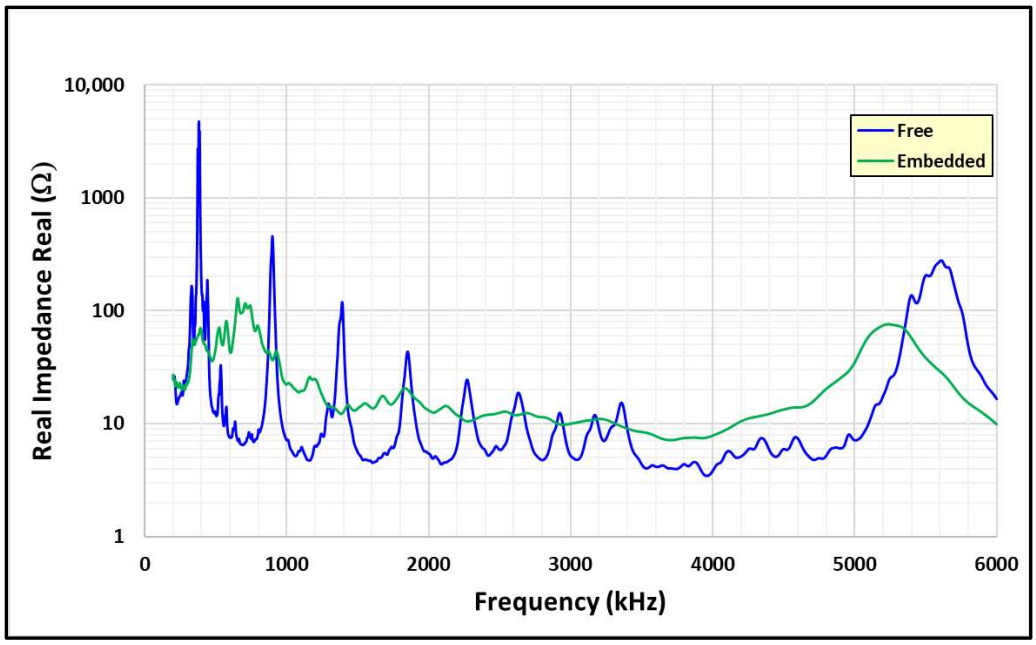

Figure 33. Free versus embedded sensor average impedance.

Embedded Sensor Effect on Tensile Load Performance

The lap shear coupon failure loads are summarized in Table 6 and compared to the baseline (without sensor) coupon test results. The load versus displacement for the final load increment (before the failure load test) comparing the three configurations is plotted on Figure 34. Sensor #11 (center bond) and Sensor #3 (load end bond) are plotted with pristine coupon 2 along with the maximum load achieved, designated with an 'x'. Some clip gage slipping is noted in the sensor #3 trace above 2000 N and in the sensor #11 trace above 4000 N. The slopes (stiffnesses) are similar, measured prior to clip gage slipping, for the three configurations, with the embedded sensor coupons failing at lower loads.

Table 6. Average tensile failure load.

Configuration	Failure Load (N)	% Difference
Pristine	10280	--
Sensor center	6875	−33
Sensor load end	6145	−40

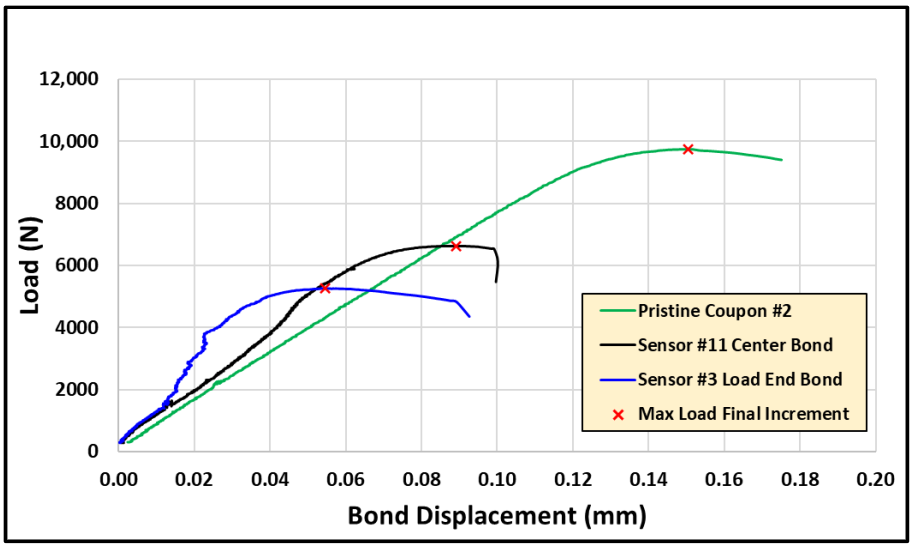

Figure 34. Load versus displacement of pristine and sensor coupons.

The failure loads in Table 6 indicate a much lower result when the sensor is embedded in the coupon bondline. The % difference for the sensor located in the center of the bond is −33% and −40% when the sensor is located at the end of the bond. To understand these results, the coupon thicknesses are measured both for the pristine and embedded sensor coupons. The bondline thickness of the pristine coupons measured an average of 0.25 mm, and the sensor coupons were 0.62 mm. The reason for the thicker bondlines of the sensor coupons is due to the sensor and wire thickness values. The sensors measured 0.39 mm thick, which is double the APC specified value (0.20 mm) for this piezoelectric sensor. This was not anticipated and is due to the effect of soldering the wires to the upper and lower surfaces of the sensor. Furthermore, the wires (which are embedded in the bond) had a diameter measured at 0.50 mm each. Together, these items led to a bondline thickness of 0.62 mm, which is measured consistently for both sensor locations. Unfortunately, this thicker bondline (over twice the thickness of the pristine coupons), resulted in adhesive-poor, porous, void-rich bonds for all the sensor coupons. The result of this adhesive-poor bondline is a knockdown of 33–40% on the tensile load performance compared to the pristine specimens. The test data are consistent and represent a bondline that exhibits the effects of these

defects. However, since the embedded sensor coupons are all similar in bondline thickness, meaning all had similar porosity and void content, the failure load results can be compared to determine the effect of sensor location on bond strength. As previously mentioned in the experiments section, a FEM is constructed and analyzed to simulate the lap shear test and evaluate the sensor effect on the stress distribution through the coupon-adhesive bond. It is seen in the experimental results that the coupons with the sensors near the end-points failed at a lower load level than the center bond-located sensors. These results are consistent with the analytical data and indicate that the center of the bond should be selected for the sensor location, based on the structural performance of the lap shear joint.

Embedded Sensor Impedance during Successive Loadings

The radial and thickness resonance results, with increasing load, are plotted in more detail in Figure 35 for the coupon with sensor #11. Each line is an incremental load cycle that is increased until the coupon failed. A large change was noticed in the thickness response on the final incremental load before failure. This was most likely due to a loss in joint stiffness and a gain in damping, which lowered the resonance amplitude. It is interesting to note that both the radial and thickness resonant frequencies increased slightly from the baseline values after the initial loading. The real impedance amplitude also increased. This could be due to initial consolidation of the joint under a light load. After the initial loading, both resonances began to decrease in frequency and amplitude. A major change is seen in both responses during the final load cycle (highest). The response amplitude is greatly reduced, and the damping is significantly increased. It is also interesting to review the imaginary part of the impedance load response in detail for both resonances. This is plotted in Figure 36.

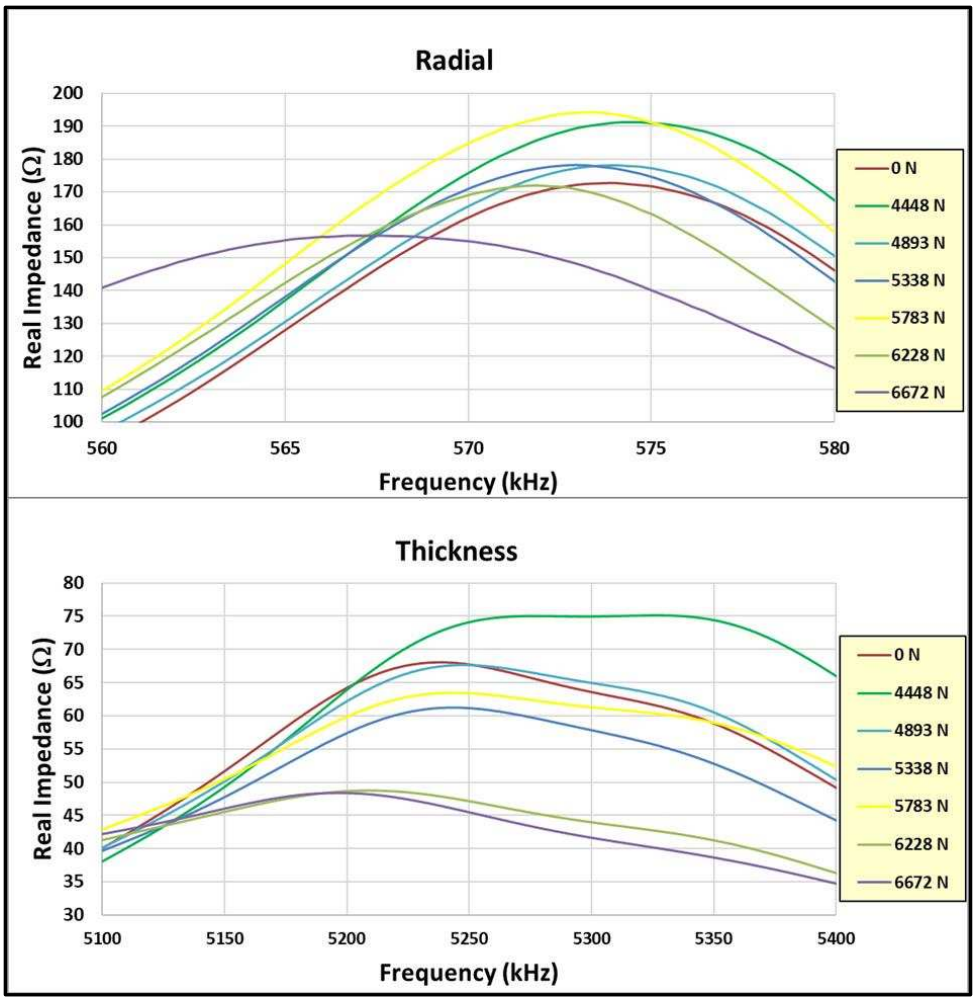

Figure 35. Radial and thickness impedance (real) resonance & load level sensor #11.

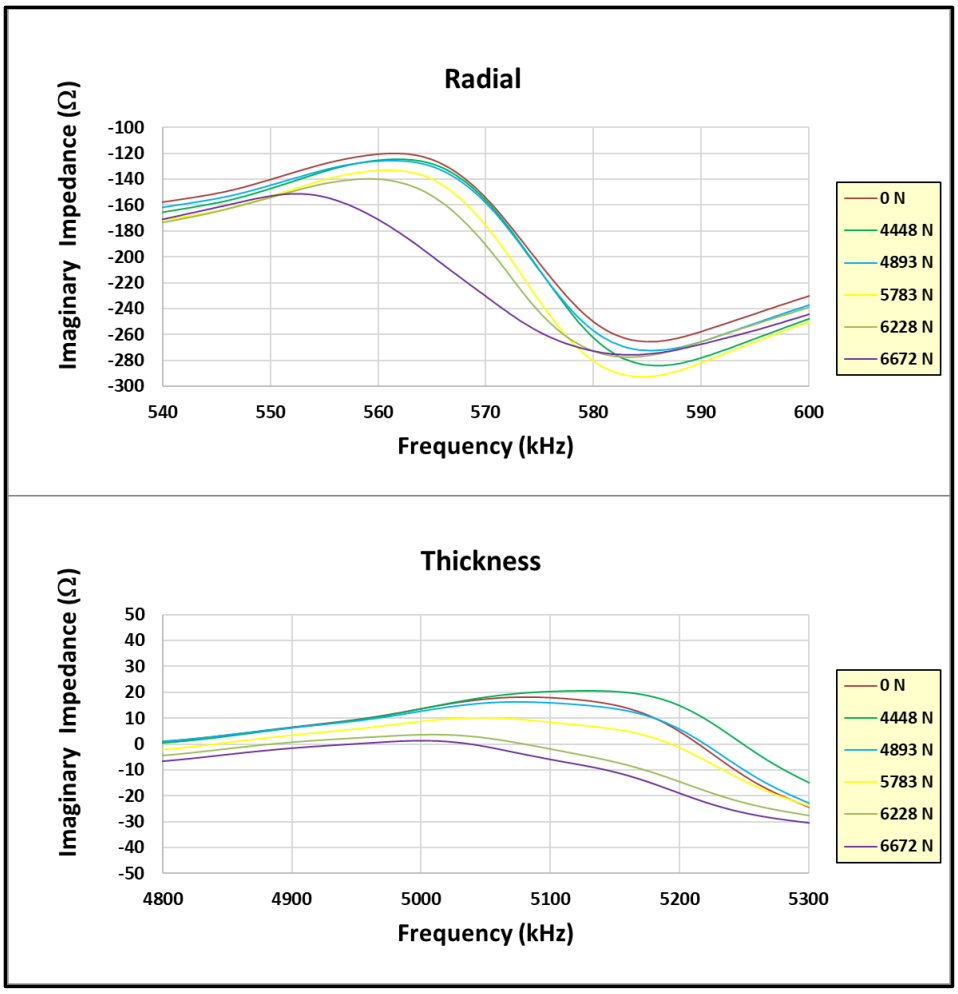

Figure 36. Radial and thickness impedance (imaginary) resonance & load level sensor #11.

Of note, in both Figures 35 and 36, examining the thickness resonance change (both real and imaginary) parts reveals a negative change at a lower load level (6228 N) than is shown in the standard evaluation of the radial resonance change. This corresponds to an earlier warning of joint degradation as the loading level was increased.

Health Monitoring Evaluations Based on Impedance Measurements

Reviewing the current literature produces several methods to evaluate the structural health of the bond via the impedance response of a piezoelectric transducers[14,32-33]. One of the most prominent evaluation tools is the root mean square deviation (RMSD) of the measured real part of

the impedance during successive loadings. The RMSD is used here for the estimate of bond damage. Equation (4) below defines the RMSD, which relates the most recently measured impedance resonant frequency compared to the baseline measured value. For this work, the damage index was calculated for both the primary radial and thickness resonances. Most of the literature focuses on the radial mode evaluation of the change in the real part of the impedance. A damage index value of −2%, calculated on the radial resonance, is the estimated threshold where the bondline integrity begins to approach a degradation level that corresponds to joint failure[14].

$$RMSD = \sqrt{\frac{\sum_{i=1}^{n}\left[Re\left(Z_n(\omega_i)\right) - Re(Z_u(\omega_i))\right]^2}{\sum_{i=1}^{n}[Re(Z_n(\omega_i))]^2}} \qquad (4)$$

where Z_n is the healthy bond impedance and Z_u is the measured bond impedance after the static load is applied and unloaded. Table 7 shows the calculated damage indices for each load level (both radial and thickness resonances) and Figure 37 shows the damage index plot as a function of applied load, again for the embedded sensor #11 test coupon, with the failure load indicated.

Table 7. Load and damage index (DI) for sensor #11.

Load (N)	Radial (kHz)	DI (%)	Thickness (kHz)	DI(%)
0	574	--	5239	--
4448	574	−0.1	5274	0.7
4893	574	0.0	5248	0.2
5338	573	−0.2	5246	0.1
5783	573	−0.1	5242	0.1
6228	572	−0.4	5208	−0.6
6672	567	−1.2	5196	−0.8

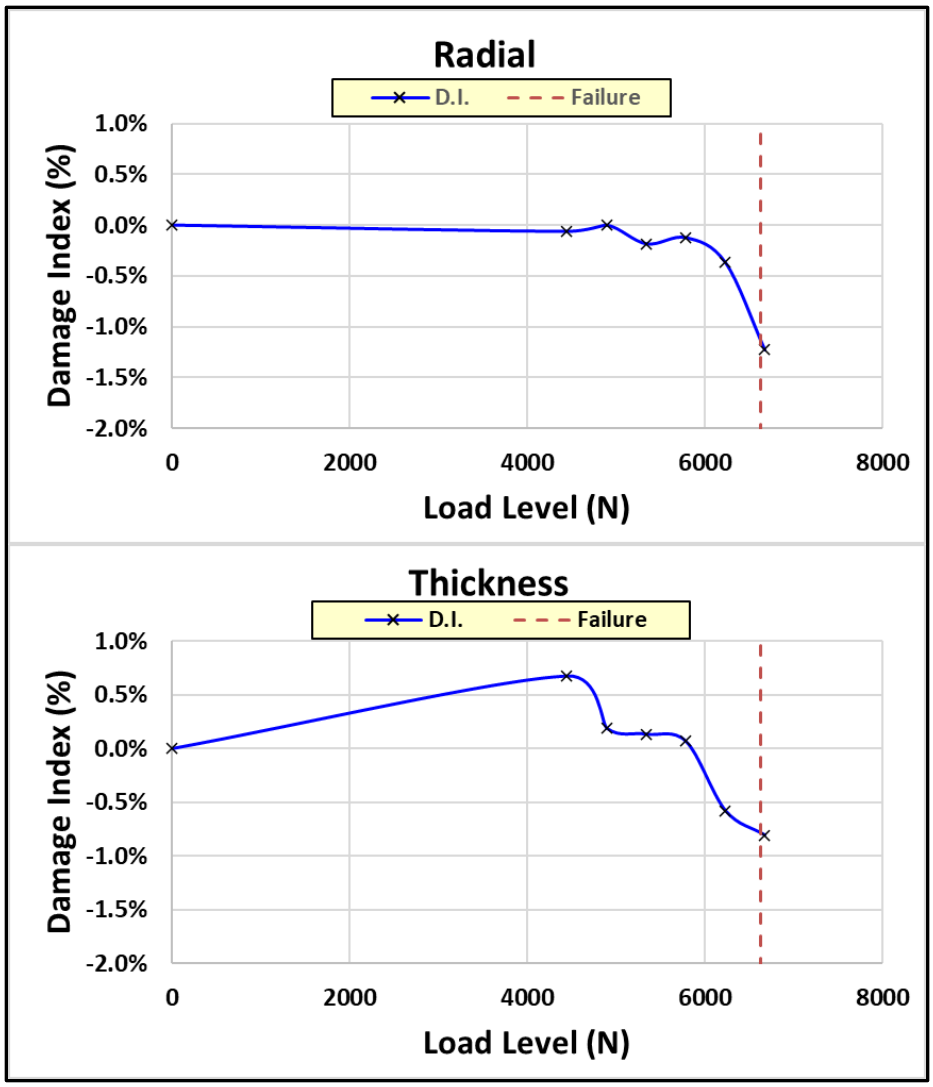

Figure 37. Sensor #11 damage index versus load level.

For further definition, Figure 38 shows each measured impedance resonance (radial and thickness), plotted against load level with the failure load denoted and the −2% damage index identified.

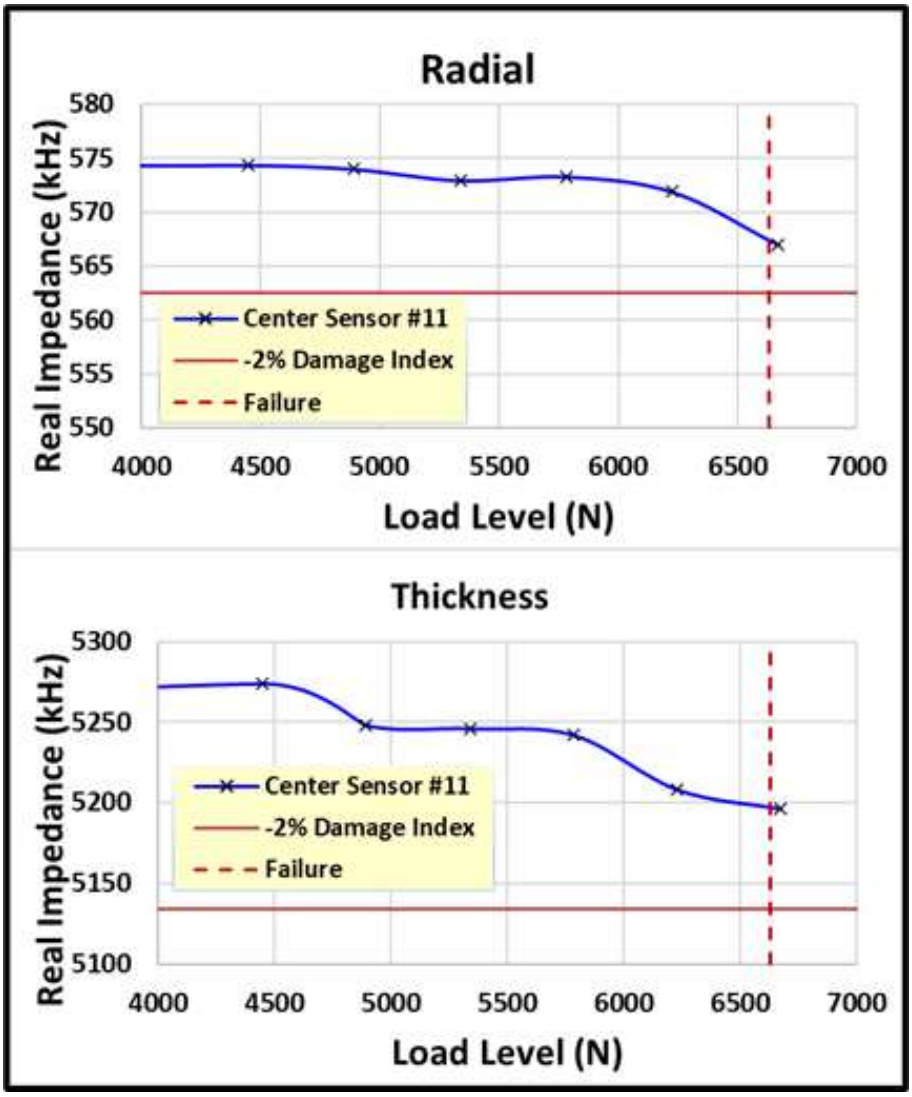

Figure 38. Sensor #11 real impedance versus load level.

Both the radial and thickness impedance damage indices trend toward the −2% RMDS value at the time of failure of coupon #11. Traditionally, the damage index is evaluated only for the radial or in-plane response. For this work, the thickness, or out-of-plane response, is also evaluated with repeated loads. The radial response dropped off quicker than the thickness response and was close to −2% at failure. However, evaluating the thickness impedance damage index shows a larger change at a lower load level than exhibited in the radial damage index load progression. This is illustrated in Figures 37 and 38. From these plots, it is seen that the change in sensor impedance

response can be used to warn of impending joint failure, and that examination of the thickness resonance impedance change can provide an earlier alert to degradation of the joint. Of particular note, on the second-to-last load before failure, 6228 N, a significant change in the damage index is observed for the thickness impedance response suggesting that failure is imminent and structural loading should be reduced to prevent catastrophic failure. The test coupons with the sensors located at the load end of the bond behaved differently than the center bond sensors in terms of the change in impedance resonance or damage index. These coupons exhibited a large damage index after the first load was applied. For both load-end bond sensors, the radial impedance damage indices were greater than the −2% warning level after this loading (4448 N). However, both of these coupons continued to take load and failed at much higher levels than the −2% threshold level. Load-end bond sensor #2 failed at 7033 N and sensor #3 failed at 5257 N. Locating the sensors at the end of the bond in the area of high stress has more effect on the impedance response of the sensor during loading and aids in earlier failure initiation. This adds difficulty to using the damage index to predict joint failure.

Due to the degradation in structural performance with the sensor location at the end of the bond and the difficulty observed with the damage index failure load predictability, it is recommended to use the center of the bond for locating the sensor. This location minimizes the degradation on tensile load shear performance and produces impedance results, during repetitive loadings, which can be used for bond health monitoring. This completes Phase 2 experimentation. Based on evaluation of the experimentation results and the need to complete additional testing to confirm the hypothesis, a second phase of single lap shear joint experimentation and assessment is required. The main goal of Phase 3 experimentation is to assess the embedded sensor joint performance and evaluate additional aspects of the sensor response for improvement in health

monitoring capability. Flatwise tension coupons with embedded sensors are also tested in Phase 3.

Chapter 4 Phase 3 Efforts

From evaluation of the Phase 2 test results, it is required to embark on another phase of testing and analysis. In order to alleviate the porous, void rich coupon bonds, which negatively affect the joint structural performance, another set of lap shear coupons are fabricated with a thicker uniform bond. The response characteristics of the sensor radial and thickness resonances are examined in detail for additional information to aid in a more robust health monitoring capability. The adhesive used to bond these coupons is paste adhesive, as opposed to film adhesive. Paste adhesive uses a room temperature cure and is effectively easier to control the bondline thickness to eliminate the bond imperfections that were experienced in Phase 2. In addition to single lap shear coupon testing, similar coupons are to be loaded in the normal direction (flatwise tension) in order to evaluate the embedded sensor capability when exposed to loads applied in a different axis.

Experimentation / Results

Free Sensor Electromechanical Impedance Response

The piezoelectric sensor disks used in these experiments were ordered from APC International and are solid disks, consisting of a highly purified lead zirconate (PZT) ceramic. These are the same model sensors that were used in the previous set of experiments with the film adhesive bonds. The only difference is in the soldering of the lead wires that connect to the spectrum analyzer. To apply the voltage to the sensor disk, one lead is soldered to one surface (positive) and one lead is soldered to the other surface (negative). In the previous experiments, the leads were soldered at the same location on each surface and run off together from one side of the disk. The leads are thick (0.50 mm) and possibly added to the bondline defect in the last set

of experiments. This time APC was requested to bond them on the opposite side of the surface so that one lead extended off one side and the second lead off the other side. This minimizes the thickness footprint of the leads in the bond reducing the potential performance impact of larger bondline defects.

A total of 15 sensors were obtained from APC international. The electromechanical impedance for all sensors is measured while the sensors are supported in the soft packing material (essentially a free boundary state). The sensor impedance response is fairly consistent across all sensors when comparing the primary radial and thickness resonant frequency and amplitude. Based on the response consistency, 10 of the sensors were selected for bonding and the others were set aside as spares. The free sensor impedance response is shown in Table 8 and the frequency response plot is shown in Figure 39.

Table 8. Free sensor measured impedance resonances.

Sensor	**Radial (kHz)**	**Amplitude (kOhms)**	**Thickness (kHz)**	**Amplitude (kOhms)**
1	386.0	8.9	5625.2	0.53
2	387.2	7.6	5591.6	0.49
3	390.8	8.4	5649.2	0.49
6	386.0	8.9	5614.4	0.49
7	390.8	7.5	5645.6	0.51
8	387.2	7.9	5630.0	0.58
9	386.0	8.5	5614.4	0.42
13	386.0	8.4	5588.0	0.50
14	383.6	7.8	5566.4	0.46
15	392.0	8.1	5636.0	0.45
Average	387.6	8.2	5616.1	0.49

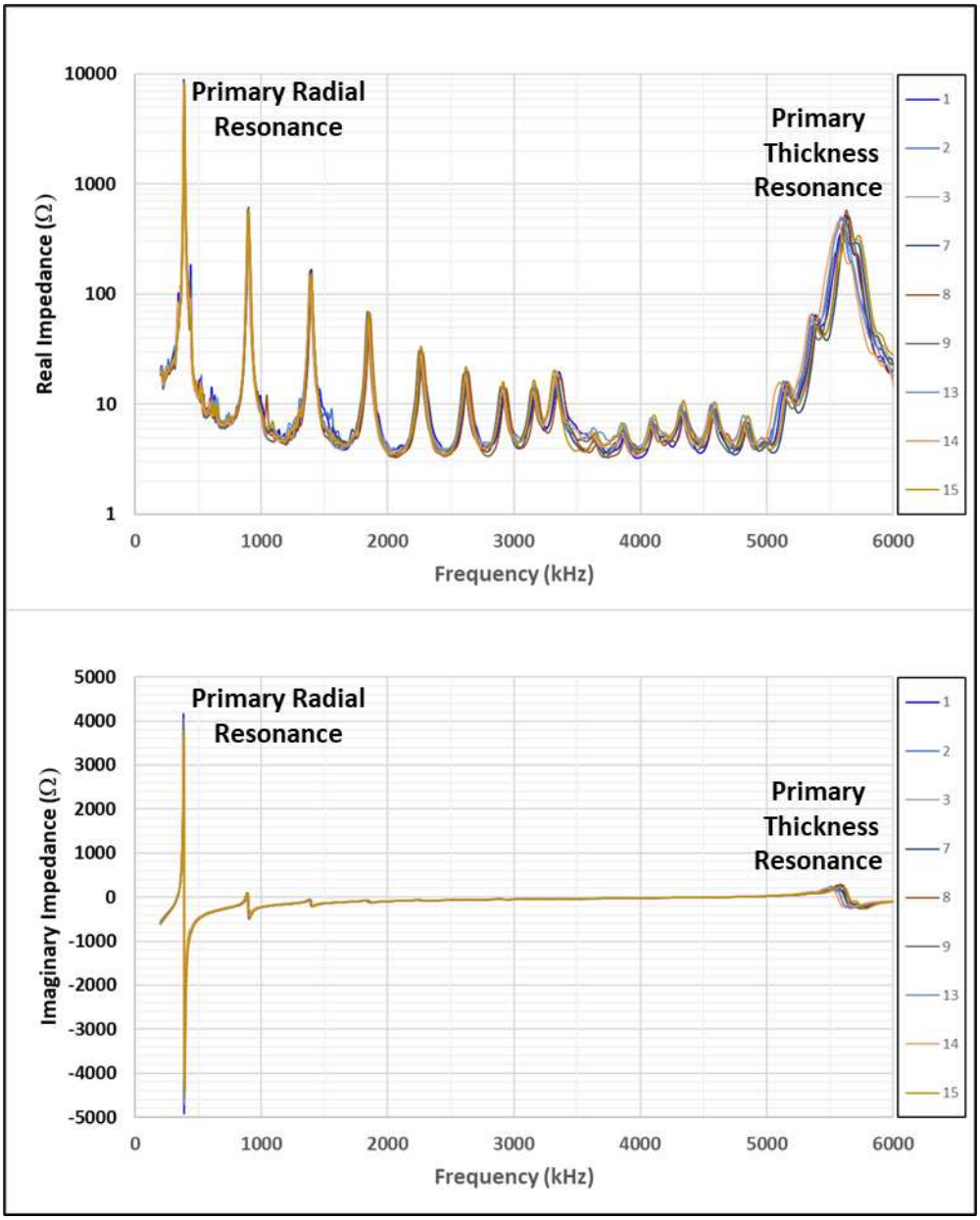

Figure 39. Free sensor impedance response.

Test Coupon Fabrication

Single lap shear and flatwise tension coupons are fabricated from composite adherends that consist of 12 plies of T650-35/5320-1 carbon/epoxy 8HS woven fabric prepreg in a quasi-isotropic layup $((45/0)_3)_S$. The adherends used the Solvay CYCOM 5320-1 toughened epoxy resin system and were vacuum bag cured at 177°C to form a panel. The panel is then cut into test coupon

adherends with a diamond saw. The test adherends are bonded together using LOCTITE EA 9394 AERO epoxy paste adhesive[34]. EA 9394 is a two-part structural paste adhesive which cures at room temperature and does not require vacuum bagging. The room temperature cure takes 3-5 days at 25°C to achieve nominal mechanical performance. It is acceptable to accelerate the cure by placing the coupons in an oven at 66°C for 1 hour. A total of 12 single lap shear test coupons were fabricated (8 pristine and 4 with bondline embedded sensors). The sensors were located in the center of the shear bond with the lead wires running out of the coupon perpendicular to the load axis. This was done to minimize any degradation effect on the structural performance by locating the sensor/wires in the area of minimum shear stress. The single lap shear adherends were placed into a 3D printed bond fixture for curing. The bond fixture was designed to maintain the coupon geometry and control the bondline thickness. The target bondline thickness is 0.71 mm, which is predicted to give similar bondline thickness for pristine and embedded sensor coupons. Figure 40 shows the single lap shear adherends fit into the 3D bond fixture.

Figure 40. Single lap shear adherends fit into bond fixture.

The flatwise tension coupon adherends (25.4 mm by 25.4 mm) are placed into an aluminum bond fixture as show in Figure 41.

Figure 41. Flatwise tension coupon bond fixture.

The two-part structural paste adhesive is mixed together and applied to the prepped bond surfaces and fit into the bond fixture. The coupons are then placed in the oven for an accelerated cure at 66°C for 1 hour as shown in Figure 42. There are 4 lap shear bond fixtures, therefore 3 cures are required to fabricate 12 test coupons. Weights are placed on the coupons to ensure consolidation of the adhesive.

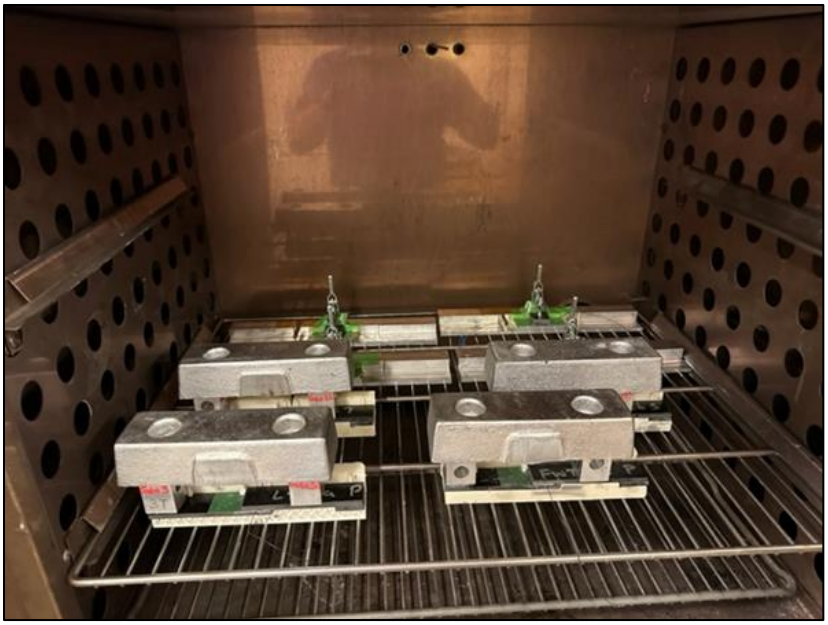

Figure 42. Coupons placed in the oven for the accelerated cure.

The cured test coupons are shown in Figure 43. The sensor lead wires can be seen coming out of the bonded coupons with embedded sensors (positive – red and negative – black).

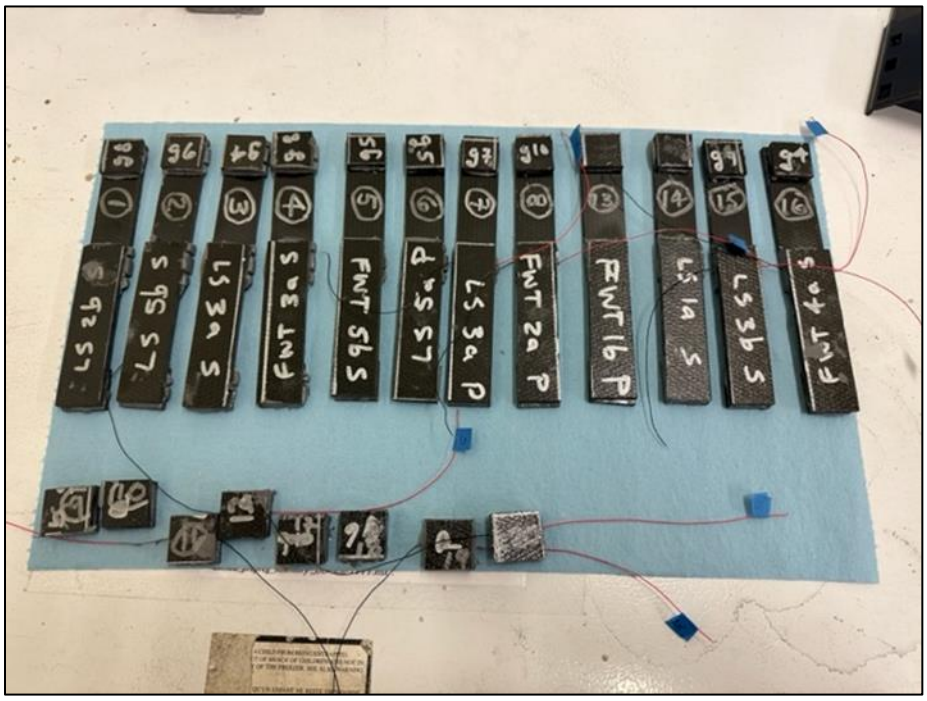

Figure 43. Cured test coupons.

The bondline thickness for the 3 batches of lap shear coupons is measured and evaluated for consistency and proximity to the target of 0.71 mm. The first batch of coupons cured are all pristine (no sensor) with an average bondline thickness of 0.74 mm, which is close to the target. For batches 2 and 3, the average bondline thickness is 0.58 mm pristine and 0.69 mm with the embedded sensor. The flatwise tension coupons (25.4 mm x 25.4 mm) exhibited a large variation between the pristine and the embedded sensor bondline thickness (0.46 mm vs 0.74 mm). This is most likely due to the bond fixture applying the holding pressure to the center of the coupon where the embedded sensor is located in the bondline, allowing the coupon to rotate during cure. For the pristine coupons, the applied pressure allows the adhesive to squeeze out, but with the sensor coupon, the location of the sensor stopped the pressure from squeezing out the adhesive, thus creating thicker bondlines. The flatwise tension coupons need to be bonded to aluminum blocks to allow loading in the test fixture.

Pristine Single Lap Shear Coupon Experiments

The pristine single lap shear coupons are tested mechanically in the ATS 900 universal test machine shown in Figure 44 using the ASTM D5868 FRP single lap shear test procedure.

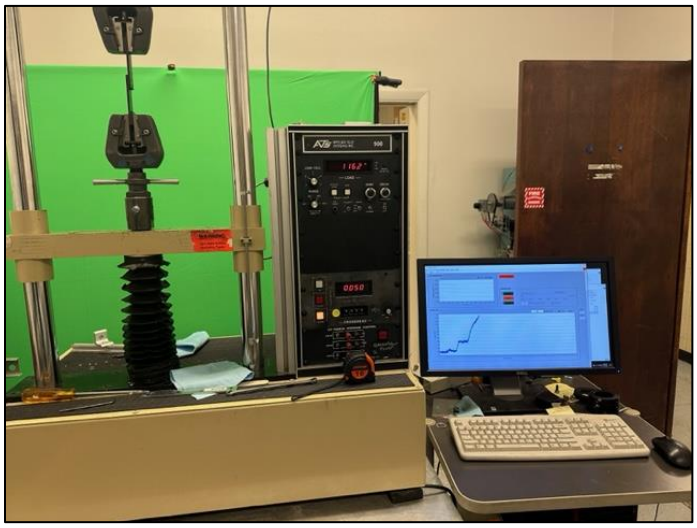

Figure 44. Pristine lap shear coupon loaded in the test machine.

There are a total of 8 pristine lap shear coupons tested, 4 from the batch 1 adhesive, 2 from the batch 2 adhesive, and 2 from batch 3 adhesive. Table 9 shows the test failure load for each pristine coupon. The average failure load for the batch 1 coupons is 10806 N, batch 2 is 4613 N, and batch 3 is 7543 N. The failed pristine coupons are shown in Figure 43. Note that each adherend is oriented so both sides of the failure surface may be observed. The batch 1 coupons exhibit higher failure loads and indicate fiber tears in the adherend, corresponding to bonds with good structural integrity. Batch 2 and 3 coupons failed at considerably lower loads than the batch 1 coupons. This is attributed to inadequate curing of the paste adhesive, which most likely occurred due to incomplete mixing of the two parts before bonding. In Figure 45, the batch 2 and 3 failures appear to be a mixture of adhesive, cohesive, and a combination of both modes. The failed coupon adhesive has a rubbery feel which lends credence to an incomplete adhesive cure.

Table 9. Pristine lap shear coupon failure loads.

Pristine Coupon	**Failure Load (N)**
Batch 1 - 1	10984
Batch 1 - 2	11371
Batch 1 - 3	9733
Batch 1 - 4	11137
Batch 2 - 5	1423
Batch 2 - 6	7804
Batch 3 - 13	6213
Batch 3 - 14	8874

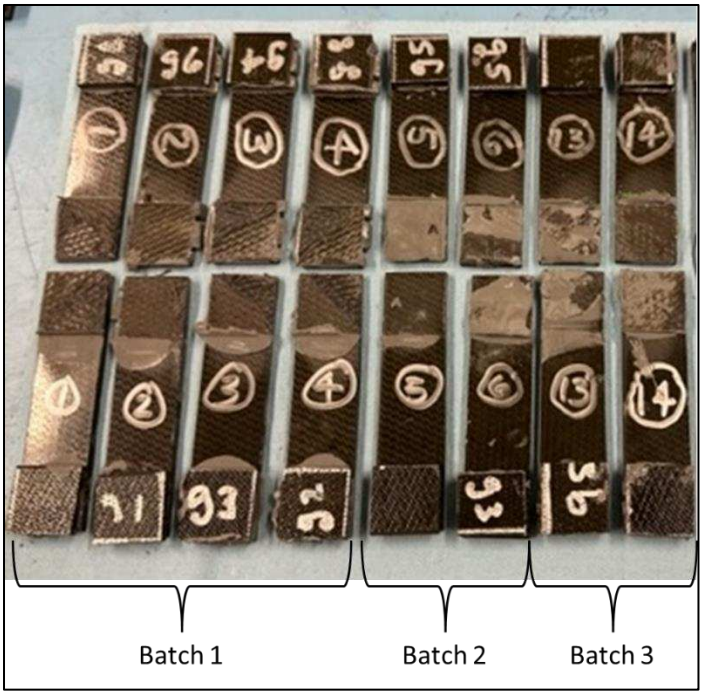

Figure 45. Failed pristine lap shear coupons.

Embedded Sensor Single Lap Shear Coupon Experiments

There are four coupons with embedded sensors fabricated, 2 in the batch 2 cure and 2 in the batch 3 cure. The coupons are tensile tested incrementally until failure and between loads the electromechanical impedance is tested and recorded. Table 10 shows the embedded sensor test coupon failure loads. Coupon #7 exhibited a low failure load, indicating a structurally weak bond similar to pristine coupon #5. Figure 46 shows the embedded sensor failed coupons. The failure appears to be purely a cohesive failure, supporting an inadequate adhesive mix and cure. The rest of the embedded sensor coupons exhibit higher failure loads, fairly consistently.

Table 10. Embedded sensor coupon failure loads.

Embedded Sensor Coupon	Failure Load (N)
#7	3132
#8	7976
#15	7166
#16	7922

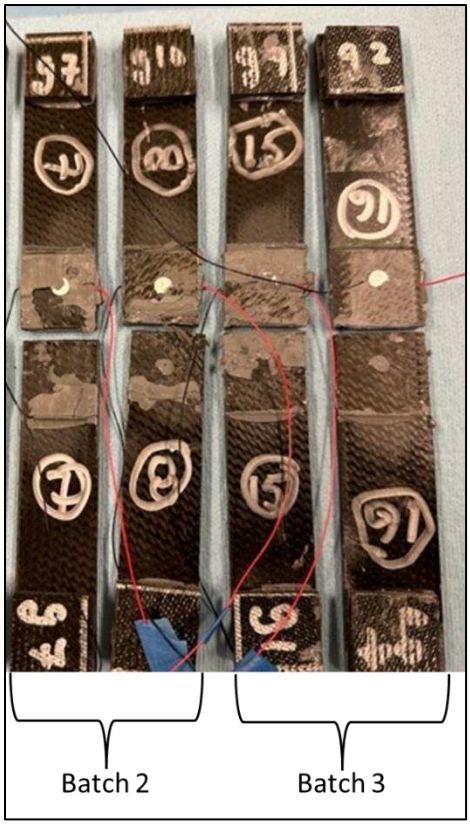

Figure 46. Failed embedded sensor lap shear coupons.

Embedded Sensor Electromechanical Impedance Tests

The embedded sensor coupons are each installed in the test fixture and the baseline embedded sensor impedance is measured. They are loaded initially to 2222 N, unloaded and the impedance is measured with the coupon installed in the test fixture. The load is increased incrementally by 445 N, unloaded, impedance measured, and repeated until failure. Figure 47 shows one of the coupons installed in the test fixture with the sensor lead wires connected to the analyzer and laptop.

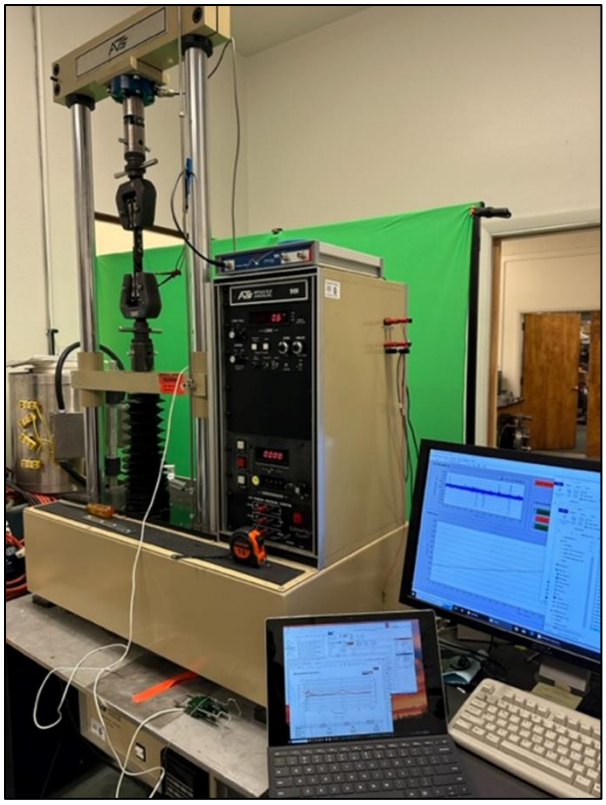

Figure 47. Fixture installed embedded sensor coupon connected to analyzer.

Normally, the electromechanical impedance primary radial resonance increases due to the constraint of the sensor in the lap shear joint (as opposed to a free state). In previous test experience, this resonance is > 400kHz. There is a much lower primary resonance measured in these experiments. This is shown in Figure 48 for coupon 8. The other embedded sensor coupons exhibit similar results.

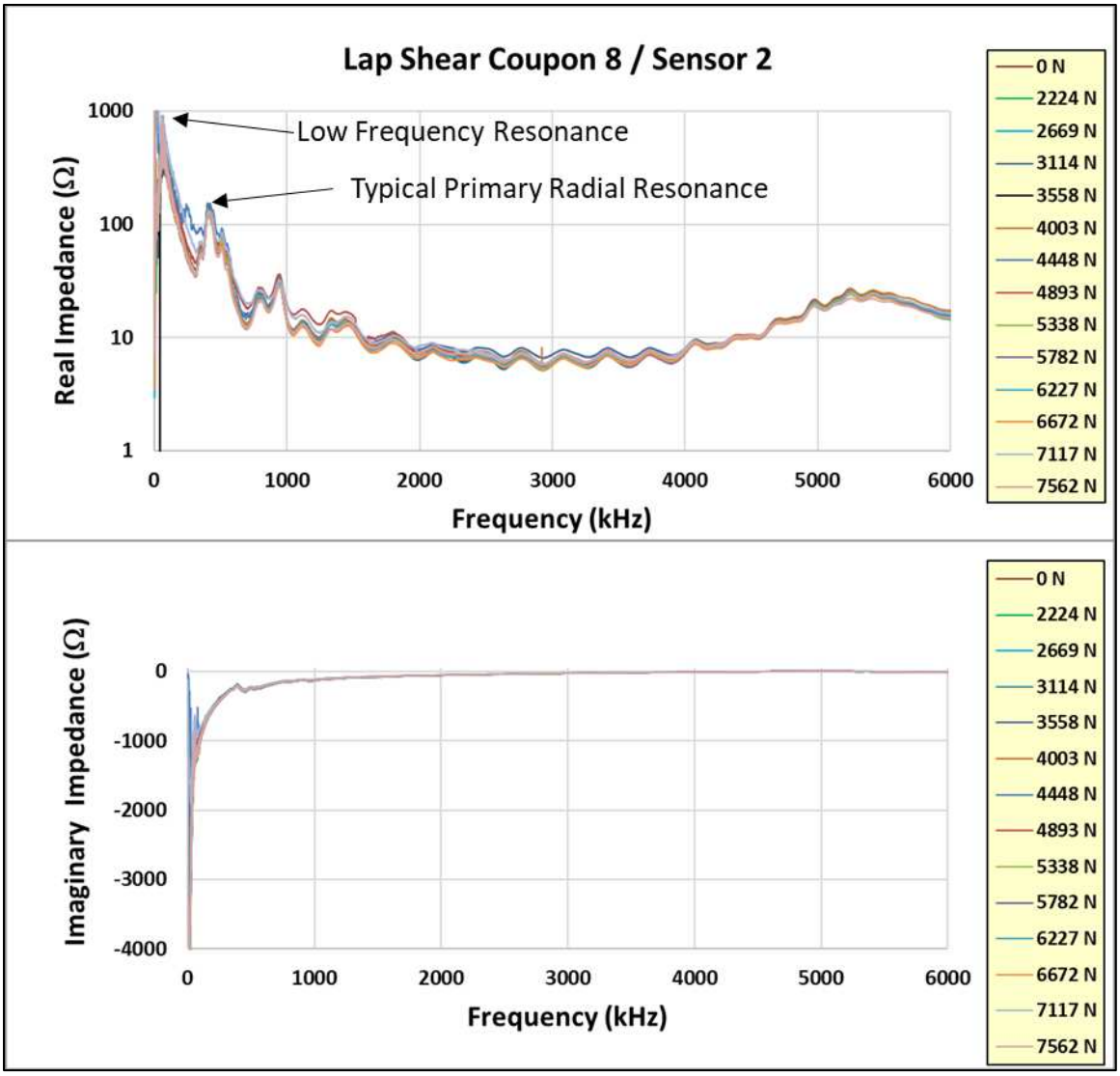

Figure 48. Coupon 8 electromechanical impedance response.

It is noted in Figure 48, there is a lower frequency response that dominates the response and overshadows the normal 400 kHz resonance. Figure 49 shows a closer look at this response from 0 to 1000 kHz. Figure 50 shows an even closer look at the real part of the impedance response up to 100 kHz. The response is concentrated around 60 kHz and contains a high frequency large amplitude oscillation. This phenomena is attributed to interference from the test fixture and was not noticed until post test data review. Unfortunately, the presence of this phenomena negatively affected the ability of the embedded sensor to monitor the structural health of the lap shear bond.

The typical damage index calculation was not meaningful and did not predict the failure of the tested coupons. Due to this, it was decided to fabricate more coupons and repeat the tests.

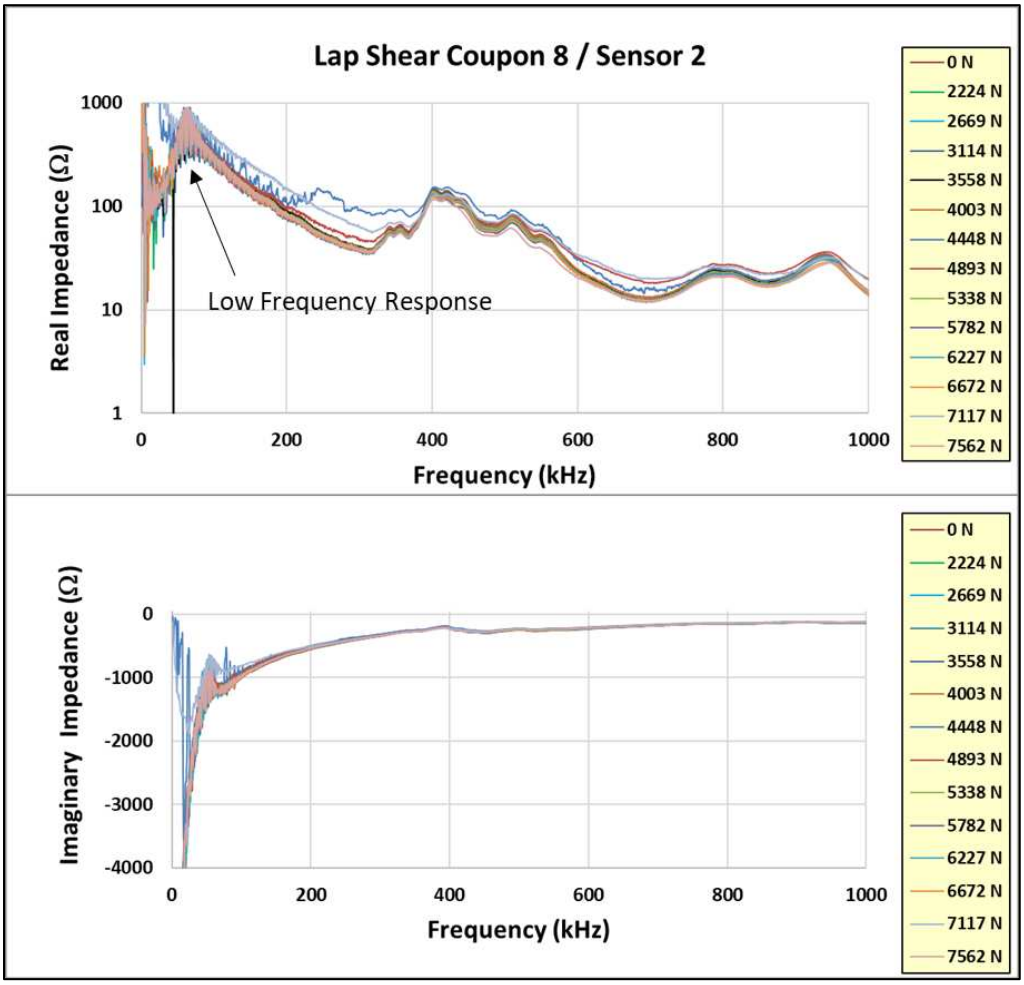

Figure 49. Low frequency impedance response.

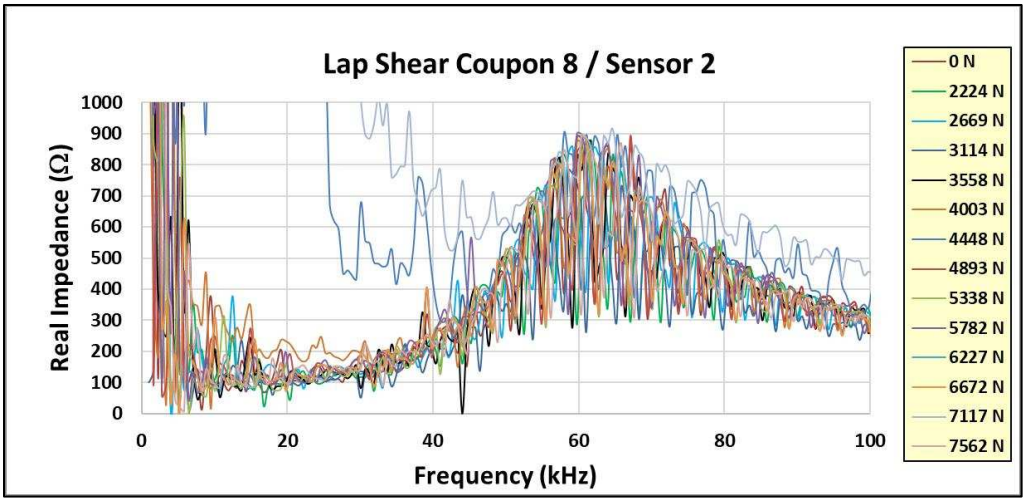

Figure 50. Closeup of low frequency response.

Second Set of Lap Shear Coupon Fabrication

Based on the results of the initial experiments, it was decided to fabricate a second set of lap shear coupons and repeat the tests. Three pristine coupons and three with embedded sensors are fabricated using the 3D printed bond fixtures and EA 9394 paste adhesive. Figure 51 shows the completed test coupons.

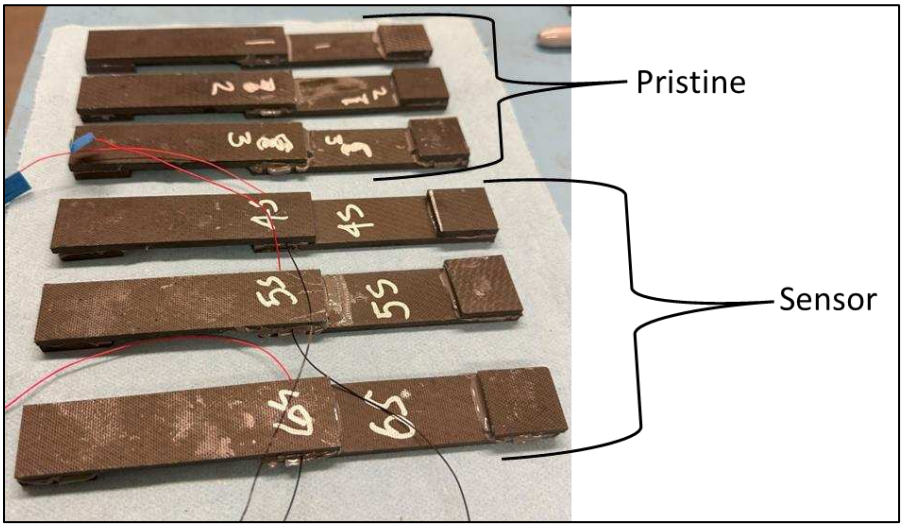

Figure 51. Second set of fabricated coupons.

The sensors are all located at the center of the lap shear bond, similar to the previous coupons and the lead wires exited the bond area at the lowest shear stress (perpendicular to the load direction).

The average bondline thickness for the pristine coupons is 0.74 mm and 0.83 mm for the embedded sensor coupons. The bondline thickness between the pristine and sensor coupons is closer than the previous set of experiments (batch 2 and batch 3 cures). Noting only a 6% bondline thickness increase with the addition of the sensor as compared to a 17% thickness increase in the prior experiments.

Second Set of Single Lap Shear Coupon Experiments

The pristine coupons are each inserted into the test machine and loaded until failure. Figure 52 shows coupon #1 loaded in the test machine.

Figure 52. Coupon 1 loaded in the test machine.

The average failure load for the pristine coupons is 8201 N. The embedded sensor coupons are tested incrementally, similar to the first set of experiments, until failure. The average failure load for the embedded sensor coupons is 8289 N. Note that the electromechanical impedance is

measured between the incremental load applications while the coupon is in the unloaded state. Table 11 shows the failure load for each coupon test.

Table 11. Failure loads – second experiments.

Coupon	Failure Load (N)
1 - Pristine	8326
2 - Pristine	8496
3 - Pristine	7781
4 - Sensor	8093
5 - Sensor	8221
6 - Sensor	8554

The failure loads between the pristine and embedded sensor coupons are much closer than the loads in the first set of paste bond experiments, with only a 1% difference in the average failure load. Figure 53 shows the failed pristine coupons, which all look similar, exhibiting a mixed mode failure (adhesion/cohesion/fiber tear).

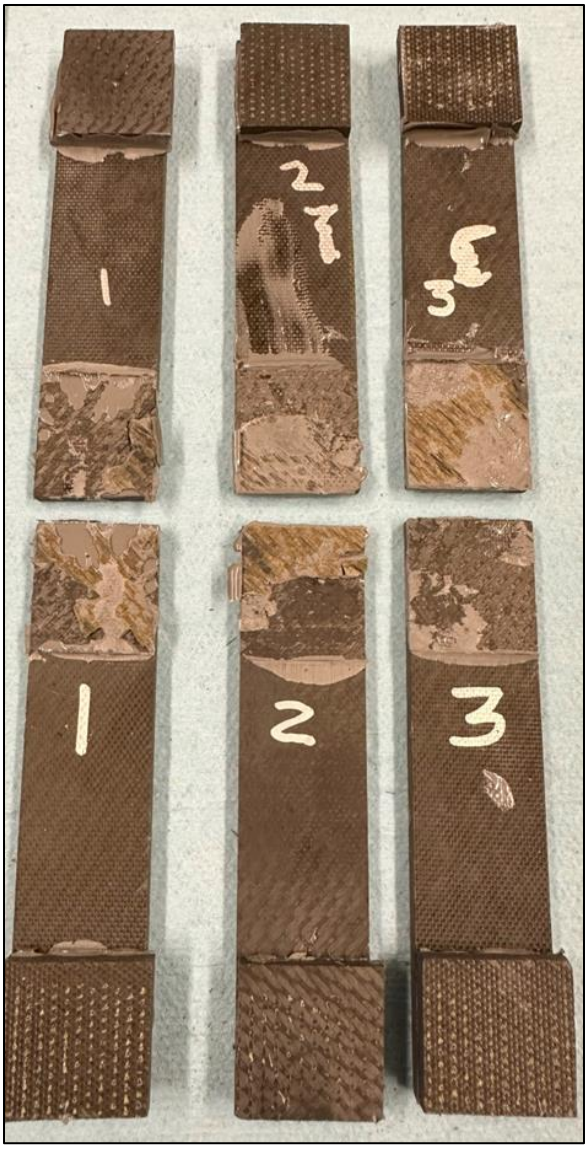

Figure 53. Failed pristine coupon adherends.

Figure 54 shows the failed embedded sensor coupons, which exhibit failures similar to the pristine coupons. Note the failure surfaces include a degree of composite adherend failure which is normally considered to be a “good” structural bond.

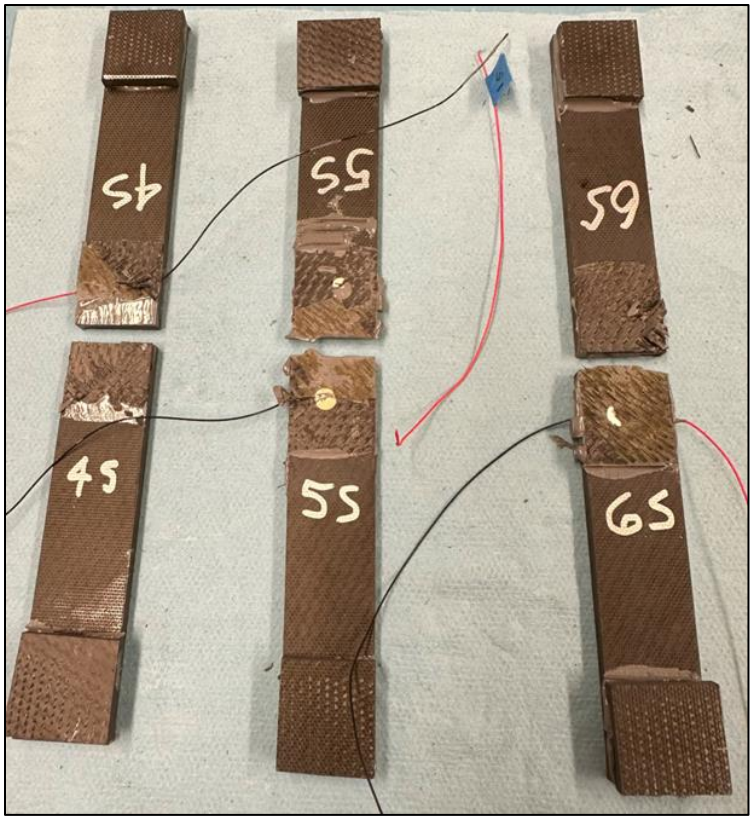

Figure 54. Failed sensor coupon adherends.

Second Set of Single Lap Shear Coupon Impedance Measurements

The second set of embedded sensor coupons are impedance tested. Figures 55-57 show the incremental impedance measurements (real and imaginary) for each of the three series of embedded sensor coupon tests.

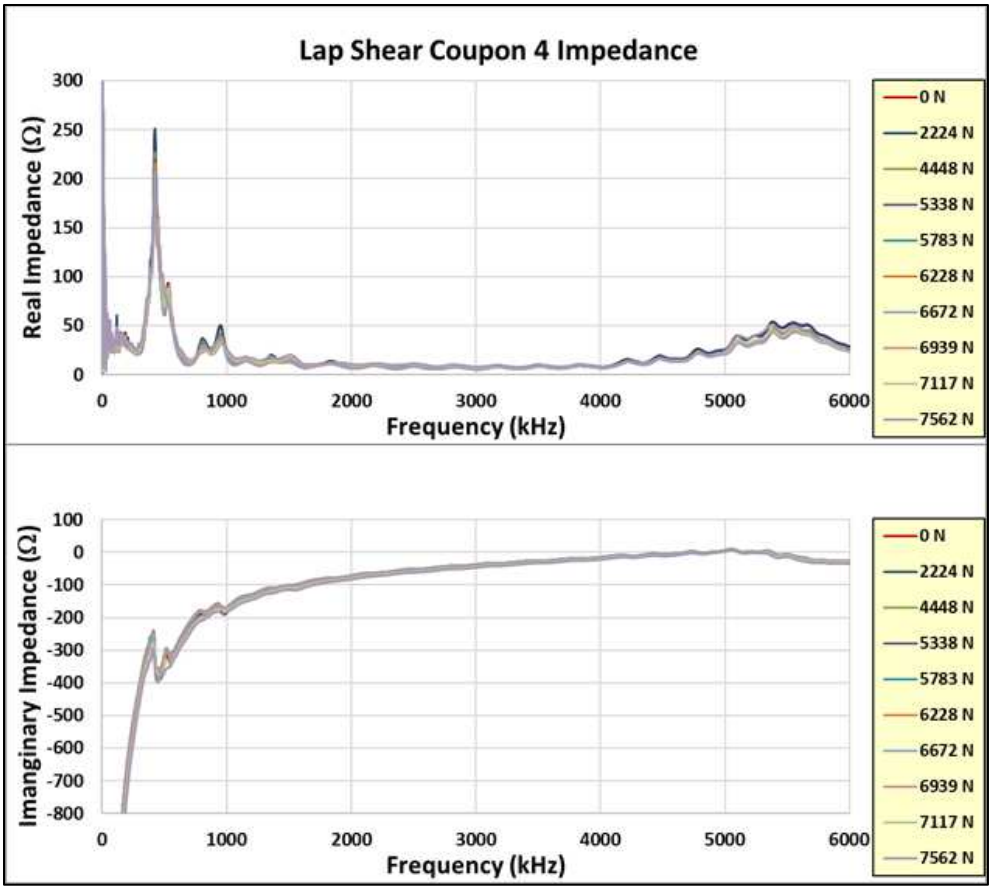

Figure 55. Coupon #4 sensor impedance/load results.

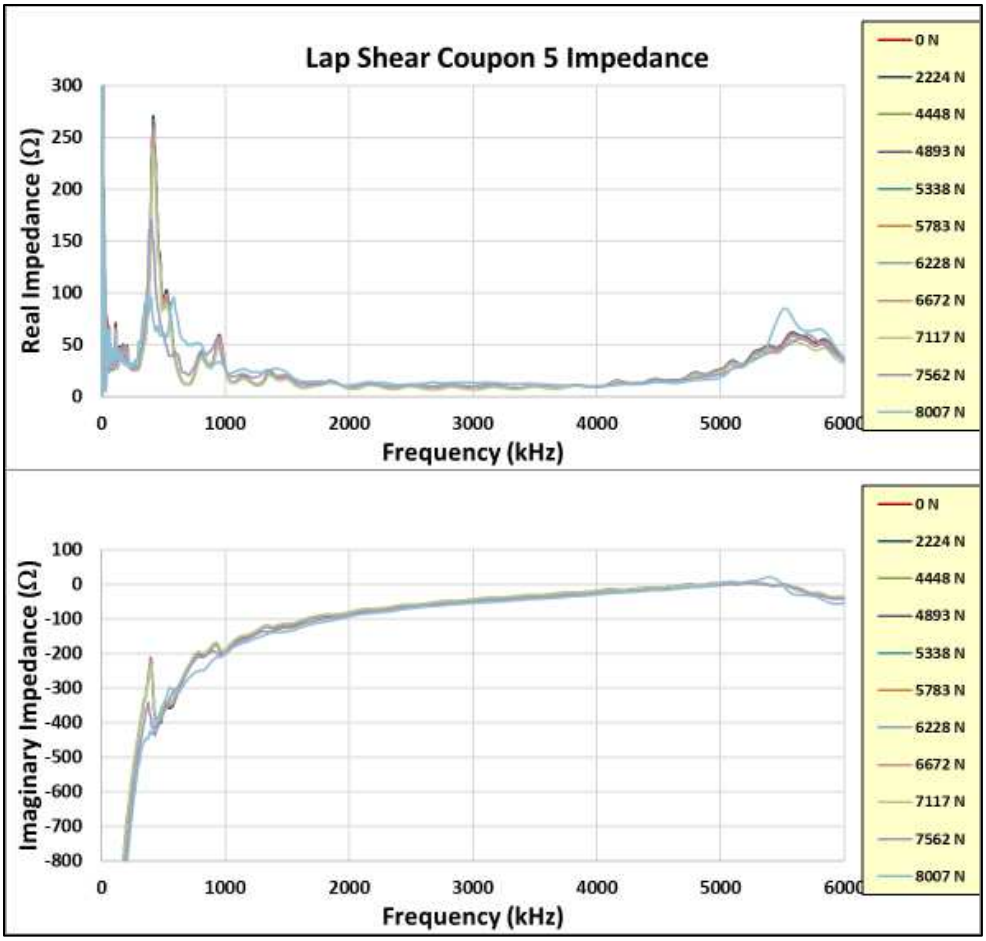

Figure 56. Coupon #5 sensor impedance/load results.

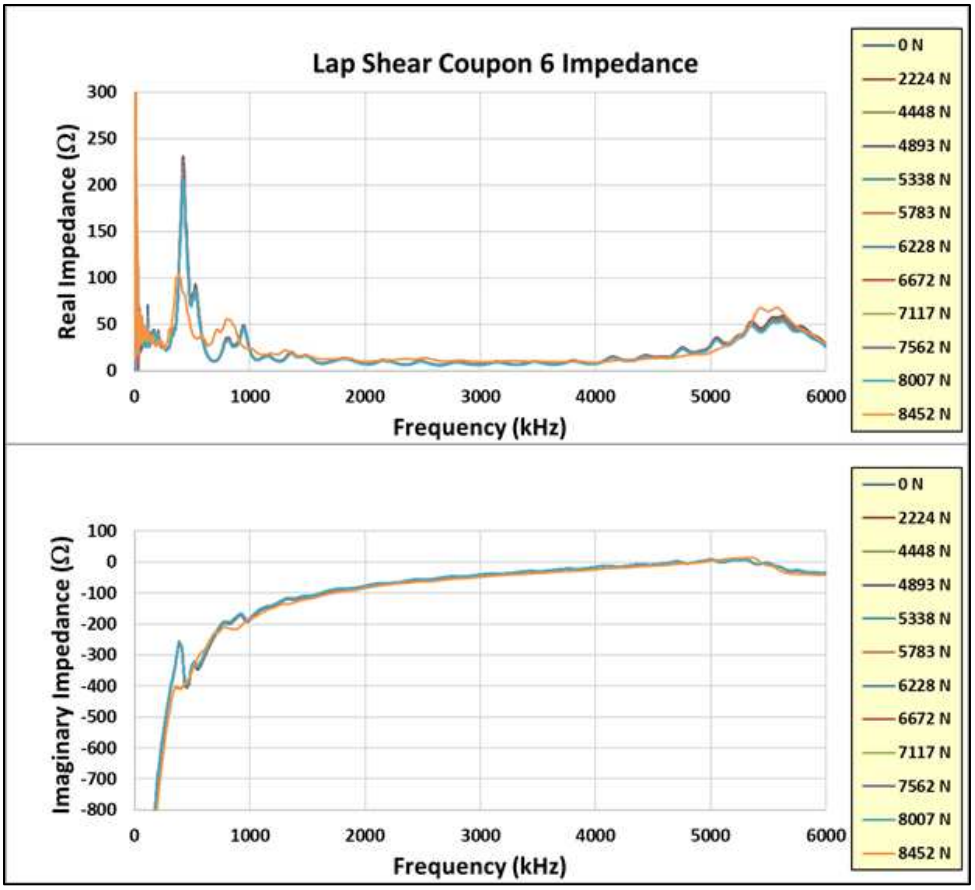

Figure 57. Coupon #6 sensor impedance/load results.

Similar patterns are observed in the primary radial and thickness impedance responses as the joint load increases for coupon #5 and #6, but not coupon #4. Coupon #4 is not unloaded during impedance measurements, whereas coupons #5 and #6 are measured in the unloaded state between successive loads.

Flatwise Tension Coupon Experiments

The flatwise tension coupons that were fabricated are now bonded to 25.4 mm x 25.4 mm x 50.8 mm aluminum blocks to attach the test machine grips allowing the coupons to be tested in flatwise tension (orthogonal to the shear load direction). A structural paste adhesive (Fibreglast 1101) is used to bond the coupon to the aluminum block[35]. Fibreglast 1101 is a two-part structural paste adhesive that has a higher tensile strength than EA 9394 (used for the coupon adherend bond)

and it is chosen to force the failure to occur in the adherend-adherend test coupon bond. Eight coupons are fabricated, 4 pristine and 4 with embedded sensors as shown in Figure 58.

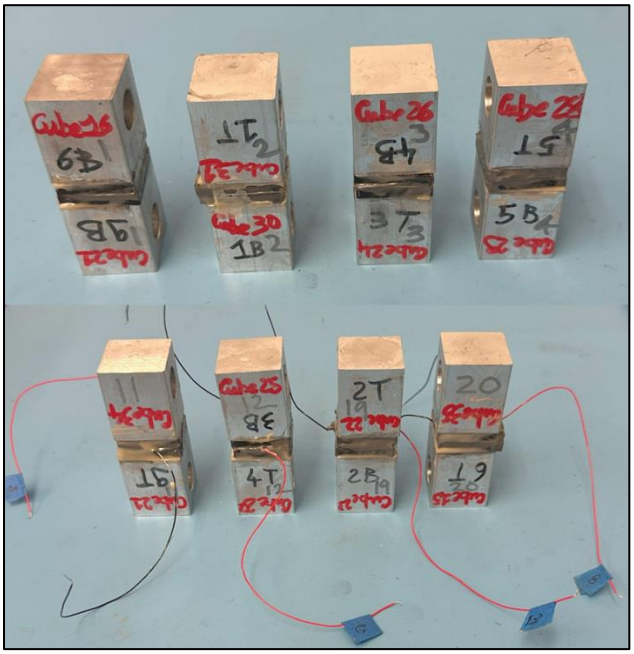

Figure 58. Flatwise tension test coupons.

Figure 59 shows a pristine flatwise tension coupon mounted in the test machine.

Figure 59. Pristine flatwise tension coupon in the test machine.

The pristine flatwise tension coupons are all tested to failure and unfortunately all failed between the aluminum block and coupon bond and not in the coupon-coupon bond as shown in Figure 60. This premature failure is due to inadequate surface preparation of the aluminum and coupon surface prior to bonding.

Figure 60. Failed pristine flatwise tension coupon.

Similar test results occurred with the embedded sensor coupons. All of the failed coupons are prepped and re-bonded at the failed interface. The tests are repeated with the same results on the other block/coupon interface, indicating that the other interface bond suffered from inadequate surface preparation prior to bonding. Again, the coupon/block surfaces are sanded, prepped, and re-bonded.

All eight coupons are retested and achieved higher failure loads than the previous tests, however, only one coupon failed in the actual coupon adherend-adherend bond. The

electromechanical impedance of this coupon was measured continuously during the experiment. This is accomplished by a continuously applied frequency dwell at the embedded sensor primary radial impedance resonance. Figure 61 shows the Nyquist impedance plot during the test loading on the laptop and Figure 62 shows the same plot at coupon failure.

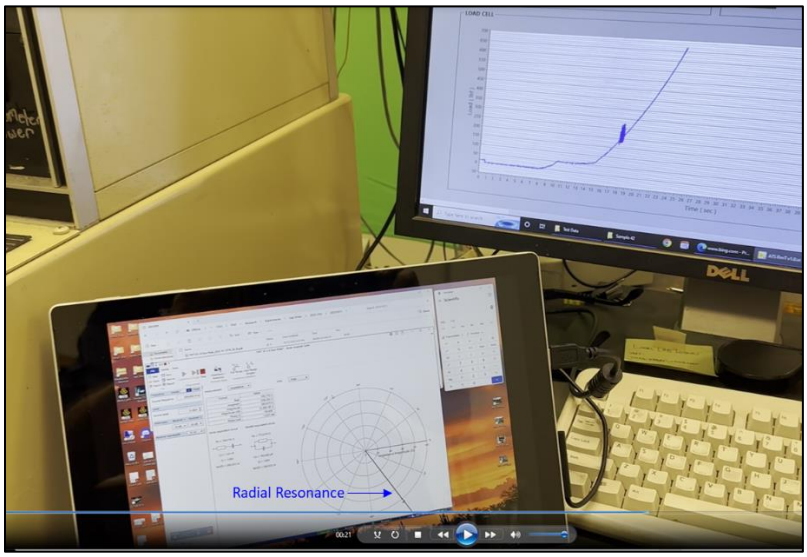

Figure 61. Flatwise tension coupon impedance during loading.

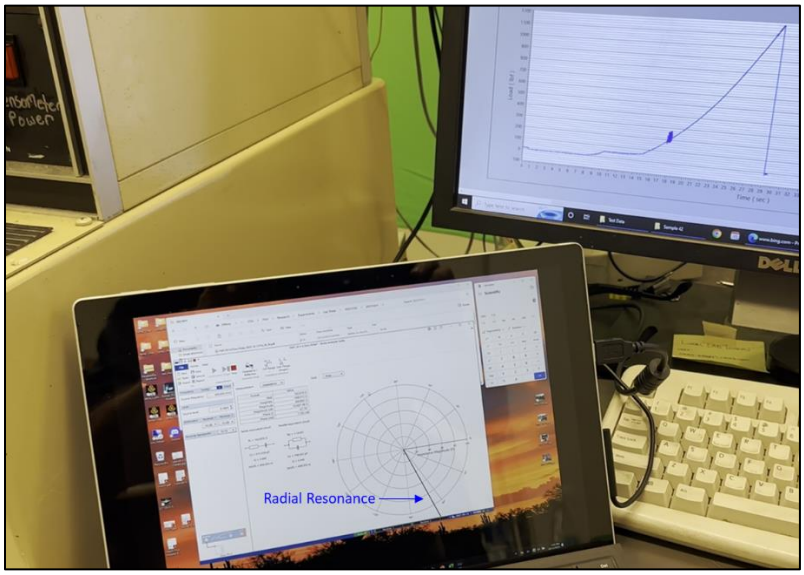

Figure 62. Flatwise tension coupon impedance at test failure.

All experimental results for Phase 3 efforts are discussed in the following section.

Discussion

The focus of this experimental work was to further quantify the viability of embedded piezoelectric sensors within the bondline of single lap shear and flatwise tensile composite joints to monitor the structural health of the bond and warn of impending joint failure from repeated loadings. Previous experiments were performed on embedded sensors in single lap shear composite joints with film adhesive bonds, showing the promise of health monitoring using the radial and thickness impedance response characteristics during loading[36]. However, the structural performance of these joints was degraded due to the inclusion of the sensor in the bond. To further evaluate this performance, a second set of experiments was performed using a structural paste adhesive with a thicker bondline to maintain the structural performance of the joint with the embedded sensor. Use of the paste adhesive with a 3D printed bond fixture acted to control the bondline thickness and resulted in similar, uniformly thick bondlines between the pristine and embedded sensor bonds. After fixture interference issues corrupted the impedance measurement of the first set of paste adhesive coupon experiments, a second set of paste coupons were fabricated and tested. The single lap shear failure loads experienced with these sensor coupons were within 1% of the pristine coupons and exhibited similar failure modes. The correction from the previous film adhesive experiments was to create a bondline that was double the sensor thickness, thus allowing the adhesive to fully encapsulate the sensor and reduce the adhesive voids experienced in the prior bonds. Also, the sensor lead wires were routed out of the bond in the minimum area of shear stress which was not possible in the film adhesive coupon fabrication. To reduce the wire footprint on the bonding surfaces for these coupons, the sensor wires were routed individually out each side of the area of minimum shear stress in the bond. In order to expand on the in situ sensor's ability to monitor bond health during repeated loadings, the primary impedance resonance for the

radial and thickness response were evaluated for damping and amplitude trends and variations. The additional review of impedance resonant amplitude and modal damping proved insightful to the sensor health monitoring approach.

The flatwise tension coupons exhibited a large variation in bondline thickness in the 25.4 mm x 25.4 mm bond area. The coupons all experienced similar failures between the loading block and the coupon surface, which was not in the desired location of the adherend-adherend coupon bond. Future work is required on the flatwise tension experiments in order to gather meaningful data for evaluation.

Single Lap Shear Coupon Electromechanical Impedance

Three embedded sensor lap shear coupons were tested to failure using incremental increasing load applications. The impedance was measured between loads, normally in the unloaded state but still installed in the test fixture. Coupon #4 is tested first with the electromechanical impedance measured installed in the test fixture but unloaded. The coupon survived nine successive load increments and failed at 8326 N. For this coupon, it was decided to measure the impedance of the sensor while the coupon was loaded (pause in the upload). Typically, the coupon impedance is measured in the unloaded state. This approach was attempted to improve test efficiency and evaluate the loaded impedance continually, The coupon impedance measurements (real and imaginary parts) are shown in Figure 63.

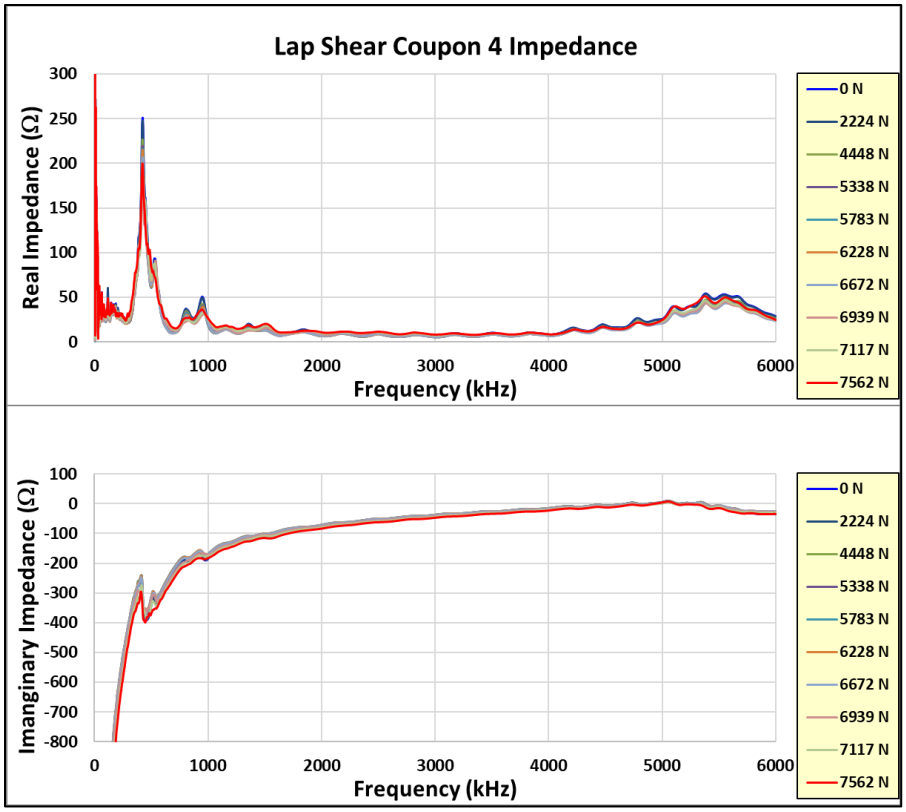

Figure 63. Coupon #4 impedance measurements for all test loads.

Note that there is not a lot of change in the impedance response with the incremental loads. The initial method used to evaluate the structural health of the bond is the damage index (DI), which is the root mean square deviation (RMSD) of the real part of the measured impedance resonance as the load is increased. The damage index is normally evaluated only for the primary radial impedance resonance but may be evaluated for any impedance resonance. An arbitrary threshold DI of -2% or greater is used to indicate impending coupon failure. For these experiments, the primary radial and thickness impedance modes are evaluated. Note the DI did not change appreciably prior to failure for the radial or thickness primary resonance as shown in Figure 64 (failure is denoted as the dashed vertical line) indicating a possible issue with measuring the DI in the coupon loaded state.

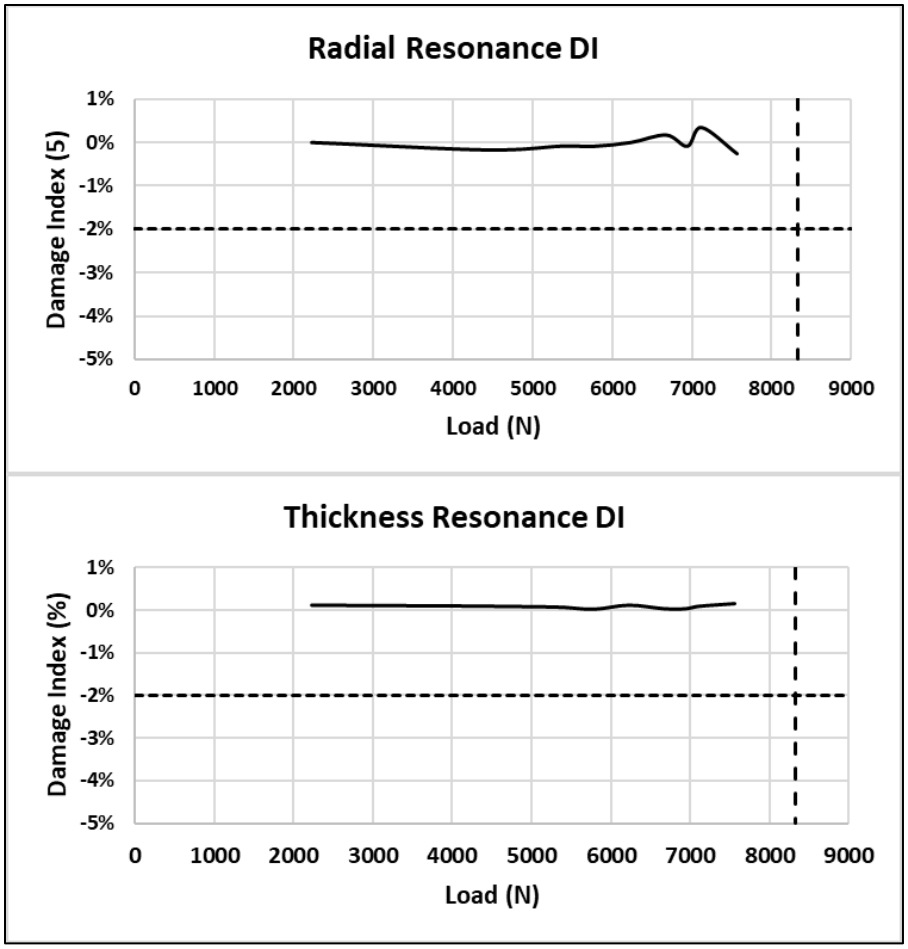

Figure 64. Coupon #4 radial and thickness mode DI.

Therefore, it is decided to revert to measuring the coupon impedance in the unloaded state after each incrementally larger load is applied and unloaded. Coupons #5 and #6 were incrementally loaded with the impedance measured between loads in the unloaded state. Reviewing coupon #5 results first, Figure 65 shows the real and imaginary impedance measurements up to failure. Note the appreciable resonance shift for the primary resonances (radial and thickness) on the highest recorded load impedance.

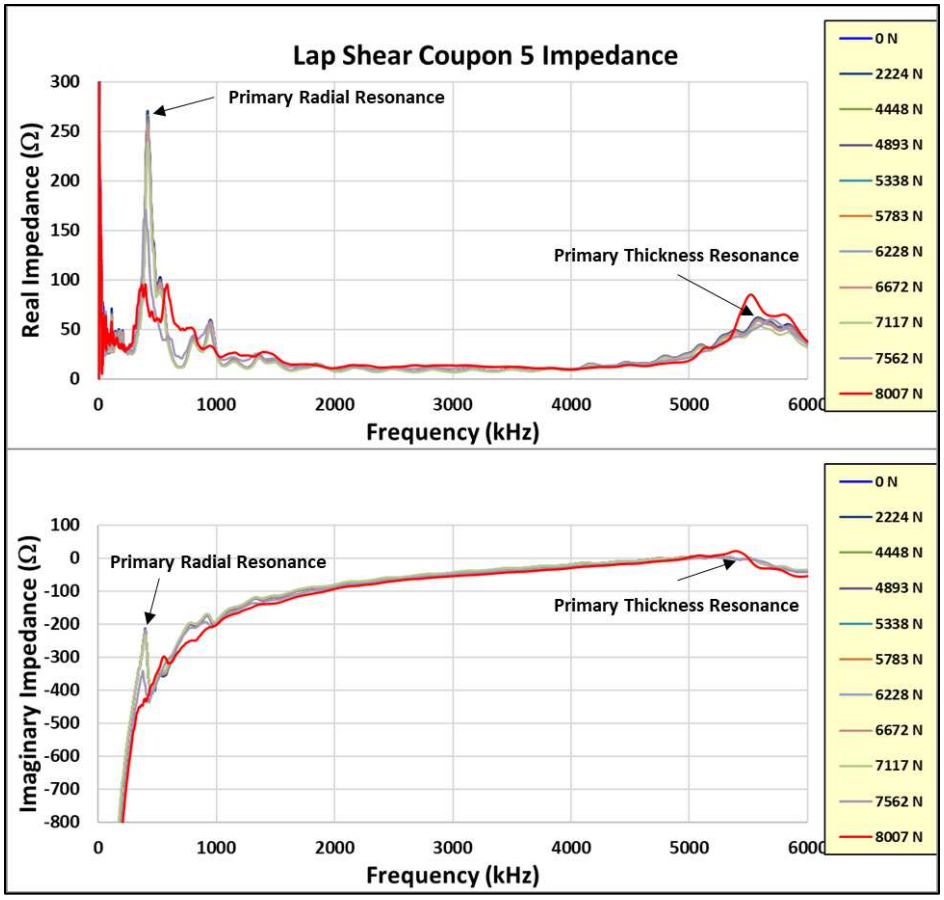

Figure 65. Coupon #5 impedance measurements.

Figure 66 shows the primary radial mode DI as the load approaches failure (note the failure load is 8221 N, designated as the dashed vertical line on the figure).

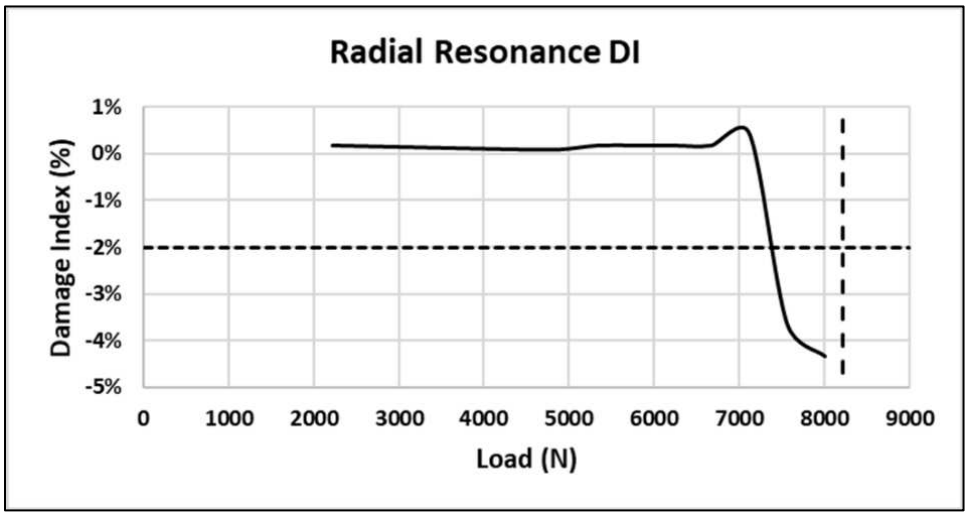

Figure 66. Coupon #5 radial mode DI.

Note the rapid change (decrease) in the DI prior to failure. The horizontal dashed line at a DI of -2% is the normal threshold used to indicate impending failure. This coupon achieved a DI of -4.3% prior to failing. Examining the radial resonant response more closely between loadings including the amplitude and not just the frequency change produces Figure 67 for coupon #5 data.

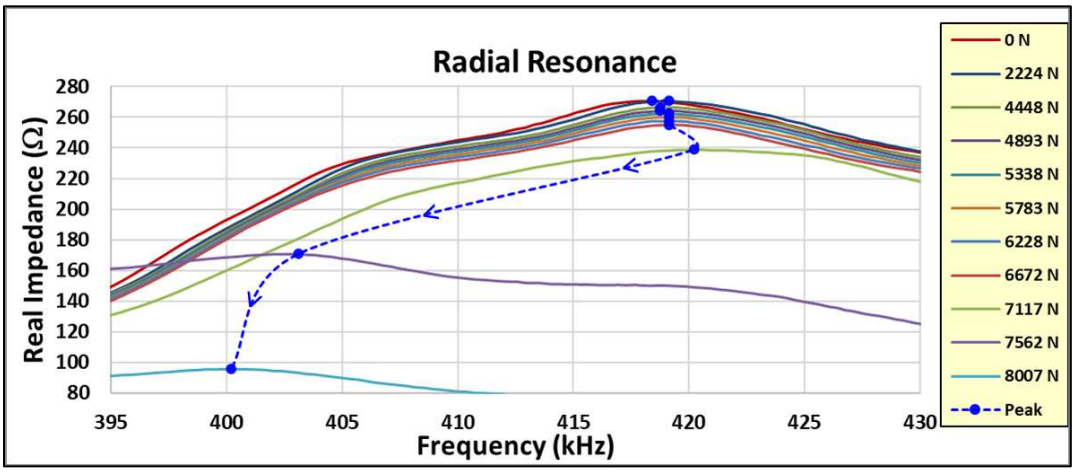

Figure 67. Zoom in on radial resonant response between loads.

The dashed line connects the peak amplitude of the radial resonance for each load, with the arrows designating the increasing load direction. Note that the amplitude decreases and the modal damping increases for each incremental load as the frequency change increases. Figure 68 shows the modal damping trend and amplitude of the radial resonance as the load level increases to failure.

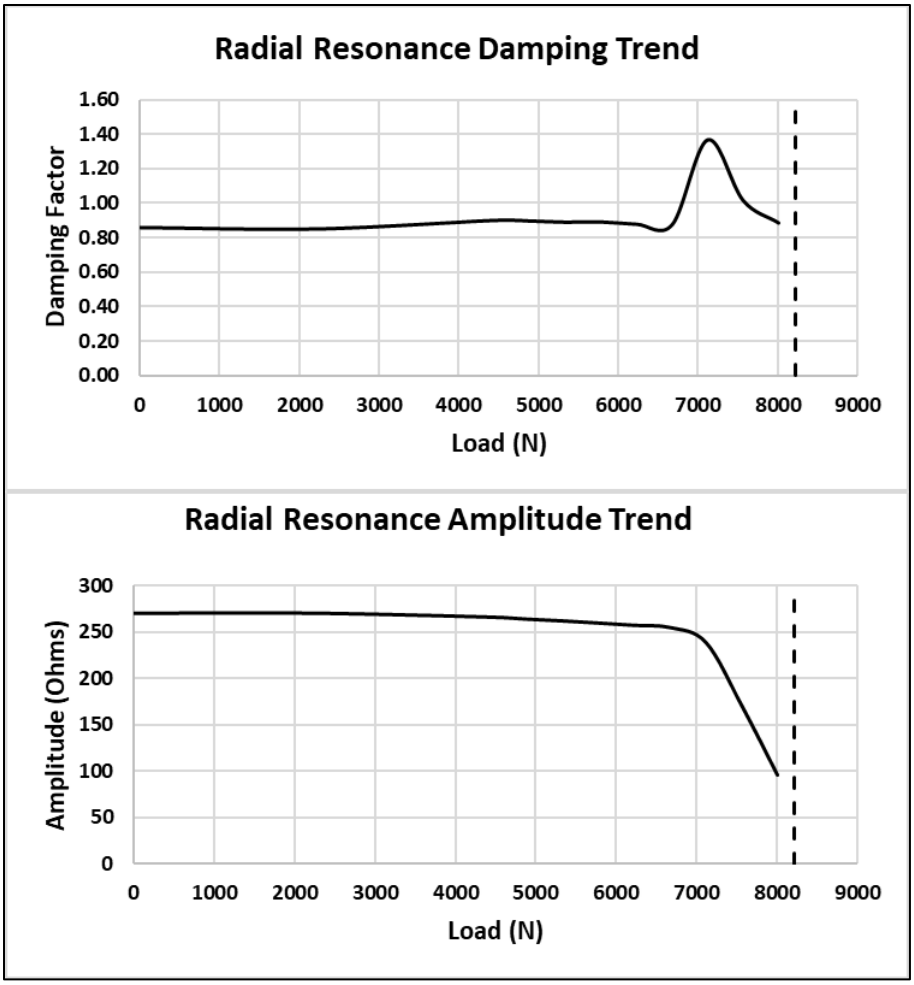

Figure 68. Coupon #5 radial resonance damping and amplitude trends.

As seen in Figure 68, there is a large decrease in the modal amplitude as the coupon approaches failure. This is similar to the DI as the coupon passes the 7000 N load value. It is of note that an increase in damping is observed at a lower load level (<7000 N). This adds valuable insight to the health monitoring ability of the impedance response, possibly suggesting impending failure earlier than the DI evaluation provides.

Similar data analysis is performed for the thickness impedance resonance measurements. Figure 69 shows the DI for the thickness resonance. Note the DI increases to +2% before decreasing on the final load. Figure 70 shows a closeup of the thickness resonance during loading.

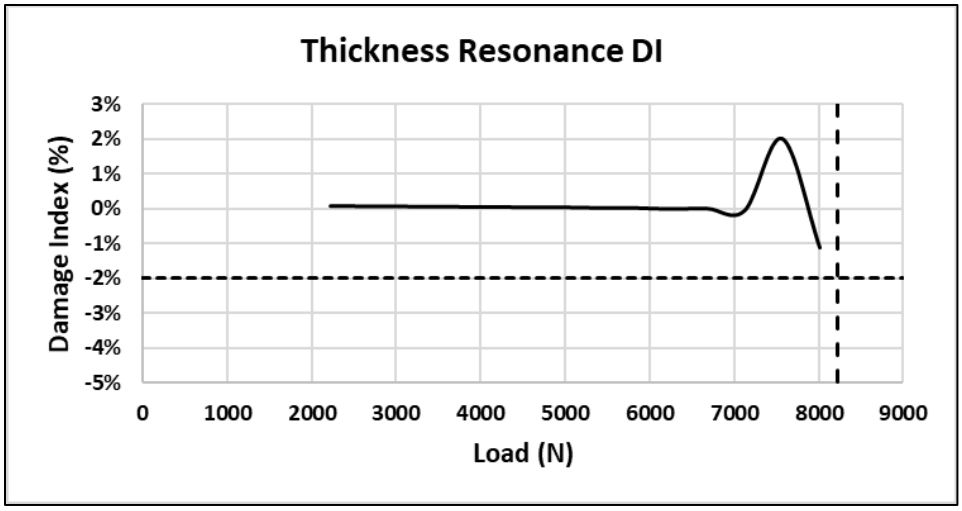

Figure 69. Coupon #5 thickness resonance DI.

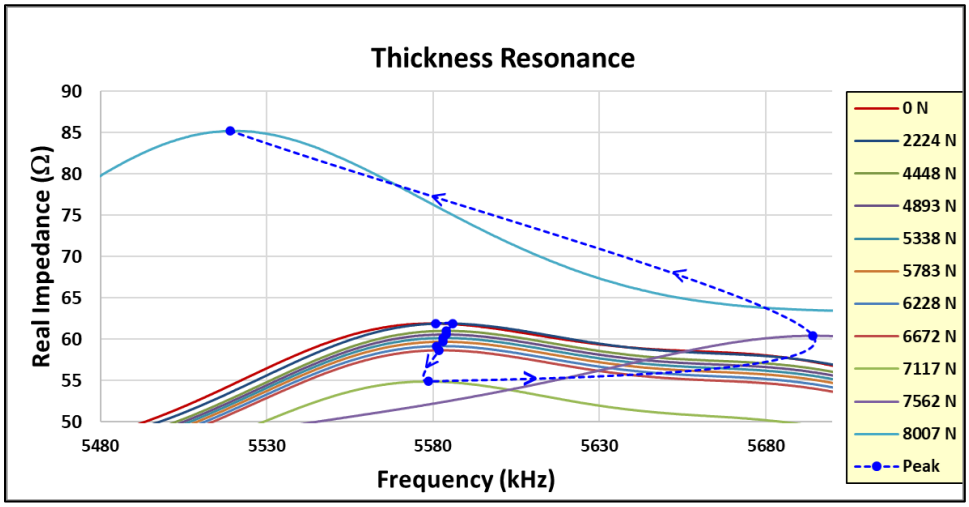

Figure 70. Coupon #5 thickness impedance resonance.

On Figure 70 note the initial decrease in amplitude in the real impedance response at a relatively constant frequency followed by an abrupt amplitude increase. Evaluating the resonance damping and amplitude trends for the loads produces Figure 71. An interesting note for the thickness resonance is the amplitude increases abruptly as failure approaches, which could indicate a local stiffening in the vertical direction of the joint prior to failure.

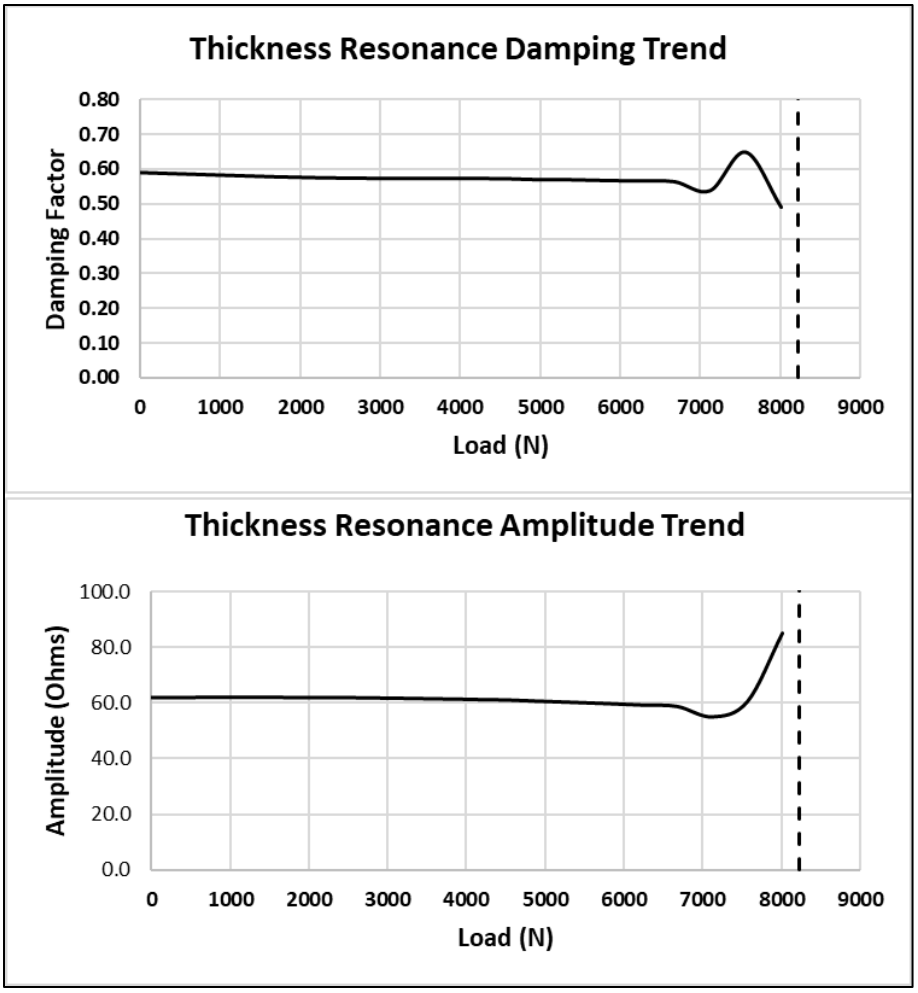

Figure 71. Coupon #5 thickness mode damping and amplitude trends.

Another way to view the impedance is to only plot the initial and final load measurements. This shows the change clearly without the incremental load plots included, as seen in Figure 72. This shows the creation of two radial resonances from the initial radial mode. The thickness mode is clearly dominant and more decoupled from the radial mode harmonics, which appear to have dissipated since the lower amplitude modes were created.

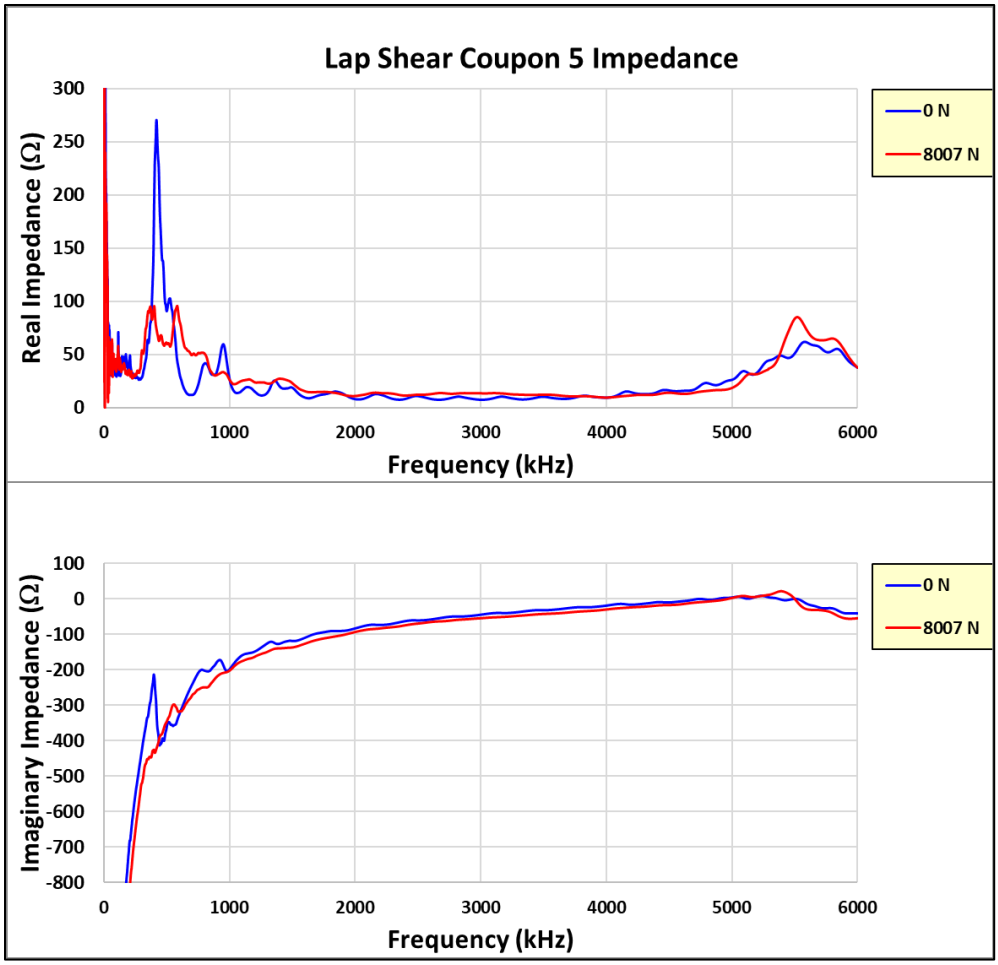

Figure 72. Coupon #5 initial and final impedance measurements.

Similar data analysis is performed on the coupon #6 test data with concludes with similar results. Figure 73 shows the impedance test results for the coupon #6 experiments. Figure 74 shows the radial resonance DI, which abruptly drops to a value -8% on the last load increment. Figure 75 shows the closeup of the radial response resonance as the load is incrementally increased. Note the increase in damping and drop in resonant frequency and amplitude as the coupon tends toward failure, similar to coupon #5.

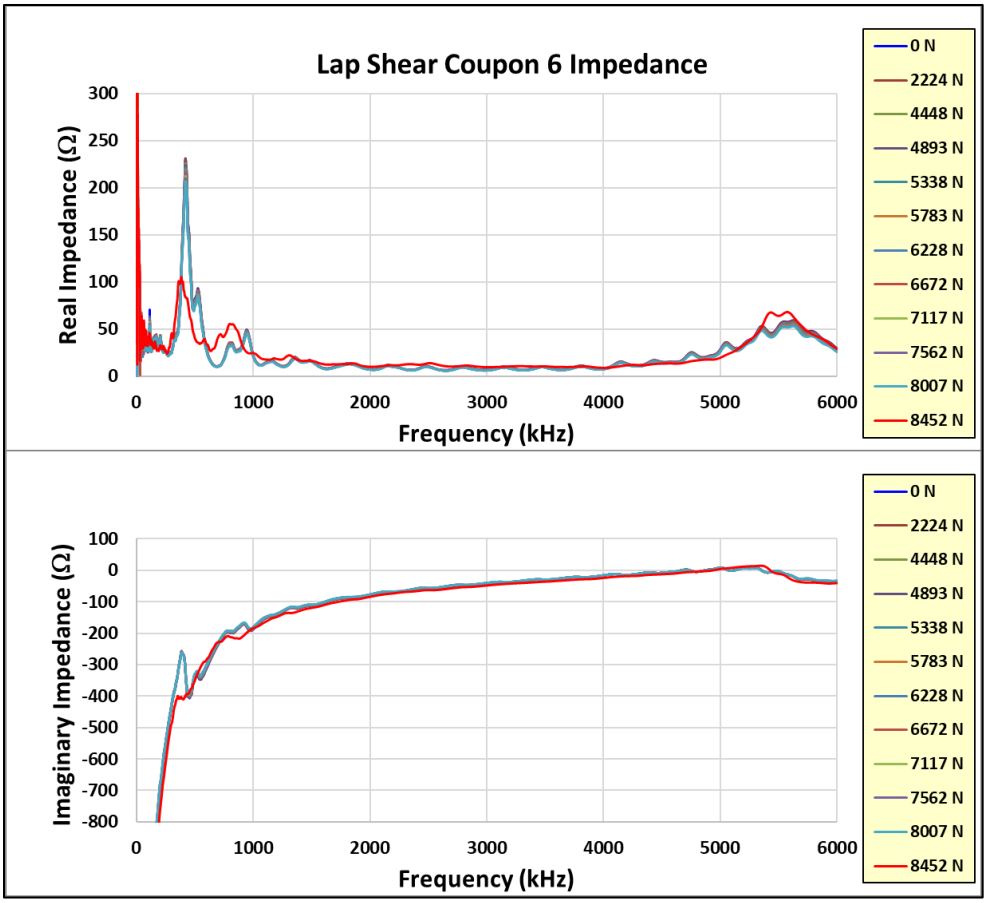

Figure 73. Coupon #6 impedance measurements.

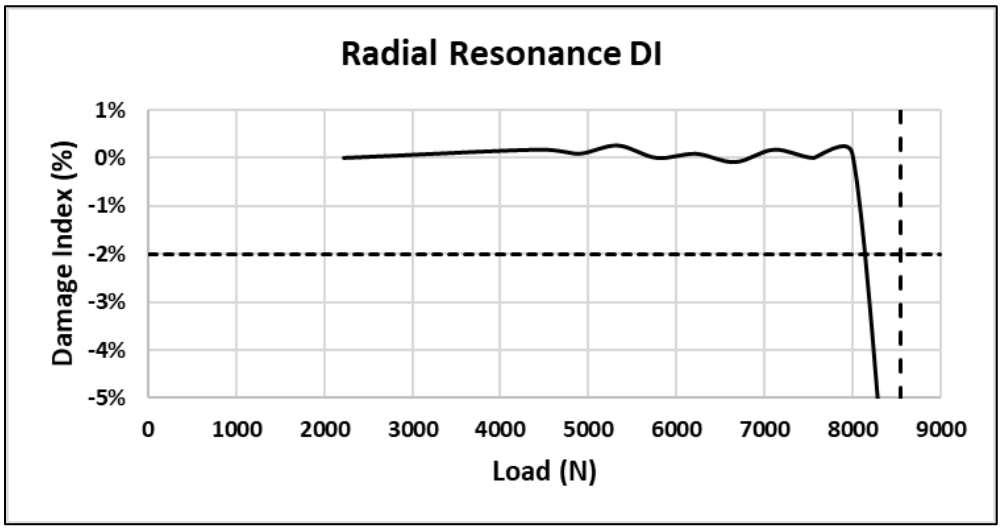

Figure 74. Coupon #6 radial resonance DI.

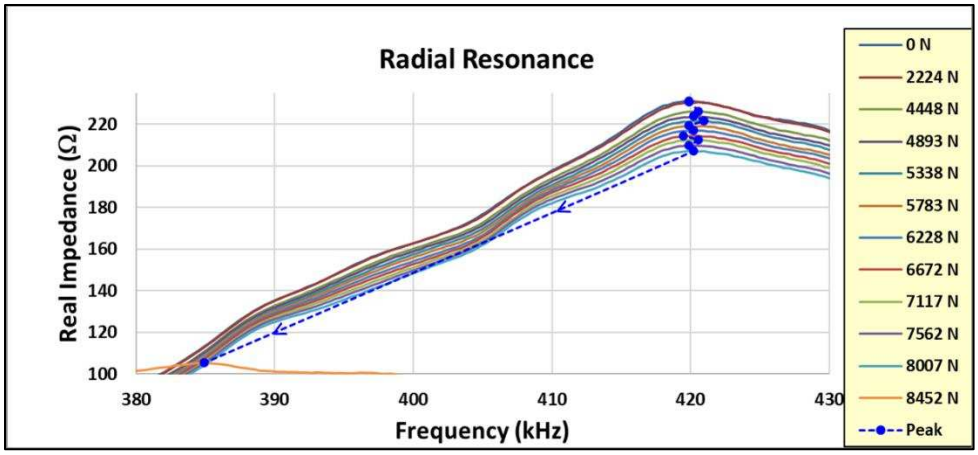

Figure 75. Coupon #6 radial resonance impedance.

Figure 76 shows the damping trend and amplitude with increasing load for the primary radial resonance of coupon #6. Note the initial damping and amplitude increase prior to a large amplitude decrease on the last test load.

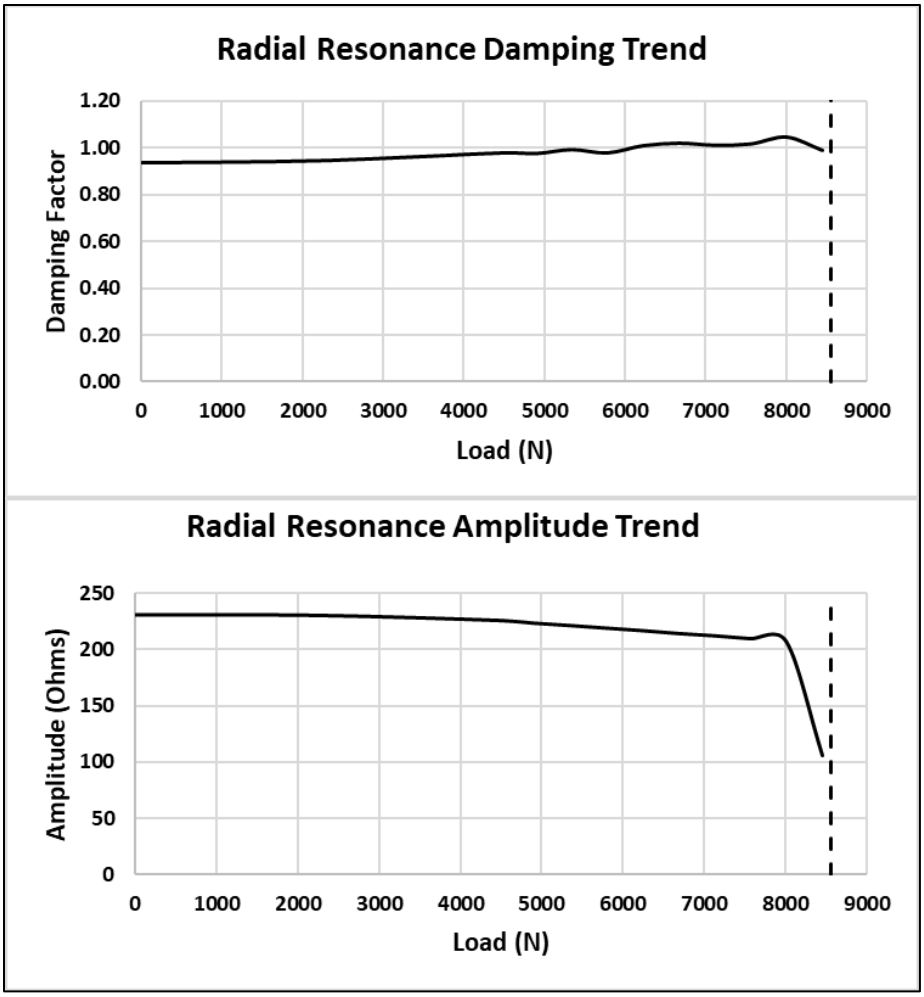

Figure 76. Coupon #6 radial resonance damping and amplitude trends.

The thickness resonance response for coupon #6 is now evaluated. Figure 77 shows the thickness DI for the test loads. Figure 78 shows a closeup of the thickness resonance for the test load increments.

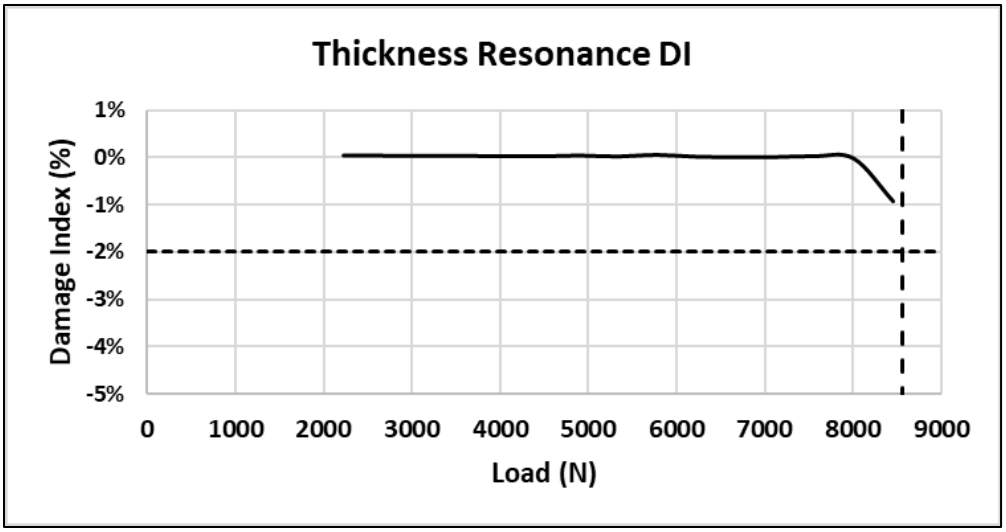

Figure 77. Coupon #6 thickness resonance DI.

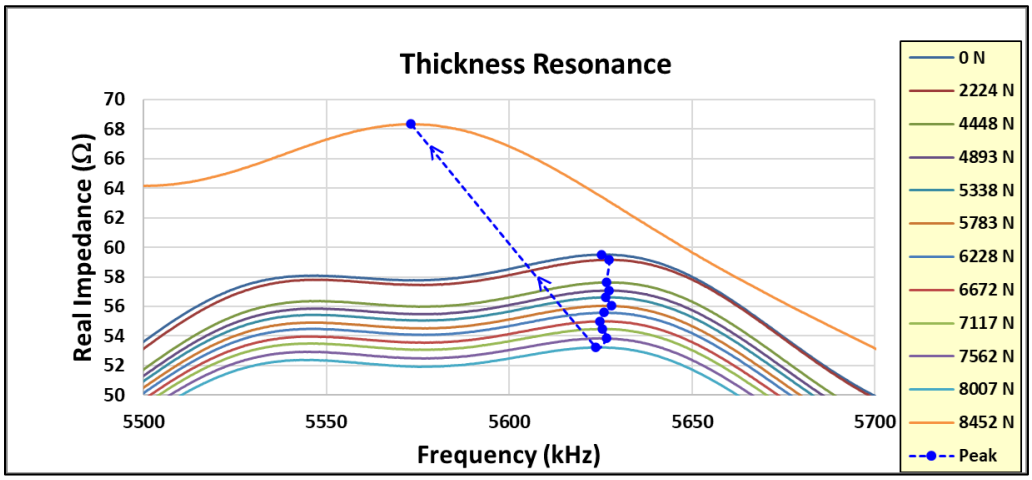

Figure 78. Coupon #6 thickness resonance.

Figure 79 shows the thickness resonance damping and amplitude trends. This mode shows a distinct damping loss, but a similar amplitude increase prior to failure. Similar to coupon #5, Figure 80 shows the initial and final load impedance (real and imaginary). As separation of the primary radial resonance into two lower amplitude modes is observed and the primary thickness response is amplified and more prominent with less interaction with radial harmonic modes.

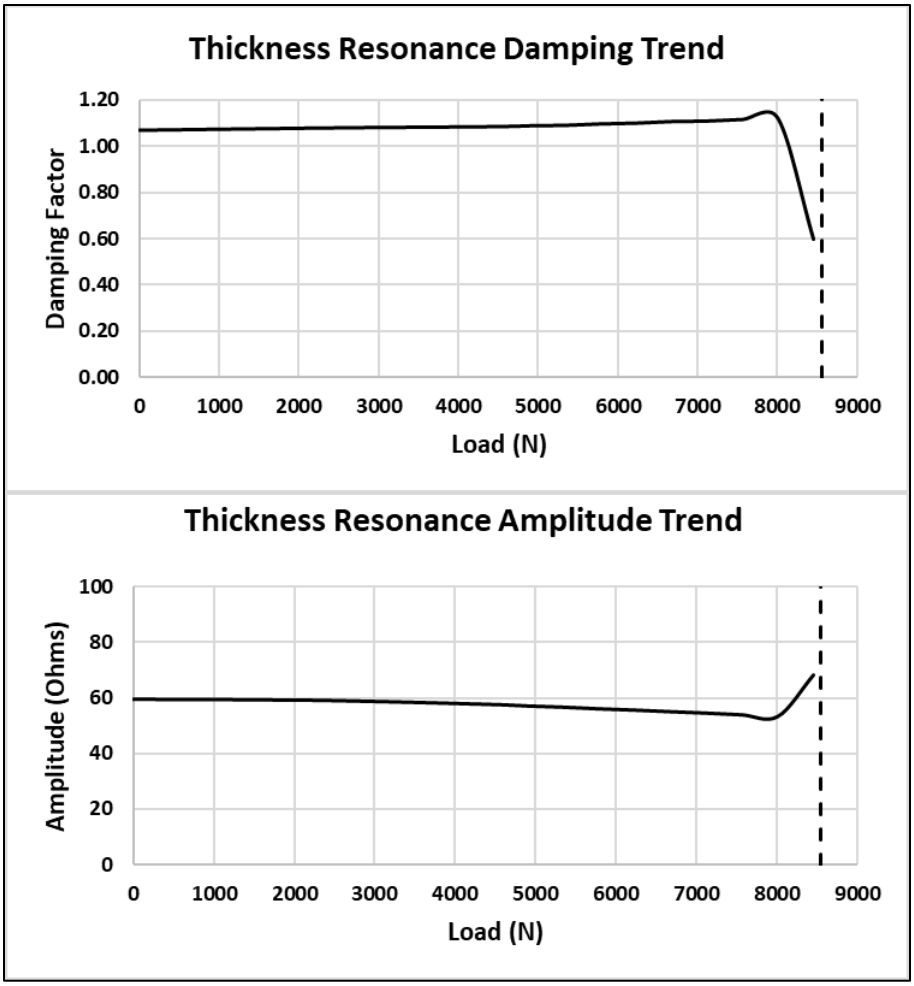

Figure 79. Coupon #6 thickness resonance damping and amplitude trends.

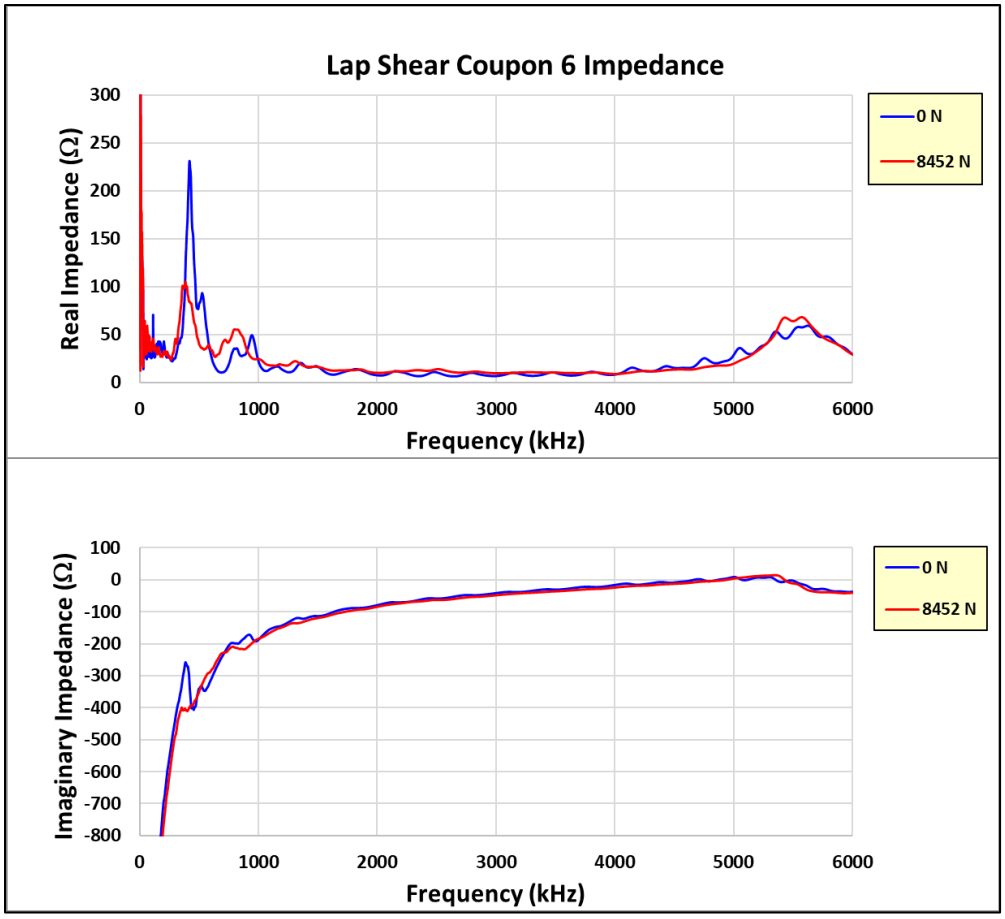

Figure 80. Coupon #6 initial and final load impedance measurements.

Reviewing the combined results of the coupon #5 and #6 together shows a consistency in the sensor's response to increasing loads. The combination of radial and thickness response evaluation adds a multi-axis approach to health monitoring with a single sensor (radial equals tension and thickness equals transverse tension). The radial and thickness response DI calculations show similar changes (both modes) for both coupons. These radial DI's register higher deviations in the response (greater than -2%) and the thickness DI's show similar direction trends but less than -2% change. Both are indicative of joint structural softening prior to failure. The response amplitudes have different trends between the radial and thickness responses. The radial amplitude reduces greatly in magnitude for both coupons prior to failure, indicative of a higher magnitude of load (damping) in the tensile direction. Both coupon observed thickness amplitudes increase in

magnitude prior to failure, indicating joint de-consolidation in the transverse (vertical) direction prior to failure. The damping trends are similar between coupons but differ in the radial and thickness resonances. The radial resonances both exhibit increases in modal damping prior to failure and the thickness resonances exhibit a decrease in modal damping prior to failure. The radial responses are indicative of a greater internal force in the tensile direction and the thickness responses are indicative of a lightening of load in the transverse direction, similar to joint de-consolidation. Both trends lead to weakening of the joint. The value of reviewing these quantities with additional scrutiny provides an earlier indication of degradation of joint performance than observed with the standard DI approach for health monitoring. Therefore, adding these response quantities to the evaluation of measured impedance leads to an earlier warning of impending failure.

Coupon Flatwise Tension Electromechanical Impedance

Unfortunately, all but one of the flatwise tension coupons failed at the aluminum block / coupon interface as opposed to failing in the test coupon bond. The coupon that failed in the correct bond exhibited a low failure load that most likely relates to the adhesive mixing issues encountered in the batch 2 and batch 3 adhesive fabrication cures. It is of note that on this failure the electromechanical impedance resonance of the radial mode did change appreciably just prior to failure, indicating the sensor in the flatwise tension loading can monitor bond integrity. A future idea may be to create a larger aluminum block / coupon interface while maintaining the 25.4 mm x 25.4 mm bond test section. Essentially this lowers the stress experienced in the aluminum block bond thus allowing the coupon to be appropriately tested. Another improvement to consider is an updated bond fixture that facilitates a uniform bond thickness across the joint. This may be

accomplished by controlling the bond thickness at both ends of the bond instead of applying one force at the bond center.

Chapter 5 Conclusions and Recommendations

Conclusions

An approach has been developed, based upon using bond embedded piezoelectric disk sensors, to evaluate and improve their joint health monitoring capabilities. The experiments successfully proved the prognostic health monitoring capability of embedding piezoelectric sensors in the bonded composite joints, fully examining their responses (both radial and thickness impedance resonances). Expanding the use of the radial response DI to include the evaluation of the thickness response proved helpful in the robustness of the health monitoring approach. Detailed examination of these quantities including scrutiny of the primary response amplitude and damping trends also adds to the monitoring capability and provides an earlier warning of impending failure than the single evaluation of the radial DI. Furthermore, detailed review of the primary impedance responses allows for a physical understanding of the changes in the joint as failure is approached. The use of the single sensor in the area of maximum joint load transfer provides response information to address joint health in multiple load axes for the lap shear coupon (radial response equals tensile load and thickness response equals transverse tension load). The use of the structural analysis FEM results provided a basis for sensor location in the bonded joint minimizing any performance degradation and at the same time optimizing the preferred sensor location in the area of maximum joint load. After completing the experiments and reviewing the data results in detail, a novel health monitoring approach has been identified and proven to be beneficial in an earlier joint failure indication. For practical use on bonded composite aircraft, it recommended to use the detailed FEM 2D plane strain analysis of the critically loaded joints to determine bondline sensor locations, embed the sensors during fabrication, and measure the impedance response of the sensors (radial and thickness primary resonant frequency, amplitude,

and damping) initially at aircraft build completion and repeatedly after operational usage (loadings). Applying this approach to these data allows for an initial evaluation of joint health and repeated checks during the life of the aircraft. The use of the embedded sensors fills the inability of the current joint inspection technique (NDI) to identify a weak bond providing prognostic joint heath monitoring capability and eliminates the need for expensive proof load testing of the aircraft and its critical composite joints.

Recommendations for Future Work

Future work is recommended to fully assess the flatwise tension sensor bond health monitoring viability. The flatwise tension experiments performed in the Phase 3 efforts were not successful in evaluating the sensor health monitoring viability due to repeated failures at the load block / test coupon interface. However, it is noted that one of the coupons did fail in the coupon bond and the sensor electromechanical impedance resonance did change abruptly prior to failure. This is promising and suggests that an embedded sensor in a flatwise tension load can monitor bond health.

References

1. Zweben, C. Advanced Composites for Aerospace Applications; Composites; IPC Business Press Limited, UK, October 1981.
2. Arif, M.; Ahmed, I. Advanced Composite Material for Aerospace Application-a Review. Int. J. Eng. Manuf. Sci. 2017, 7, 393–409.
3. Mrazova, M. Advanced composite materials of the future in aerospace industry, INCAS BULLETIN 2013, 5, 139–150.
4. Samann, F.E.F. Detecting Kissing Disbond Defect in Adhesively Bonded Structures: A Review. Int. Conf. Adv. Sci. Eng. (ICOASE) 2019, 2019, 214-219.
5. Jeenjitkaew, C.; Luklinska, Z.; Guild, F. Morphology and surface chemistry of kissing bonds in adhesive joints produced by surface contamination. Int. J. Adhes. Adhes. 2010, 30, 643–653.
6. Brotherhood, C.; Drinkwater, B.; Dixon, S. The detectability of kissing bonds in adhesive joints using ultrasonic techniques. Ultrasonics 2003, 14, 521–529.
7. Grondel, S.; Assaad, J.; Delebarre, C.; Moulin, E. Health Monitoring of a Composite Wingbox Structure. Ultrasonics 2004, 42, 819–824.
8. Masango, T.P.; Philander, O.; Msomi, V. The Continuous Monitoring of the Health of Composite Structure. Hindawi J. Eng. 2018, 2018, 1-7.
9. Varadan, V.K.; Varadan, V.V. Microsensors, Microelectromechanical Systems (MEMS), and Electronics for Smart Structures and Systems. Smart Mater. Struct. 2000, 9, 953–972.
10. Diamanti, K.; Soutis, C. Structural health monitoring techniques for aircraft composite structures. Prog. Aerosp. Sci. 2010, 46, 342–352.
11. Hassani, S.; Mousavi, M.; Gandomi, A.H. Structural Health Monitoring in Composite Structures: A Comprehensive Review. Sensors 2022, 22, 153, 1-45.
12. Dugnani R, Zhuang Y, Kopsaftopoulus F, et al. “Adhesive bond-line degradation detection via a cross-correlation electromechanical impedance-based approach.” Struct Health Monit 2016; 15(6): 650-667.
13. Annamdas VGM, Soh CK. “Application of Electromechanical Impedance Technique for Engineering Structures: Review and Future Issues.” Journal of Intelligent Material Systems and Structures 2010; 21(1): 41-59.
14. Zhuang Y, Kopsaftopoulos F, Dugnani R, et al. “Integrity monitoring of adhesively bonded joints via an electromechanical impedance-based approach.” Struct Health Monit 2018; 17(5): 1031-1045.
15. Ju, M.; Dou, Z.; Li, J.; Qiu, X.; Shen, B.; Zhang, D.; Yao, F.Z.; Gong, W.; Wang, K. Piezoelectric Materials and Sensors for Structural Health Monitoring: Fundamental Aspects, Current Status, and Future Perspectives. Sensors 2023, 23, 543.
16. Giurgiutiu, V. Structural Damage Detection with Piezoelectric Wafer Active Sensors. J. Phys. Conf. Ser. 2011, 305, 012123.

17. Giurgiutiu, V.; Rogers, C.A. Recent Advancements in the Electro-Mechanical (E/M) Impedance Method for Structural Health Monitoring and NDE. In Proceedings of the Conference on Smart Structures and Integrated Systems, San Diego, CA, USA, 1 March 1998; pp. 536–547.
18. Mei, H.; Haider, M.F.; Joseph, R.; Migot, A.; Giurgiutiu, V. Recent Advances in Piezoelectric Wafer Active Sensors for Structural Health Monitoring Applications. Sensors 2019, 19, 383, 1-21.
19. Giurgiutiu, V.; Zagrai, A. Embedded self-sensing piezoelectric active sensors for on-line structural identification. J. Vib. Acoust. Trans. ASME 2002, 124, 116–125.
20. Giurgiutiu, V. Piezoelectric Wafer Active Sensors. In Structural Health Monitoring of Aerospace Composites; Elsevier: Amsterdam, The Netherlands, 2016, 177–248.
21. Schmidt RP, Kalser DA. "Woven Preform for Structural Joints, Patent No.: US 6,874,543 B2", Apr. 5, 2005.
22. Flansburg BD, Engelstad SP, Lua J. "Robust Design of Composite Bonded Pi Joints." Proceedings of the 50th AIAA/ASME/ASCE/AHS/ASC Structures, Structural Dynamics, and Materials Conference, AIAA 2009-2447, 2009; Palm Springs, CA, May 4-7.
23. CYCOM 5320-1 Prepreg, Technical Data Sheet, Solvay, 2017. Available online: https://www.solvay.com/en/product/cycom-5320-1 (accessed on 05/24/2020).
24. FM300-2 Film Adhesive, Technical Data Sheet, Solvay, 2017. Available online: https://www.colvay.com/en/product/fm-300 (accessed on 06/23/2020).
25. APC International, Ltd.. Physical and Piezoelectric Properties of APC Materials. 2019. Available online: https://www.american piezo.com (accessed on 03/29/2021).
26. Ansys® Academic Research Mechanical, Release 2022 R2, Help System, Coupled Field Analysis Guide; ANSYS, Inc.: Canonsburg, PA, USA.
27. Gresil, M.; Yu, L.; Giurgiutiu, V. Predictive modeling of electromechanical impedance spectroscopy for composite materials. Struct. Health Monit. 2012, 11, 671–683.
28. Bode 100 User Manual, OMICRON Lab, OMICRON Electronics. 2019. Available online: https://www.omicron-lab.com (accessed on 10/11/2020).
29. Schuster, T. Bode 100–Application Note: Impedance Measurements using the Bode 100. 2020 Omicron Lab–V1.0. Available online: https://www.omicron-lab.com (12/10/2022).
30. ASTM D5868; Standard Test Method for Lap Shear Adhesion for Fiber Reinforced Plastic (FRP) Bonding. ASTM International: West Conshohocken, PA, USA, 2015.
31. ASTM D5573-99; Standard Practice for Classifying Failure Modes in Fiber-Reinforced-Plastic (FRP) Joints, ASTM International: West Conshohocken, PA, USA, 1999.
32. Bhalla, S.; Soh, C.K. Structural Impedance based damage diagnosis by piezo-transducers. Earthq. Eng. Struct. Dyn. 2003, 32, 1897–1916.
33. Tseng, K.K.-H.; Naidu A S K. Non-parametric damage detection and characterization using smart piezoceramic material. Smart Mater. Struct. 2002, 11, 317–329.
34. LOCTITE EA 9394 AERO Epoxy Paste Adhesive, Technical Data Sheet, Henkel, 2013. Available online: https://www.heatcon.com/wp-content/uploads/2015/08/HCS2407-141_Henkel-Resin-Kit-LOCTITE-EA-9394-AERO.pdf (accessed on 7/11/2022).

35. Fibreglast 1101, Technical Data Sheet, Fibre Glast Development Corporation, 2020. Available online: https://s3.amazonaws.com/cdn.fibreglast.com/downloads/00056.pdf (accessed on 7/7/2022).
36. Caldwell, S.; Radford, D. Composite single lap shear joint integrity monitoring via embedded electromechanical impedance sensors. Journal of Composites Science 2023, 7, 53, pp 1-24.